Design of a Wearable Device for Conditional Neuromodulation of the Pudendal Nerve

Arsam Nasrollahy Shiraz

A thesis submitted in partial fulfilment of the requirements for the degree of **Doctor of Philosophy**

Analogue and Biomedical Electronics Group

Department of Electronic and Electrical Engineering

University College London

Official declaration

I, Arsam NASROLLAHY SHIRAZ, confirm that the work presented in this thesis is my own. Where information has been derived from other sources, I confirm that this has been appropriately indicated in the thesis.

"The noblest pleasure is the joy of understanding."

Leonardo da Vinci

Abstract

The main functions of the lower urinary tract are to store and periodically void urine. These functions are controlled by complex neural circuits which are controlled in the brain, spinal cord and peripheral ganglia. After spinal cord injury, depending on the level and completeness of the lesion, very often the normal lower urinary tract functions are disrupted. Incontinence and concurrent voiding problems are the prevalent ensuing conditions. Before the advent of the existing effective treatment and management techniques, such conditions constituted the first cause of death in spinal cord injury patients. There is no single solution, however, that can recover the full bladder function even today. The prevalent form of the treatment involves the use of drugs to maintain continence and catheterisation for voiding. The drugs have troublesome side effects and catheterisation very often leads to infection which is the first cause of re-hospitalisation in this patient group. Therefore, there is a need for an alternative form of treatment.

The pudendal nerve neuromodulation may provide an opportunity for designing a solution capable of recovering the full bladder function. The unique aspect of the pudendal nerve neuromodulation is that depending on the stimulus frequency it may result in micturition-like or continence-like reflexes. Also, the stimulus current can be applied trans-rectally, meaning that a wearable and minimally invasive solution may be developed. The major limitation of such a solution is the high level of the required stimulus current to activate the nerve trans-rectally. A feature of the trans-rectal neuromodulation of the pudendal nerve is that its efficacy may be increased by only applying the stimulus current when needed

when employed to tackle incontinence.

There is evidence that the electromyogram signal from the external anal sphincter may be used as a control signal to detect the onset of hyperreflexive contractions of the bladder. Thus, a single device capable of the surface electromyogram recording from the external anal sphincter and trans-rectal stimulation of the pudendal nerve can be designed to conditionally deliver the stimulus current to the target nerve. The main objective in designing such a device should be to minimise the required stimulus current and to design the recording electrodes for a chronic use.

Using a state of the art computational model and different experimental measurements, an electrode configuration was designed which based on the models required a considerably lower stimulus current level to activate the nerve. A novel algorithm was developed to account for the variations of the nerve in different individuals and in an individual in different postures. Using this novel algorithm, it was verified that the said configuration requires an equally low stimulus current for all the variations. Thus, the modelling results suggest that by employing the proposed design, the trans-rectal neuromodulation of the pudendal nerve may be implemented as a viable solution.

The surface electromyogram signal is dependent on certain features of the target muscle, skin condition, electrode shape, electrode material, electrode size and the recording apparatus. A medical grade stainless steel was selected as the material from which the electrodes were made, primarily due to its availability and mechanical properties. Finding the design parameters of a system capable of the surface electromyogram recording from the external anal sphincter using stainless steel electrodes with no contact tissue preparation is of great interest. Based on theoretical models and practical considerations, a set of prototypes were designed and developed and in a proof-of-concept study, a design capable of efficaciously estimating the amplitude of the surface electromyogram signal recorded from the external anal sphincter was identified.

Acknowledgement

I am deeply indebted to Prof. Andreas Demosthenous who supervised me with meticulous professionalism and selfless passion. His advice and support through my academic career opened new avenues that positively affected my life. His tremendous enthusiasm for science, professional demeanour and invaluable academic expertise taught me personally and academically.

Special thanks go to Prof. Craggs whose breadth and depth of knowledge and experience enlightened me throughout the course of the project. I would like to also thank Dr Vanhoestenberghe and Prof. Donaldson for their involvement in the project. I am grateful to Dr Mosse and Dr Nikitichev for their help in making the prototypes and sharing their pragmatic insight in making things. I would like to thank Mr Solomon for his help in performing the experiments. Also, many thanks go to Dr Leaker for managing and funding the project through NUCT Ltd.

Without the help and support of my parents, none of what I have achieved would be possible. It goes without saying that I am and always will be thankful for all they have done for me. The companionship and support of my wife formed a driving force behind my endeavours throughout the PhD study and I am most grateful to her.

I would like to thank all the friends, family and colleagues who have helped and supported me in achieving my goals.

Finally, I would like to thank UCL for the scholarships to pursue the PhD degree.

Contents

List of Figures

List of Tables

Acronyms

ACh	Acetylcholine
AF	Activating function
AP	Action potential
AHP	After Hyper polarisation
ATP	Adenosine triphosphate
CNS	Central nervous system
CPE	Constant phase element
CV	Conduction velocity
DAP	Depolarising after-potential
DD	Double differential
DFT	Discrete Fourier transform
DGN	Dorsal genital nerve
DL	Double layer
DSD	Detrusor sphincter dyssynergia
EAS	External anal sphincter
EMG	Electromyogram
EN	Endoneurium
EP	Epineurium
EZ	Extinction zone
FDM	Finite difference method
FEM	Finite element model
FFT	Fast Fourier transform
FVM	Finite volume model
GHK	Goldman-Hodgkin-Katz
HH	Hodgkin-Huxley
IES	Inter electrode spacing
IID	Independent and identically distributed
IRN	Inferior rectal branch of the pudendal nerve

IZ	Innervation zone
LUT	Lower urinary tract
mAChR	Muscarinic ACh receptor
MAV	Mean absolute value
MNF	Mean spectral frequency
MRG	McIntyre Richardson Grill
MRI	Magnetic resonance imaging
MU	Motor unit
MUAP	Motor unit action potential
NA	Noradrenaline
nAChR	Nicotinic ACh receptor
NDO	Neurogenic detrusor overactivity
NO	Nitric oxide
PAG	Periaqueductal grey
PCB	Printed circuit board
PE	Perineurium
PEEK	Polyether ether ketone
PerN	Perineal branch of the pudendal nerve
PMC	Pontine micturition centre
PNS	Peripheral nervous system
QoL	Quality of life
RMS	Root mean square
SCI	Spinal cord injury
SEMG	Surface Electromyography
SNR	Signal to noise ratio

Chapter 1

Introduction

1.1 Overview

This thesis presents the research carried out by the author in designing an optimised wearable neuromodulator for treating two prevalent urinary dysfunctions after spinal cord injury (SCI). This chapter aims to provide a brief motivation for what follows in the thesis. After briefly discussing the statistical prevalence of SCI, two major lower urinary tract (LUT) dysfunctions that arise after SCI are introduced. The added values of the trans-rectal neuromodulation of the pudendal nerve are briefly pointed out and the general aims of the project are summarised. This chapter concludes by summarising the thesis contributions followed by a brief summary of what follows.

1.2 SCI

SCI can be a sudden and devastating incident in one's life. It has been shown that the majority of those affected are male individuals, aged between 18 and 32 [1]. The global estimates are about 300,000 new cases every year [2]. Vehicular accidents and falls constitute the primary causes of SCI [1], showing that no one is immune. Incomplete tetraplegia and complete and incomplete paraplegia constitute more than 90 % of the cases, destroying the quality of life (QoL) for those affected [1, 2]. The cost of SCI for the individuals and society is high [1] as the treatment, management and rehabilitation are generally multifaceted.

Any solution which efficaciously addresses one or several needs of those affected greatly improves their QoL and if the solution is economical, it may remove a financial burden from the individuals and society. This is of great significance given that the statistics show that only a fraction of those affected will be employed after SCI [1].

1.3 LUT dysfunction after SCI

One of the challenges SCI patients often face is that usually SCI results in a form of urinary dysfunction as will be described in detail in Chapter 2. Namely, voiding problems and urinary incontinence are prevalent. The inadequate management of these dysfunctions may have severe consequences such as renal failure. Indeed, LUT dysfunctions constituted the leading cause of death in the individuals with SCI before the advent of the improved management techniques [3]. Thus, the significance of reliable and efficacious solutions is paramount. In terms of patients' priorities, one of the most desired function recoveries is that of the LUT [4]. This may be primarily due to issues surrounding the existing solutions, their side-effects and the severity of the burden LUT dysfunctions impose.

1.4 A disruptive solution

No single solution is available at the moment which is capable of recovering all of the bladder functions after SCI [5]. The solutions may be categorised from conservative to radical depending on how intrusive they are and the kind of risks they may expose patients to. Understandably, a more conservative solution is favoured if it is sufficiently efficacious. Due to the nature of these conditions or through time as the condition stops responding to a conservative treatment, a more radical treatment may be adopted. Based on a survey on patients' preference [6], a solution capable of recovering the full bladder function with minimal side-effects can greatly improve the QoL for those affected.

The existing solutions may include different forms of medication, catheterisation or those solutions that involve surgical operations. Professional care may be required in delivering even the conservative treatments if the lesion is at a high level of the spinal cord or if it is complete.

The wearable devices that need little or no professional supervision are of great interest as they may be augmented or upgraded at any time without the need for a constant engagement of clinical staff and their re-training. Thus, a dynamic treatment paradigm, tailored to the need of every individual may be implemented using such devices. Furthermore, the cost of a mass-produced piece of technology can be reduced to be only a fraction of the prolonged use of medication, clinical staff and surgical operations.

Therefore, a reliable and efficacious wearable device based on neuromodulation might greatly improve the QoL for those affected and may free up some of the resources for the use in the other sectors; neuromodulation is the application of the stimulus current to neural tissues to modulate the behaviour of certain neural circuits. The trans-rectal neuromodulation of the pudendal nerve via a wearable device may provide an opportunity for recovering the full bladder function after SCI via minimally invasive means with minimal side-effects. Such a device may be in place for several hours between defecation episodes, during which time the device can mechanically stop faecal incontinence if such conditions also exist.

1.5 Project aims

Devices used for the transcutaneous delivery of the stimulus current, generally, suffer from the need for high levels of the stimulus current to achieve the desired response [7, 8]. This has confined the use of such devices to therapeutic applications. The primary objective of the project was to minimise the stimulus current in the trans-rectal neuromodulation of the pudendal nerve using the state of the art computational models. The use of computational models in such problems

may greatly expedite the design procedure as one, otherwise, needs to test various designs on numerous subjects to test a hypothesis. On the other hand, a model may be readily used to test a hypothesis by varying the presumed involved elements. The challenge in developing a realistic model is to account for all of the said elements. Comparing a comprehensive modelling attempt with experimental data might be further enlightening as even the observed discrepancies may lead to a more complete understanding of the underlying phenomena. Thus, a realistic model was to be developed based on the prior experimental data to test if varying the electrode position on a trans-rectal stimulator could lead to minimising the required stimulus current. In the context of the transcutaneous nerve stimulation, where a nerve is not accessed directly like in an implant, the challenging aspect is the possible variations of the course of the nerve in different individuals and the nerve displacement in different postures of the body in the same individual. Thus, any modelling study should account for these variations. The neuromodulation of the pudendal nerve, intended to induce continence (the majority of times), may be performed conditionally to improve the efficacy as will be discussed in Chapter 2. The control signal can be the electromyogram (EMG) signal recorded from the external anal sphincter (EAS) which can be conveniently recorded using a set of surface EMG (SEMG) electrodes mounted on the trans-rectal stimulator. Although SCI patients do not possess a voluntary control over the EAS and the signal is not contaminated by that of the conscious recruitment of the muscle, the design of such electrodes for a reliable chronic use is challenging. This is due to the absence of the skin preparation in this application and the particular size and formation of the EAS. Also, the recorded SEMG signal is dependent on the design of the recording assembly. The design of such an assembly is also addressed in this thesis.

1.6 Contributions

- By thoroughly discussing the neurologic problem, for which the trans-rectal neuromodulation of the pudendal nerve may be a solution, the overall concept of the project is put into perspective.

- In terms of the presented literature review, where possible major contributions in a field are tabulated chronologically while their key features are highlighted and categorised for readers' convenience.

- The models and the underlying formulations regarding the biophysics of the phenomena under investigation are thoroughly analysed.

- A state of the art hybrid computational model of the pelvic region and the pudendal nerve are presented whose parameters are primarily based on experimental measurements. The model was used to propose a novel and optimised electrode configuration for the trans-rectal stimulation of the pudendal nerve. The modelling results are consistent with the existing data in the literature, thus, retrospectively validated. The major finding of the studies in Chapter 3 is that the required stimulus current may be reduced by 90%. If the results are corroborated in the subsequent clinical tests, the outcome of this study portrays the trans-rectal neuromodulation of the pudendal nerve using the optimised design as a viable chronic solution for controlling the target LUT dysfunctions after SCI. This can completely change the extent to which the trans-rectal neuromodulation of the pudendal nerve is currently implemented.

- A novel algorithm was developed to generate an ensemble of possible and probable pudendal nerve trajectories to study the effect of such variations in different patients and in a patient in different body postures. It was verified that the optimised design yields similar responses even when the

variations are taken into account. The aforementioned novel algorithm may be used in any similar problem.

- By a thorough theoretical analysis, a review of the existing literature and experimental measurements, an efficacious electrode assembly was proposed for the chronic EAS SEMG recording for the purpose of estimating the amplitude of the said signal.

- Using a minimum number of coefficients, a functional model of the electrode-tissue interface was developed.

The work presented in this thesis has led to the following publications:

A. Shiraz, S. Mosse, E. Solomon, B. Leaker, M. Craggs and A. Demosthenous, "Theoretical and empirical design of electrode assembly for chronic external sphincter surface electromyogram recording," *Manuscript in preparation for submission to Medical & Biological Engineering & Computing journal.*

A. Shiraz, M. Craggs, B. Leaker and A. Demosthenous, "Minimizing stimulus current in a wearable pudendal nerve stimulator using computational models," *Neural Systems and Rehabilitation Engineering, IEEE Transactions on, In press.*

A. Shiraz, B. Leaker and A. Demosthenous, "Optimization of a Wearable Pudendal Nerve Stimulator Using Computational Models," *2015 37th Annual International Conference of the IEEE Engineering in medicine and biology society conference (EMBC)*, Milan.

A. Shiraz and A. Demosthenous, "Using Computational Models to Optimize a Neuromodulator," *Bio-ElectroMagnetism for Biological and Medical Applications Workshop in 2015 45th European Microwave Conference*, Paris.

A. Shiraz, A. Vanhoestenberghe and A Demosthenous, " Optimization of neural stimulation in a device for treating urinary incontinence," *2013 IEEE Biomedical Circuits and Systems Conference (BioCAS)*, Rotterdam.

A. Shiraz and A. Demosthenous, "Towards optimized neural stimulation in a device for urinary incontinence," *2013 COMSOL Conference*, Rotterdam.

A. Shiraz and A. Demosthenous, "Conditional ano-rectal neuromodulation device for urinary incontinence," *2013 The Future Diagnostics in Life Sciences and Healthcare*, Salisbury.

A. Shiraz, A. Vanhoestenberghe and A Demosthenous, "Towards an optimized wearable neuromodulation device for urinary incontinence," *2012 19th IEEE International Conference on Electronics, Circuits, and Systems (ICECS 2012)*, Seville.

A. Shiraz, A. Vanhoestenberghe and A Demosthenous, "Design and development of a closed loop active neuromodulation device for treating urinary incontinence", *2012 Royal Academy of Engineering Young researchers futures meeting in Neural Engineering,* Warwick.

A. Shiraz, A. Vanhoestenberghe and A Demosthenous, "Stainless-steel electrode-tissue interface characterisation of conditional trans-rectal stimulator for treating urinary incontinence", *2012 3rd Annual Conference for the UK and Ireland Chapter of the International FES Society (IFESSUKI)*, Birmingham.

1.7 Thesis organisation

In this section a brief summary of every chapter and the overall progression of the presented narrative are presented.

Chapter 2: **Fundamentals of the design**. To put the overall concepts, goals and achievements into perspective and given the fact that the nature of the project is highly interdisciplinary, the fundamentals of the design are reviewed in Chapter 2 with a particular attention to the neurophysiology of the LUT.

The human nervous system and its central and peripheral divisions together with their roles are introduced. Then, from a cell level understanding of the nervous system to complex neural circuits mediating different functions, the key features of the human nervous system are discussed. A particular attention is paid to the fundamentals of the neural signal generation and propagation as these are the central concepts in the subsequently presented modelling studies in Chapter 3. Where possible, analytical models are used to gain a functional understanding of the underlying principles.

At the next stage, the neurophysiology of the LUT and its functions are introduced. It is further discussed how and why SCI may interrupt the normal behaviour of this unit. After discussing different treatment and management solutions, the pudendal nerve neuromodulation as a promising method is presented. A comprehensive review of the key contributions in the literature regarding the application of the stimulus current to the pudendal nerve is presented in a tab-

ular format and in a chronological order while the main features of every cited contribution are highlighted. Finally, the target solution is discussed in more detail while challenges faced and the motivation for the work presented in the subsequent chapters are mentioned.

Chapter 3: **Stimulation compartment design**. After a review of analytical models of an excitable tissue, volume conductor models are discussed. These models when used in tandem with the Hodgkin and Huxley (HH) type models of excitable tissues are referred to as hybrid models. The fundamental features and variables in each model are presented and the selected choices of different elements in the models are justified. The activating function (AF) and its heuristic use are introduced. A thorough review of the use of hybrid models in the literature for various applications are presented. The subsequent sections of this chapter discuss the experiments and models performed and developed, respectively, to optimise the stimulation compartment.

A trans-rectal stimulation study used to approximate the conductivity of the media surrounding the stimulator *in situ* and a magnetic resonance imaging (MRI) study performed to form a three dimensional (3D) understanding of the pelvic region and the course of the nerve are presented. The development of the hybrid model of the pelvic region and the pudendal nerve are discussed in detail. The validity of the model with respect to the numerical methods used, the boundary conditions adopted and approximations made are verified. A multi-electrode model is made to investigate the effect of varying the electrode configuration. It is shown that a specific electrode configuration requires a considerably lower stimulus current level to induce the required response. A novel algorithm is shown to investigate the effects of the nerve variation on the required level of the stimulus current. It is shown that for an ensemble of probable and possible variations a specific configuration consistently results in a low required stimulus current level.

Chapter 4: **SEMG compartment design**. After an introduction to the fundamentals of SEMG signals, the functional models of the generation and propagation of the SEMG are discussed. A complete understanding of such models is instrumental in understanding the underlying principles of the design. The system level models of the recording apparatus, including the frequency response of the electrodes and the recording arrays are then presented. SEMG amplitude (the feature of interest) estimation methods are discussed while the choices made are analytically justified. After a review of the contributions in the literature regarding the SEMG recording from the EAS, the significance of the electrode-tissue impedance in designing a bio-potential recording apparatus and how it may be modelled are described in detail.

Through a thorough examination of the effects of different design parameters, the making of a set of four prototypes with different design features are proposed, so by testing them *in vivo*, both of the theoretical and empirical design considerations are evaluated. Their making and the experimental protocol and setup are shown, subsequently. Stainless steel electrodes are used in all the prototypes.

A partially processed set of data acquired from the prototypes *in situ* is shown for each test prototype. A prototype yielding the most correlated SEMG signal with the muscular activity is selected. By post-processing the acquired data, the appropriate design features are derived. Finally, the electrode-tissue interface for a pair of electrodes similar to the selected ones are modelled using an RC ladder equivalent model of a constant phase element (CPE). Thus, all the features of the SEMG recording compartment are carefully designed and analysed.

Chapter 5: **Conclusions and the future directions**. After summarising the contributions and achievements of the thesis, the possible improvements of the presented work are discussed. Future directions in the development of the proposed optimised design with a reference to the ongoing developments are proposed.

Chapter 2

Fundamentals of the design

2.1 Introduction

In this chapter, the fundamentals of the target solution are discussed. The audience of the presented content is an engineer with a limited neuro-physiological knowledge. The presented information is kept at a minimum level required to understand the underlying motives for the presented attempts and achievements. After an overview of the human nervous system and the neurophysiology of the LUT, the pathology of the LUT after SCI, as related to the target solution presented in the thesis, is discussed. Namely, the neurogenic detrusor overactivity (NDO) and detrusor sphincter dyssynergia (DSD), as the primary target neurologic conditions are discussed. After reviewing some of the main existing solutions, the pudendal nerve neuromodulation as a possible solution is explored in detail and the key related contributions in the literature are presented. Finally, the target solution in terms of the overall concept and the challenges on the path of its implementation are discussed to put the presented work in this thesis into perspective.

2.2 Human nervous system

In this section, the human nervous system, its divisions and major attributes as well as the general nomenclature required are reviewed.

2.2.1 Central and peripheral divisions

Anatomically, at the highest level, the human nervous system is divided into the central and peripheral parts. The central nervous system (CNS) comprises the brain and the spinal cord while the peripheral nervous system (PNS) mainly includes the nerves that connect the periphery of the body to the CNS. The brain comprises the cerebral hemispheres, diencephalon, cerebellum, and the brainstem. The spinal cord is divided into four sections, each of which has various segments: cervical (C1-C8), thoracic (T1-T12), lumbar (L1-L5), and sacral (S1-S5) [9, 10]. Figure 2.1 shows the different components of the CNS.

The PNS comprises the spinal nerves, originating from the spinal cord, and a part of the cranial nerves, originating directly from the brain [9,10]. The peripheral nerves originating from a specific segment of the spinal cord (C-S) generally mediate a specific functionality [11]. PNS innervations pertinent to the target solution presented in the thesis will be covered later in this chapter.

2.2.2 Fundamental elements of nervous system

There are two main classes of cells in the nervous system: nerve cells (neurons) and glial cells (glia). Generally, the former are the ones involved in neural signalling and the latter function as support cells [9–11]. The following sections describe these elements in more detail.

Neuron

Typically, the morphology of a neuron may consist of four distinct regions: a soma, dendrites, an axon, and presynaptic terminals [9]. These regions are shown in Figure 2.2. The main function of neurons is to convey the neural signal, the

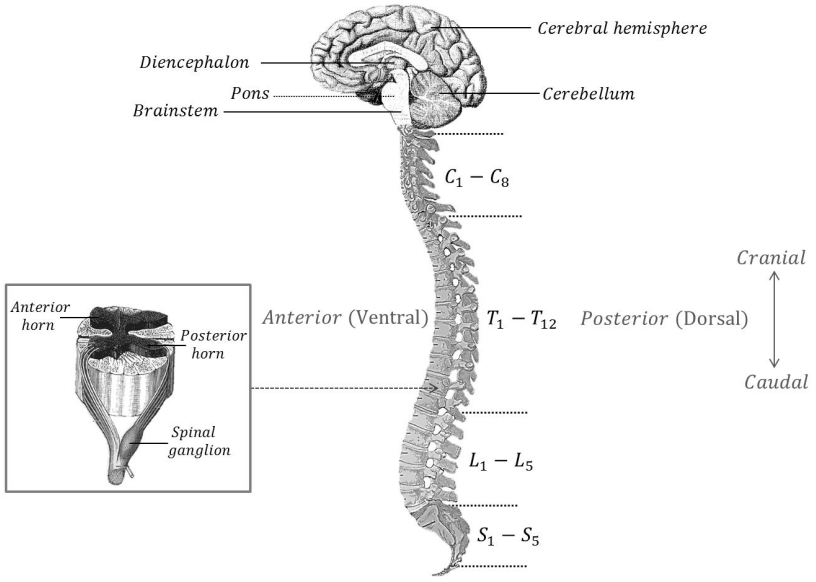

Figure 2.1: Human central nervous system. The brain and its main components and the different sections of the spinal cord are shown. The anatomical terms of direction which are referred to later in the thesis are also shown. Inset shows a cross-section of the spinal cord and its main features. Different segments of the figure were adapted from [12] to construct the presented figure.

action potential (AP), which will be discussed in detail later in this chapter. The soma holds the nucleus, in which the genes of cells exist, and endoplasmic reticulum, in which cells' proteins are synthesised. A soma, usually, gives rise to two types of projections, also referred to as processes. Typically, there is one long (0.1-3 m) axon [10], also referred to as the nerve fibre, which acts as the main long conducting unit of the neural signal (AP) to the other neurons. The other type of projections, which are generally shorter and branch-like, are dendrites. Dendrites typically act as the main signal receiving ports in a neuron. Generally, near the end, an axon divides into these branches which communicate with other neurons through the presynaptic terminals. The point of communication between a neuron and other neurons is called a synapse. The cell transmitting the signal is called a presynaptic cell and the one receiving it is called the postsynaptic cell. Presynaptic terminals land on the soma and/or the dendrites of a subsequent cell [10].

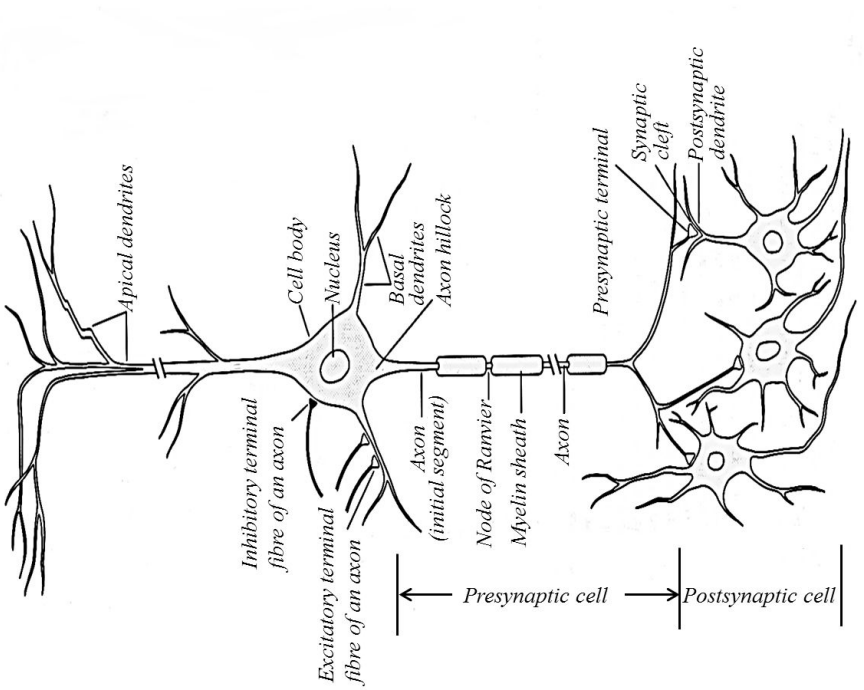

Figure 2.2: A typical motor-neuron. The main regions as referred to in this chapter are shown. Figure adapted form [10] with changes.

In terms of the functionality or the direction of conveying the neural signal, neurons are classified into three major groups: afferents, meaning conducting inwards or towards, efferents, meaning conducting outwards or away, and interneurons. Afferents carry information from the periphery of the body to the CNS. These neurons are very often interchangeably referred to as sensory nerves. However, it should be noted that all afferent communications may not lead to a form of sensation. Efferents or the motor fibres carry the neural signal and commands from the CNS to muscles and glands. Interneurons, which are neither sensory nor motor, constitute the largest group of neurons. Interneurons convey APs over long or short distances from a neuron to the other [9, 10].

In terms of the number of the processes originating from their soma, neurons are classified as unipolar, pseudo-unipolar, bipolar or the most common multipolar cells. In the unipolar cells, a single primary process exists which serves as the axon of that cell. The axon is then branched into the receiving dendrites. This type of cell can be found in the autonomic nervous system. Bipolar neurons

(e.g., the bipolar cell of retina) with an oval shaped soma have two processes originating from them. Many afferents are of this type in which the dendrites convey the signal from the periphery of the body and the axon relays the information to the CNS. A variation of this type of neuron is the pseudo-unipolar cell (e.g., the ganglion cell of the dorsal root) that initially develops as bipolar and later the processes merge to form an axon emerging from the soma. This single process then splits in two branches, one of which conveys the neural signal from the periphery and the other conveys it towards the spinal cord. Multipolar cells (e.g., motor neurons of the spinal cord), typically, have many dendrites emerging from various points around their soma and have a single axon. All the variations discussed above are primarily related to the functions of the cells [9–11].

Glia

The more populous, 10-50 times [10], cells in the nervous system compared to neurons, glial cells, surround neurons and have various functionalities. Glial cells act as the general and structural support for neurons. Schwann cells and oligodendrocytes insulate axons in the PNS and CNS, respectively [10]. Schwann cells form the myelin sheath which essentially acts as an insulation around a nerve fibre. Fibres may be myelinated or unmyelinated and, consequently, they show different characteristics as discussed further in this chapter. In a myelinated fibre, large segments along its length are wrapped by layers of myelin while only small segments between the wrapped segments are left exposed at regular intervals. The exposed segments are referred to as the nodes of Ranvier [9–11].

Astrocytes, the other type of glial cells, are thought to have various roles such as bringing nutrients to neurons in the CNS and providing the blood-brain barrier. Another function of astrocytes, more relevant to what follows in this thesis, is to help maintain the right potassium ion concentration in the extracellular space of neurons. They have a similar role in regulating synaptic activities by absorbing neurotransmitters. There is another class of glial cells, microglia as opposed to

macroglia discussed so far, which is thought to be only recruited during infection, injury, and seizure [10].

Key terms in neuroanatomy [9–11, 13]

Generally, there are two *root*s originating from the spinal cord. The dorsal root conveys the sensory information while the ventral root conveys the motor signalling. The dorsal root then enters into the dorsal root ganglion, having a pseudo-unipolar cell. In the PNS, a local accumulation of cell bodies and supporting cells is referred to as the **ganglion**. Peripheral axons are generally bundled into what is called **nerves**. The nerves from the dorsal and ventral roots merge after those of the dorsal root exit the dorsal root ganglion to form the spinal nerve. The spinal nerve is then branched into the anterior and posterior **rami**. Further, a branching network of the nerves may be formed which is referred to as the **plexus**. These terms will be referred to at the subsequent stages of the thesis.

The nerve cell bodies in the CNS may be arranged in two ways. The ones in the first group are the nuclei, the local accumulations of neurons with similar connections and functionalities, such as the collections found in the cerebrum, brainstem, and spinal cord. The second arrangements are cortices which are sheet-like array of cells such as those found in the cerebral hemispheres and cerebellum. The axons in the CNS are gathered into **tracts**, analogous to the nerve in the PNS. Tracts that cross the mid-line of the brain and spinal cord are referred to as **commissures**. The **grey matter** refers to any accumulation of cell bodies and neuropils (synaptically dense regions of dendrites, synaptic terminals, and glial cell processes) in the brain and spinal cord (e.g., nuclei or cortices) while the **white matter** refers to tracts and commissures.

The above-mentioned terms are some of the key anatomical terms related to what follows in this thesis. There are functional classifications as well that should be understood in the subsequent discussions. The PNS may be subdivided into the

autonomic nervous system and **somatic** nervous system. Generally, the former is in charge of the involuntary control and the latter provides the voluntary control. The autonomic nervous system may be further divided into the **sympathetic** and **parasympathetic** nervous systems. The sympathetic nervous system is generally perceived to be in charge of the *fight-or-flight* response while the parasympathetic nervous system is responsible for the *rest-and-digest* functions. An important anatomic feature of the sympathetic nervous system is its **paravertebral** and **prevertebral** ganglia, the latter of which is positioned close to the innervated organs. A paravertebral ganglion in the sympathetic trunk is connected to the corresponding spinal nerve via the **white** and **gray rami** communicants. A more detailed description of these divisions is beyond the scope of the thesis but in relation to the target application their role will be described in more detail.

Having discussed the main functional entities and terms, the subsequent section describes the idea of neural circuits in the nervous system.

Neural circuits, receptors and transmitters

Neurons are organised to form neural circuits and reflexes which process the sensory information and elicit motor responses. A typical circuit on the afferent end may be terminated by sensory receptors. These are nerve endings which transduce a specific stimulus energy into the corresponding receptor potential. Receptors are specialised in terms of the energy they transduce which may be electromagnetic, mechanical, thermal or chemical [14]. A complex sensation such as pain may recruit different receptors. The receptor potential then travels along the attached afferent fibre with a specific AP firing pattern. Given the specificity of the receptors, the attached afferents may covey a specific mode of sensation as well. Thus, by artificially inducing APs at an appropriate frequency or a given signalling pattern in the attached fibre, the corresponding sensations could be induced artificially. The cell bodies of these afferents may be in the corresponding

ganglia. The central axon of the mentioned cell might enter through the dorsal horn of the butterfly-shaped grey matter of the spinal cord and synapse with central neurons. Namely, it may synapse with interneurons or motoneurons in the spinal cord.

The basic forms of the synaptic transmission between neurons are electrical and chemical while the majority of the transmissions are chemical [10]. While at an electrical synapse a low resistance electrical path exists between the two associated cells, at chemical synapses neurons are separated completely by a small space called the *synaptic cleft*. The entities that essentially pass the neural signal from a presynaptic cell to a postsynaptic cell are called neurotransmitters (e.g. acetylcholine (ACh)). The arrival of an AP at the presynaptic side of a synapse leads to the release of chemical neurotransmitters which then diffuse across the cleft and interact with the receptors of the postsynaptic side [10]. The mentioned interaction leads to either excitation or inhibition. The former case leads to the suppression of the AP generation while the latter leads to the generation of APs. The type of the resulting action, primarily, depends on the type of the transmitter and receptor involved. Also, it should be noted that the synaptic input may add up from various presynaptic cells.

The sensory information may be conveyed through the white matter of the spinal cord to different regions in the brain for further processing. In which case, the response of the brain may be conveyed back to the target cells through different regions of the white matter of the spinal cord. A spinal reflex on its own may result in a motor activity without any modulatory input from the brain. A well-known example of this case is the myotatic reflex, commonly known as the knee jerk reflex [10]. Through the ventral horn of the gray matter, efferent fibres leave and land on target muscles or organs. At a neuromuscular junction, neurotransmitters are released and the corresponding contraction or relaxation effects are mediated.

As mentioned above, the chemicals involved in the neural transmission and re-

ception at the point of a synaptic contact determine the nature of the resulting effects induced. The ACh neurotransmitter plays a significant role in the control of the LUT. A transmission involving ACh is referred to as cholinergic. The corresponding receptors in a cholinergic transmission may be muscarinic (mAChR) or nicotinic (nAChR) [9]. Adrenergic neurotransmitters and the corresponding receptors are the other key elements in this context which are discussed in this chapter.

Understanding the fundamentals of neural circuits is instrumental in designing the solutions which are intended to modify a neurologic problem. Neural circuits may be very complex and in a given circuit many inputs and interactions may not be known.

The existing understanding of some neural circuits may be conjectural or based on the studies on other species as will become clear in the case of the neural circuits controlling the LUT.

2.2.3 AP

Having presented an overview of different elements and aspects of the human nervous system, the AP as the most fundamental phenomenon in the nervous system is discussed in detail here. An AP is a rapid (∼1 ms) variation (∼100 mV) of the transmembrane potential. APs are naturally triggered in the initial segment of the attachment of an axon to its corresponding soma (i.e., axon hillock) and travel down the axon at velocities ranging from 1 to 100 m/s depending on the fibre type [9]. The AP generation is an all-or-none process, meaning that an active rise of a specific extent in time and amplitude in the transmembrane potential (V_m) is triggered if V_m exceeds a threshold whilst any relatively smaller variation does not yield such a response. The AP then propagates down the axon owing to the fact that it raises the transmembrane potential above the threshold in the adjacent segment of the axon, resulting in the generation of an AP in that segment. The underlying dynamics of the AP propagation are discussed further in

this chapter. Different activities are mediated via this highly stereotyped signal throughout the nervous system by the neural circuits mentioned before. The actual command or information is not perceived by the variation of the signal (i.e., AP) but different effects are mediated through the paths APs travel and their firing pattern [9].

The temporal variation of APs

Generally, there are three main temporal sections in an AP. The resting potential, the transmembrane potential in the absence of any stimuli, is a negative value. The origins of this potential will be discussed in detail in the subsequent sections. Upon an increase in the transmembrane potential beyond the threshold value, V_m rapidly increases to a specific positive value. This phase is called the depolarisation period. The depolarisation phase is followed by the subsequent reduction in the transmembrane potential which is called the repolarisation phase. The transmembrane potential reduces even below its initial resting potential for a period of time which is referred to as the hyperpolarisation phase. Finally, V_m returns back to its initial value after a period of time. The sequence of these variations contributes to the way an AP propagates in the nervous system and more specifically along a nerve fibre. The above-mentioned sequence is the most general view of the temporal variations. More subtle variations are referred to in Chapter 3. The general temporal variations of APs are shown in Figure 2.3.

AP generation

The generation and propagation of APs are generally mediated by voltage-gated ion channels. These channels are ion specific, meaning that when they are open they are only permeable to a specific ion. Also, the state that these channels are at depends on the transmembrane potential. To better understand the nature of an AP features such as its amplitude and the underlying chemical mechanisms, the Nernst formulation is described in more detail here.

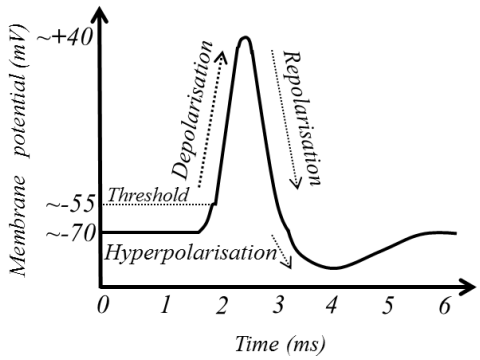

Figure 2.3: A general view of the temporal variations of an AP.

Supposing that two media are separated by an ion specific channel and the density of that ion is different in the two media, ion flows against the concentration gradient. It is noted that ions do not exist in isolation, meaning that a positive ion is paired with a negative one. Thus, as the ions that the barrier is permeable to diffuse, an electric field is built up in the direction of the concentration gradient. The opposing forces of the concentration-dependant diffusion and electric field reach an equilibrium, at which stage there is no net ion flow. By equating these opposing forces, the transmembrane electric potential at which the equilibrium is reached can be calculated as shown in Equation 2.1 which is referred to as the Nernst equation. This concept is central in many bioengineering concepts. Namely, it is also revisited when the electrode-tissue interface is addressed.

$$V_{Nernst} = \frac{RT}{zF} ln(\frac{[X]_2}{[X]_1}) \tag{2.1}$$

where R is the gas constant (8.314 $[J.K^{-1}.mol^{-1}]$), T is the temperature [K], z is the valence of the ionic species, F is the Faraday's constant (96485 $[C.mol^{-1}]$), and $[X]_1$ and $[X]_2$ are the concentrations of the ion in the first and second media, respectively. It should be noted that V_{Nernst} is measured from medium 1 to 2. In the context of a nerve cell, the secondary medium is the extracellular space and the first medium is the intracellular space. Thus, a higher concentration of a positive ion outside the cell results in a positive Nernst voltage for that ion.

Where several ion species are present, the transmembrane potential can then be calculated using the Goldman-Hodgkin-Katz (GHK) formulation [15] as shown in Equation 2.2.

$$V_m = \frac{RT}{F} ln(\frac{\sum_i^n P_{X_i^+}[X_i^+]_2 + \sum_j^m P_{X_j^-}[X_j^-]_1}{\sum_i^n P_{X_i^+}[X_i^+]_1 + \sum_j^m P_{X_j^-}[X_j^-]_2}) \tag{2.2}$$

where $P_.$ is the permeability of the membrane to a given ionic species referred to in the subscript. Building on the Nernst equation, the GHK formulation may be intuitively understood. If the membrane becomes more permeable to a specific species, the equilibrium potential tends to the Nernst potential of that species. The defining variables as shown in Equation 2.2 are the permeabilities and concentrations involved. The permeabilities are governed by the voltage-gated channels mentioned before. The functions of the channels should be discussed briefly with a reference to the realistic fibre characteristics. The pioneering work [16] of HH laid the foundation for the existing systematic understanding of the channel mechanisms. The HH model of the channel dynamics is presented in detail in Chapter 3. These channels have gates that depending on the voltage across them the rate at which they open or close varies. For a channel to conduct, all its gates should be open. The major ions involved are sodium and potassium with their respective selective channels. The concentration of the sodium ions in the extracellular space is much more than those in the intracellular space while that of potassium ions is the other way round [10]. Therefore, the opening of the sodium channels results in a rise of the transmembrane potential while the opening of the potassium channels results in its reduction. The resting potential is due to the permeability of the membrane to the existing ions. The resting potential is not a case of equilibrium but that of the steady state [10]. As the rest potential is negative, this means that the membrane is more permeable to the ions with negative Nernst potentials.

To understand how the voltage-gated ion channels behave as they do, the micro-

physiology of these channels and the cell housing them are briefly discussed here [10]. The surface of the cell membrane is formed by a lipid bi-layer about 6-8 nm thick which is hydrophobic. The ions involved are hydrophilic due to their electrostatic interactions with the dipolar water molecules. It should be noted that smaller ions interact more strongly with water molecules to form larger water shells around them. The ion channels are some proteins that span the cell membrane and owe their selectivity to a pore-diameter based molecular sieving and specific chemical interactions. The transmembrane potential acts on a component of a voltage gated ion channel that has a net charge an consequently results in a conformational change. The other important feature in generating APs at a molecular level is the active transporter. The active transporter, which is classified based on its source of energy (e.g., ATPase pumps), moves the ions against the concentration gradient to maintain a given concentration of the ions after every AP event [9]. This process takes several milliseconds.

The information presented up to this point can facilitate the better understanding of the underlying mechanisms leading to the generation of an AP. Assuming that only sodium and potassium ions are involved, a full cycle of the AP generation is described as follows [9,10]. The inputs in an axon hillock raise the transmembrane potential beyond a threshold at which point the permeability of the membrane to sodium and potassium ions increases. The conductivity of sodium channels increase faster than those of potassium ions. Thus, the influx of sodium ions brings the transmembrane potential closer to the equilibrium potential of sodium ions. At the higher transmembrane potentials, the conductivity of the membrane to potassium ions increases while sodium channels start to inactivate, reducing the membrane permeability to sodium ions. This results in repolarisation of the membrane. The inactivation of sodium channels and the prolonged permeability of the membrane to potassium ions result in the lowering of the membrane potential below the resting potential and closer to the equilibrium potential of potassium ions.

This summarises the typical mechanisms in the generation of APs. Several more channel types may be involved in different species but the overall process is generally similar.

The other important feature of an AP is the characteristics of the refractory period succeeding the AP. There exists the absolute refractory period in which no action potential may be triggered in the segment of the membrane under question. This is followed by the relative refractory period during which period a stronger than normal stimulus may produce a new AP [17].

Artificially induced AP

APs may be generated artificially. This can be achieved by piercing the membrane and injecting positive charges into the intracellular space. Upon such an intervention in an axon, two APs are generated, travelling away from the injection point. The case of the extracellular stimulation is more subtle but can be understood easily based on what has been presented so far. The case of a bipolar extracellular source is shown in Figure 2.4a. The ionic current induced by the source depletes the extracellular space of negative ions in the vicinity of the cathode. This, increasing the transmembrane potential near the cathode, generates an AP near it. This schematic representation of the underlying processes helps in understanding the way an AP is generated.

AP propagation

Assuming an AP is generated, naturally or artificially, the AP automatically induces the generation of other APs in its vicinity. Considering unmyelinated fibres, as shown in Figure 2.4b, the extracellular and intracellular current flows along the fibre induce an increase in the transmembrane potential in the vicinity of the depolarised segment. When the AP is induced in a segment of the fibre naturally, the preceding segment is in the hyperpolarisation phase, thus, the AP travels in a specific direction. In the case of a myelinated fibre, as the current

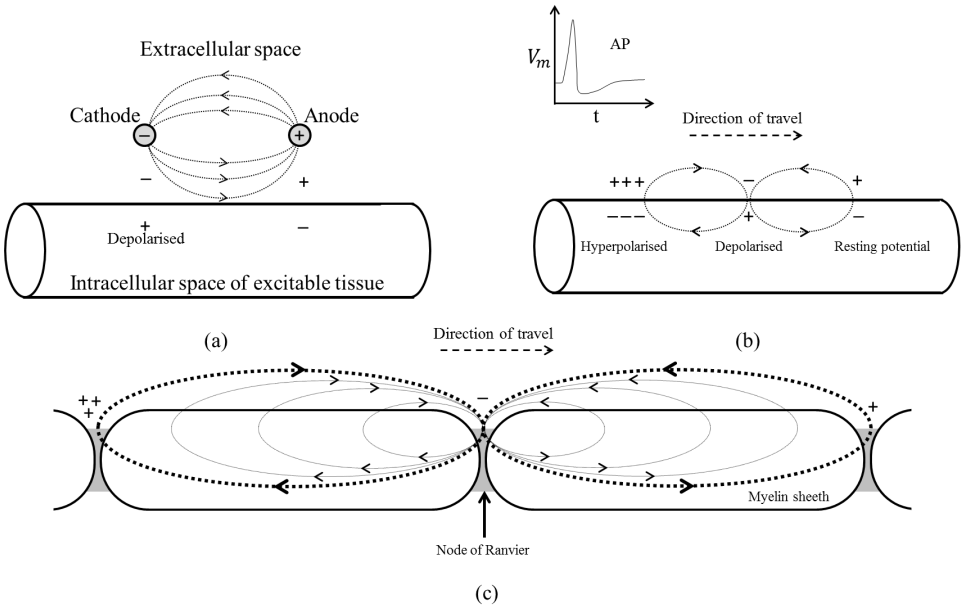

Figure 2.4: Generation and propagation of APs in myelinated and unmyelinated fibres. (a) shows the extracellular stimulation of an unmyelinated fibre. (b) shows the propagation of an AP in an unmyelinated fibre while (c) shows the propagation of an AP in a myelinated fibre.

loops are relatively weak where the myelin insulation is present, the loops are at their highest intensity from a node to the other, resulting in the AP essentially hoping from a node to the other, rendering the transmission much faster.

Predicting the exact dynamics of the natural or artificial generation of APs requires a complete understanding of the underlying neural mechanisms and stimulus properties. These features are explored in more detail in Chapter 3. Having established the fundamentals of the AP generation and propagation, the following section reviews how these features are affected by the fibre size.

Fibre size

The speed at which APs travel in fibres, their conduction velocity (CV), significantly differs if they are myelinated or not for the reasons mentioned above. The fibre size also may affect such features. Larger fibres show higher CVs and excitability. The latter means that a less intensive stimulus current is required to generate an AP. In this section, the underlying principles of the aforementioned

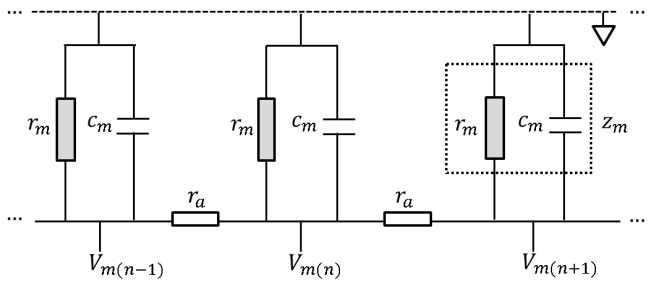

Figure 2.5: A simple cable model of an excitable tissue for a given length. r_m is the transmembrane resistance, c_m is the lipid bi-layer capacitance. The parallel combination of r_m and c_m are referred to as z_m. r_a is the axial resistance of the fibre. The extracellular potential is approximated to be the same and zero everywhere. Thus, the intracellular potential is equal to the transmembrane potential, V_m. In this model active channels are not considered but even in their presence the concepts referred to here can be extended.

phenomena are explored. The analytic models of nerve fibres are discussed in Chapter 3 but here they are touched upon to better understand the effect of the fibre size. A segment of a nerve fibre may be modelled as shown in Figure 2.5 for a unit length where r_m and c_m are transmembrane resistance $[\Omega.cm]$ and capacitance $[F/cm]$, respectively, while r_a is the axial resistance $[\Omega/cm]$. First, the variations of the aforementioned parameters with the variations of the fibre radius (a) should be considered. Considering the formulations of the parallel plate capacitance and the resistance of a cylindrical medium, it is trivial to show that the relations shown in (2.3) hold.

$$\begin{aligned} r_m &\propto a^{-1} \\ r_a &\propto a^{-2} \\ c_m &\propto a \end{aligned} \tag{2.3}$$

A larger z_m results in a higher V_m for a given transmembrane current. Based on 2.3, it is also trivial to show that the transmembrane impedance is inversely proportional to the radius. Thus, it may sound counter-intuitive that larger fibres

require less current to generate APs. However, it should be noted that the above mentioned model does not take into account the active ion channels, which are also uniformly distributed on the surface of a fibre. Thus, more channels exist and consequently more current is pumped in larger fibres which results in an increased excitability.

Demonstrating the effect of the fibre size on the CV is more subtle. It was mentioned that every depolarised segment raises the transmembrane potential in the subsequent segment. The purpose of the following original analysis shown in (2.4) is to find out the time constants involved. Considering the simple potential divider configuration in which $V_{m(n)}$ is divided to produce $V_{m(n+1)}$, the following can be shown:

$$\begin{aligned} V_{m(n+1)} &= V_{m(n)} \frac{\frac{\frac{r_m}{scm}}{r_m+\frac{1}{scm}}}{r_a + \frac{\frac{r_m}{scm}}{r_m+\frac{1}{scm}}} \\ &= V_{m(n)} \frac{1}{sr_a c_m + \frac{r_a}{r_m} + 1} \\ &= V_{m(n)} \frac{1}{\frac{r_a}{r_m}+1} \frac{1}{\frac{s}{\frac{1}{r_m c_m}+\frac{1}{r_a c_m}}+1} \end{aligned} \tag{2.4}$$

where s is the Laplace variable. This shows two time constants, one of which is dependent on the fibre diameter ($\tau_1 = r_a c_m$) and the other is not ($\tau_2 = r_m c_m$). By obtaining the inverse Laplace transform of the final expression in (2.4), it can be shown that $V_{m(n+1)} = V_{m(n)} \frac{1}{\tau_1} e^{-t(\frac{1}{\tau_1}+\frac{1}{\tau_2})}$. Thus, when $V_{m(n)}$ is applied to the n^{th} segment of a fibre, an increase in the fibre diameter increases the amplitude of $V_{m(n+1)}$ and how fast it decays in time. Although this is a simplistic representation of a fibre, it shows that the fibre diameter may affect certain features of the travelling signal. Indeed, active and passive properties of fibres affect their CVs [18].

Depending on the size and CV of fibres, Erlanger's system ($A_{\alpha,\beta,\gamma,\delta}$, B and C) and Lloyd's system (I, II, III and IV) have been proposed for a classification of fibres based on the aforementioned features [14]. Erlanger's system is used for

Table 2.1: Fibre classifications [9, 10, 14].

Type	Diameter (μm)	Velocity (m/s)
A_α	8-20	50-120
A_β	5-12	30-75
A_γ	2-8	10-50
A_δ	1-5	3-36
B	1-3	3-15
C	0.2-1.5	0.5-2
I	12-20	70-120
II	4-12	24-70
III	1-4	3-24
IV	0.2-1.5	0.4-2

motor nerves whose fibres are generally in groups A_α and A_γ and for cutaneous afferents mostly in groups A_β, A_δ and C. However, Lloyd's system is generally implemented for the afferents from the receptors in muscles which are usually in groups I and II. Thus, groups III and IV are not used [14]. Table 2.1 shows the CV and diameter ranges for different classes of fibres. Having established the fundamentals of the human nervous system, the neuro-physiology of the LUT, related to the target application of this thesis, is discussed in the subsequent section.

2.3 Neuro-physiology of the LUT

Main functions

The main functions of the LUT are to store and periodically void urine [19]. These functions are performed by the main functional units of the LUT. These functional units include the urinary bladder and an outlet consisting of the bladder neck and urethra [20]. The urinary bladder is engulfed in a smooth muscle called the detrusor while the urethra, the projecting tube from the bladder, is composed of smooth and striated muscles. During the storage phase, the urinary bladder relaxes while its outlet contracts and during the voiding phase the bladder contracts while the outlet relaxes. These synergic and reciprocal activities of

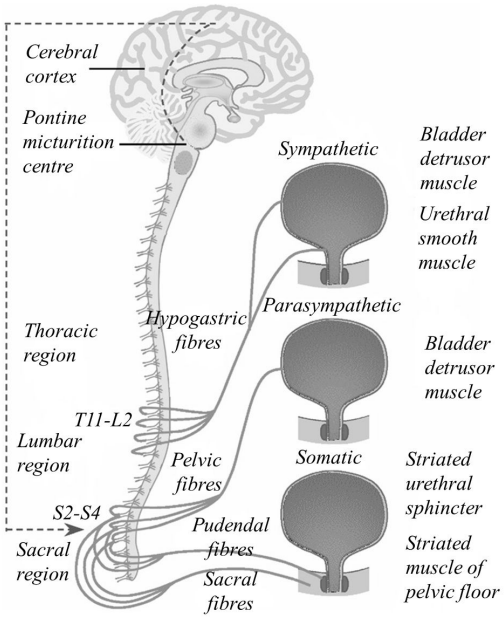

Figure 2.6: The schematic of LUT neural pathways. The inhibitory and excitatory nature of the reflexes are discussed in the text. Figure adapted from [22] with changes.

the functional units are controlled by complex neural circuits. The neural circuits are primarily controlled in the brain, spinal cord, and peripheral ganglia [21]. The intricacy of the neural circuits is partly due to the fact that the LUT functions are under the somatic as well as autonomic control and partly due to the required switching action between the aforementioned reciprocal activities [20].

The current understanding of the neurophysiology of the LUT is based on the studies on human and other species [20, 21]. The following lines provide a general overview of the neurophysiology of the LUT to put what follows in the thesis into context. A more elaborate and detailed review of the underlying studies can be found elsewhere [5, 20, 21].

Sympathetic, parasympathetic and somatic innervation

Figure 2.6 shows some of the neural pathways which are thought to be involved in the control of LUT functions and Figure 2.7 shows a close-up view of the LUT and the receptors and neurotransmitters that are involved in controlling it. The

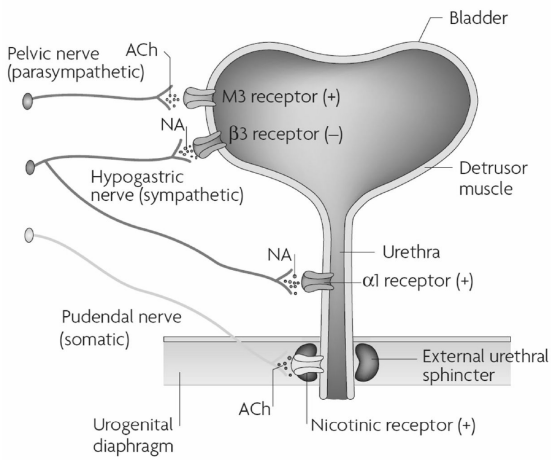

Figure 2.7: The LUT, its motor innervation and the receptors and neurotransmitters involved. Figure adapted from [20].

autonomic nervous system controls the LUT through the sympathetic nervous system, primarily via the hypogastric nerve, and parasympathetic nervous system, primarily via the pelvic nerve [20, 21]. The somatic control of the LUT is mediated by the pudendal nerve [20, 21]. It is generally thought that the activation of the sympathetic nervous system is responsible for maintaining continence while the activation of the parasympathetic system facilitates voiding [22]. Before discussing the reflexes which are thought to be involved, the presumed efferent innervation of the LUT via the mentioned systems and nerves is briefly discussed here, followed by a general overview of the afferent innervation of the LUT.

In the sympathetic system, the pathways originating from T11-L2 spinal segments, after passing through the paravertebral ganglia, pass to the prevertebral ganglia. The prevertebral ganglia are located in the superior hypogastric and pelvic plexus. These pathways also pass to short adrenergic neurons in the bladder and urethra [21]. These nerves release noradrenaline (NA) to activate β adrenergic receptors in the bladder wall to inhibit detrusor contractions. NA is also released to activate α adrenergic receptors in the urethral smooth muscle and the bladder neck to excite them [20]. In the parasympathetic system, pathways originate from the sacral segments, travelling in sacral roots and the pelvic nerve to ganglia in the pelvic plexus and the bladder wall from which post-ganglionic

nerves arise [20]. By releasing ACh to activate mAChRs in the bladder wall, an excitatory effect in the detrusor is achieved [21]. Adenosine triphosphate (ATP) has been shown in different animal studies to mediate a non-cholinergic excitatory effect as well [21]. Furthermore, in various species nitric oxide (NO) has been shown to be the inhibitory transmitter involved in inducing the relaxation of the urethral smooth muscle [20, 21]. The somatic motor pathways, arise from the sacral spinal segments and motor neurons in Onuf's nucleus and reach the external urethral sphincter via the pudendal nerve [20]. The origin of these pathways has been shown to be different in animals [21]. ACh neurotransmitters and nAChRs are involved in the somatic excitatory input to the external urethral sphincter [20].

Afferent innervation

Afferent fibres, conveying information from the LUT to the corresponding central neurons, can be found in the pelvic, hypogastric and pudendal nerves [20, 21]. These afferent fibres consist of myelinated A_δ and unmyelinated C fibres [5,20,21]. Different classifications of nerve fibres were mentioned earlier in this chapter. As will be shown in the subsequent section, apart from the conscious sensory information, the afferents of the LUT are thought to play an integral role in controlling LUT functions. Based on studies on cats and rats, it has been shown that A_δ fibres are generally mechano-sensitive while C fibres are nociceptive [21]. Regarding the afferents to the outlet, pudendal afferents have been shown to be sensitive to the passage of liquid through urethra in rats [21]. Furthermore, the central terminations of pudendal afferent pathways and the pathways from the external urethral sphincter of cats, rats and monkeys converge in part with those of bladder afferents [21].

This summarises the entities involved in afferent activities of the LUT and will be revisited in the subsequent sections where the continence mediating and voiding reflexes as well as neurogenic problems after a lesion are referred to.

Storage and voiding phases

Owing to intrinsic properties of the detrusor, intravesical pressure is kept at low and relatively constant levels during the storage phase [21]. Furthermore, the suppression of the parasympathetic outflow and in some species the activation of sympathetic efferents may promote continence [21]. It has also been shown that pudendal efferent activities further mediate continence [21]. Upon voluntary decision for voiding in healthy adults, the sympathetic and somatic outflows are inhibited and the parasympathetic efferents are activated to facilitate voiding by an initial relaxation of the outlet and the subsequent contraction of the reservoir [20, 21]. Various positive and negative feedbacks in voiding and storage phases, respectively, through intricate neural circuits at spinal and supra-spinal levels are involved in mediating the desired functions.

Low-level vesical afferent activities activate a spinal sympathetic reflex that promotes continence [21]. As mentioned, pudendal efferent activities are present during the storage phase. These activities, which further promote continence, are partly mediated by a spinal reflex, referred to as the guarding reflex. Similar to the sympathetic reflex, a low level bladder afferent activity initiates this reflex [21]. Studies on cats suggest that supra-spinal inputs may also result in pudendal efferent activities [20, 21]. An effect more pertinent to the target application of this thesis is that the afferent activity resulting from the contraction of the external urethral sphincter may act as the input to another reflex which further promotes continence [23–26].

Based on animal studies the pontine micturition centre (PMC) and periaqueductal grey (PAG) in the brain may be involved in controlling micturition [20, 21]. The PMC activates the descending pathways that result in urethral relaxation and the activation of the parasympathetic outflow, creating a spinobulbospinal reflex to mediate voiding [20, 21]. Also, the flow of urine in the urethra produces afferent activities that further facilitate voiding through secondary reflexes [20].

The PAG projects to many regions of the brain and is thought to pass sensory information to higher parts of the brain, have an input to the PMC and modulate the onset of voiding [20, 21]. A more elaborate description of the circuits which are thought to be involved in the storage and voiding phases may be found elsewhere [21] but the presented information should be enough to understand what follows in the thesis. Based on the aforementioned description of the reflexes involved, it may be concluded that four types of neurons are involved in the neural control of the LUT functions: the primary afferent neurons, spinal efferent neurons, spinal interneurons and neurons in the brain. These neurons activate or modulate the reflexes.

As it will become clear later in this chapter, pudendal afferents are of particular interest in the design of the target solution in this thesis. It is speculated that the converging pathways of the pudendal afferents with vesical afferents may contribute to the modulatory input of the former into the reflexes [27]. It was further mentioned that they may play a role in both voiding and storage phases.

Having discussed the neuro-physiology of the LUT, the consequences of SCI are discussed later in this chapter. Before that, some key terms regarding SCI are presented in the subsequent section.

2.4 SCI

The spinal cord is the major pathway through which efferent and afferent command and information travel between the brain and the body. As it was mentioned, the spinal cord contains longitudinally oriented spinal tracts (white matter) surrounding its central areas (grey matter) where the majority of the spinal nerve cell bodies are located. The grey matter is organised into segments that comprise sensory and motor neurons. It was further mentioned that every segment of the spinal cord is generally in charge of controlling a specific part of the body and functionality. Thus, a damage to a specific segment of the spinal cord

may result in the loss of control in the corresponding part of the body. Here, some key terms related to SCI are discussed [28].

Tetraplegia refers to the impairment or loss of motor and/or sensory functions in the cervical segments of the spinal cord due to the damage of the nervous system within the spinal canal.

Paraplegia refers to the impairment or loss of motor and/or sensory functions in the thoracic, lumbar or sacral but not cervical segments of the spinal cord. Neurological level of any injury refers to the most caudal segment of the spinal cord with normal sensory and anti-gravity motor function on both sides of the body provided that there is an intact sensory and motor function rostrally.

An incomplete injury refers to the situation in which there is a preservation of some sensory and/or motor function below the neurological damage level that includes the lowest sacral segments (S4-S5). In contract, a complete injury refers to the situation when there is an absence of any sensory and motor function below the lesion.

2.5 LUT after SCI

Given the intricate neural circuits involved and the switching-like somatic control of the LUT functions as described above, it comes as no surprise that after SCI both functions of the LUT may be significantly disrupted [5]. Depending on the location of the lesion and its completeness the degree of LUT dysfunctions and their nature may vary. For instance, the lesion may merely interrupt the input from higher centres in the brain such as PMC. On the other hand, the lesion may damage thoraco-lumbar circuits. The management of LUT dysfunctions following SCI is challenging as the dysfunction may change during the course of the injury [5]. LUT dysfunctions substantially decrease the QoL for those affected.

The major conditions appearing after SCI and as addressed by the target solution presented in this thesis include the NDO and DSD. The NDO involves the

existence of bladder contractions at low volumes and the DSD is the condition in which the reciprocal activities of the bladder and the outlet are not maintained, hence bladder contractions are mirrored with contractions in the urethra. These conditions may have severe consequences as discussed in Chapter 1 [29].

After SCI above a lumbo-sacral level, understandably, the input from higher orders in the brain and consequently the voluntary control of the LUT may be disrupted. This may result in an areflexic detrusor and urinary retention [5]. However, after a period of time, new sacral spinal reflexes develop. It is thought that these reflexes are mediated by C fibres which are generally thought to be mechanically silent in healthy individuals as mentioned [5]. These fibres are thought to become sensitive to low volume bladder activities. Thus, contractions occur during the filling phase of the bladder [20, 21]. When C fibres become mechanosensitive, the cells in the dorsal root ganglion become enlarged and show an increased electrical activity [5].

The disruption of the spinobulbospinal reflex, namely the input from the PMC, consequently may disrupt the micturition reflex. Any lesion between the sacral segment of the spinal cord and pons may result in an uncoordinated voiding and DSD. Indeed it has been shown that the DSD is correlated with the completeness but not the level of SCI [5].

Weld and Dmochowski showed that 95% of patients with suprasacral injury demonstrated NDO and/or DSD (n=196) [30]. Thus, it shows that such conditions are very widespread following a suprasacral lesion.

2.6 Existing solutions

The focus of this section is on the existing solutions for the NDO and DSD. Generally, these solutions may be divided as pharmaceutical, mechanical and surgical. Mechanical devices may be subdivided into passive and active devices. The latter are primarily the kind of devices used for the neuro-muscular stimulation. After

a brief overview on all types of solutions, in this section the active devices are elaborated on.

Pharmaceutical and surgical

In the case of the NDO, typically, the first devised treatment involves anticholinergic drugs [3]. Considering the nature of the neural signalling involved, it should be clear why that is the case. The high doses of prescribed anticholinergic drugs may lead to troublesome side effects including dry mouth, blurred vision, constipation and cognitive impairment [5, 29]. If such drugs do not yield the desired response, the botulinum toxin type-A injection into the bladder wall may be implemented as a more intrusive intervention [31]. The same toxin may be used for the people suffering from the DSD for a chemical defferentation [3]. Also, muscle relaxant $\alpha-$blockers may be used to relax the outlet [3].

More intrusive solutions include surgical operations. Some implantable stimulators rely upon surgical operations and will be discussed later in this section. the bladder augmentation, an operation in which a section of the intestine is used to increase the bladder volume, can be used to partially suppress the NDO [3]. Further, sphincterotomy may be implemented which is a complex procedure in which urethra is cut into several times to incapacitate it [3, 29]. Both procedures are very intrusive and may result in irreversible side-effects. Having discussed the major pharmaceutical and surgical solutions, the remainder of this section focuses on the use of devices.

Devices

The intermittent catheterisation, developed in the twentieth century, is the predominant solution used in tandem with drugs [3]. Drugs are taken to stop the NDO and catheterisation is used for voiding. Generally, catheterisation is performed four to six times a day [29]. The major issue with catheterisation is that

it is the foremost cause of re-hospitalisation due to infection in the people with SCI [3]. Thus, the quest for an efficacious solution which results only in a limited interruption to patients' lives has never stopped. Devices are intended to reduce symptoms and/or to restore the bladder functions [3]. They may be implemented to restore the functions partially but a device for the recovery of the full bladder function would be highly effective in improving the QoL for those affected. Artificial sphincters, urethral stents and intraurethral pumps are other examples of mechanical devices used which may be used to treat the NDO, DSD and both, respectively [3]. However, the efficacy and the target patient group of such interventions are limited.

The concept of the electrical stimulation was introduced earlier in this chapter. The exact dynamics and analytic models underlying the electrical stimulation will be discussed in detail in Chapter 3. Generally, the stimulus current is injected in an excitable tissue to depolarise it and consequently generate APs. Sensory or motor fibres may be the target of the stimulus current. Stimulating motor fibres may directly induce an activity which is naturally mediated by those fibres. On the other hand, the target of the stimulus current may be sensory fibres. In that case, different effects may be perceived depending on the stimulus and the neural circuits involved. Such a stimulus may modulate the neural activity, in which case the process is referred to as the neuromodulation. In both cases, intact segments of neural circuits are harnessed to achieve a desired response [1]. The duration and frequency of the stimulus result in different firing patterns, thus, different responses may be perceived. Therefore, the design parameters in broad terms constitute the site and characteristics of the stimulus. It may also be possible to hyperpolarise a segment of the nerve and block the generation and propagation of the AP if needs be.

The stimulus current may target the excitable tissue of the bladder directly in

[1] Throughout the thesis, where the act of delivering the stimulus current to excite the neural tissue is intended, the process is referred to as *stimulation* regardless of the end response.

the form of an intravesical stimulation or bladder wall stimulation to facilitate voiding [3]. Such solutions may be used in patients with damaged lower motor neurons in which cases the neural stimulation is not possible. A limited wealth of literature exists on the use of such methods on SCI patients [3,29]. The stimulus current may be applied on the peripheral sites. Namely, the tibial nerve stimulation to suppress the NDO and the pelvic nerve stimulation to facilitate voiding are the examples of such attempts [3,29]. The limited efficacy in the former and distributed nature of the nerve in the latter has resulted in their sparse and generally research based implementations [3].

The stimulation may be applied centrally. The Finetech-Brindley system (Finetech Medical Ltd., Welwyn Garden City, UK) [32] is an example of such attempts to induce voiding by the sacral anterior root stimulation. Efferent fibres, supplying both the detrusor and urethra, are stimulated by implanting electrodes intradurally or extradurally [3], resulting in the contraction of both. However, when the stimulus is removed the urethra relaxes much faster that the detrusor and this results in voiding. Obviously, the voiding paradigm is non-physiological but yields high voiding efficiencies. For the solution to be effective, posterior rhizotomy has been performed in subjects to increase the bladder capacity and compliance by suppressing hyperreflexive contractions of the bladder. Unfortunately, this irreversibly eliminates the reflex erection, reflex micturition and any remaining pelvic sensation [3]. The limited use and the downfall of the solution has been attributed to this last limiting factor.

To treat hyperreflexive contractions of the bladder, Interstim system (Medtronic, MN, USA) [33] for the sacral nerve neuromodulation has been implemented by delivering a low frequency and low amplitude stimulus via a quadripolar electrode, usually placed near the S3 spinal nerve [3]. The effect has been attributed to the inhibitory modulatory effect of somatic afferents on motor fibres to the bladder. The use of this system in SCI has produced mixed results depending on the completeness of the lesion [3]. The discussion presented up to this point

demonstrates the potential benefits an efficacious and conservative solution can have for the patients. A more comprehensive review of the existing solutions can be found in [3] and [29].

The pudendal nerve stimulation has also been proposed for treating a variety of LUT dysfunctions after SCI. The next section will investigate the neurophysiology of the pudendal nerve followed by a comprehensive review of the literature on the pudendal nerve stimulation.

2.7 Pudendal nerve stimulation

The general role of the pudendal nerve in the somatic control of the LUT function was discussed earlier in this chapter. Its efferent and afferent pathways innervate various pelvic structures including the EAS, external urethral sphincter, genitalia and urethra [34]. The origin of the pudendal nerve is related to the sacral plexus which is composed of the anterior rami of L4 and L5 and sacral nerves of S1, S2, S3 and S4. Subsequently, from this plexus, the pudendal nerve is formed from the anterior rami of S2, S3 and S4 sacral nerves [35, 36]. The nerve is paired and its lateral branches originate from the either side of the sacrum. Through the lower part of the left and right sciatic foramen, the nerve branches enter the gluteal region. Turning around the sacrospinous ligament near its attachment to the ischial spine, the pudendal nerve re-enters the perineum via the lesser sciatic foramen [35]. Running across the distal edge of the ischo-anal fossa, the nerve gives rise to its terminal branches in an area referred to as the Alcock's canal. These terminal branches generally constitute the inferior rectal branch (IRN), which is generally the first terminal branch, the dorsal genital nerve (DGN) and perineal nerves (PerN) [34]. This is the general view of the course and branching pattern of the pudendal nerve. However, the branching pattern and the course of the nerve have been shown to be highly variable across different individuals [35]. The latter has been quantified in ultrasound and cadaveric studies at the point

the compound nerve re-enters the perineum with respect to its distance from the ischial spine [37, 38]. Therefore, if the nerve is not accessed directly, such variabilities should be taken into account.

The pudendal nerve stimulation at various positions along its course and different terminal branches, using various stimulation parameters, has been the topic of research by many workers. Some of the key contributions are shown in Table 2.2 in which it is demonstrated that the pudendal nerve stimulation has been studied for the recovery of both functions of the LUT. The major conclusion of the presented information is that depending on the position and frequency of the stimulus current pulses, voiding or inhibition effects may be achieved in the pudendal nerve stimulation. Also, the pattern of the stimulus pulses may induce different responses as shown below. These may be attributed to the studies that indicate pudendal afferents are involved in both voiding and storage responses. In the voiding phase, the passage of urine through the urethra may trigger a voiding reflex via pudendal afferents while during the storage phase, the guarding activity of the external urethral sphincter may trigger a storage reflex via these afferents. Understandably, the afferent activities in these two cases may be different. Thus, one may hypothesise that this is the cause of yielding different responses when applying different stimulus pulses of different characteristics.

Table 2.2: A review of studies on the pudendal nerve stimulation.

Ref.	Year	Subject	Function	Branch	Frequency (Hz)	Duration (μs)	Notes
[7]	1986	human	inhibit	DGN	1	200-500	[2]
[39]	1987	human	inhibit	compound	1-5	200	[3]
[40]	1996	human	inhibit	DGN	5	500	[4]

Continued on next page

[2] In a study on recent SCI patients, bipolar surface electrodes were used to stimulate the DGN. 200-500 μs pulses repeated at 1 Hz were applied. The detrusor contraction was completely abolished or the threshold of the contraction was significantly increased.

[3] Using needle electrodes inserted in the vicinity of the ischial spine, 200 μs pulses repeated at 1-5 Hz were applied. At relatively low stimulus amplitudes the hyperreflexive contractions of the bladder were inhibited across all subjects.

[4] In a study on 20 chronic SCI patients, bipolar surface electrodes were used to deliver 500 μs pulses repeated at 5 Hz. It was demonstrated that a current twice the bulbocavernosus threshold resulted in a significant increase in the bladder capacity.

Ref.	Year	Subject	Function	Branch	Frequency (Hz)	Duration (μs)	Notes
[41]	1998	cat	void	urethral	10-50 (burst)	200	[5]
[42]	1998	human	inhibit	DGN	5	500	[6]
[43]	2001	human	inhibit	DGN	15	200	[7]
[44]	2002	human	inhibit	DGN	25	250	[8]
[45]	2005	cat	void	PerN	2-40	100	[9]
[46]	2005	human	inhibit	compound	1	-	[10]
[47]	2005	human	inhibit	compound	5 & 15	210	[11]
[48]	2006	cat	both	compound	2-100	100	[12]

Continued on next page

[5]The electrical stimulation of the urethral sensory pudendal nerve in decerebrate and spinal cats were compared. While in decerebrate animals the stimulation evoked voiding, in acute spinal subjects the results were less conclusive. Bursts of 200 μs pulses at 300 Hz were repeated at frequencies ranging from 10 Hz to 50 Hz.

[6]The therapeutic effect of the DGN stimulation using surface electrodes and 500 μs pulses repeated at 5 Hz with amplitudes as high as 99 mA was tested in SCI patients. No lasting effect was observed.

[7]A continuous and conditional stimulation of the DGN using 200 μs pulses repeated at 15 Hz, was applied using silver-silver chloride self-adhesive surface electrodes in SCI patients. The current was varied between 20-60 mA. Considering the detrusor pressure as the control signal, both of the conditional and continuous stimulations increased the bladder capacity. The conditional stimulation yielded a higher mean bladder capacity in the majority of cases.

[8]Biphasic 250 μs pulses repeated at 25 Hz were applied using bipolar surface electrodes, 1-cm in diameter, on the penis with a 2 cm inter-electrode spacing. The stimulation inhibited hyperreflexive contractions of the bladder and decreased the increased blood pressure in dysreflexia.

[9]This study investigated the underlying spinal micturition reflex circuits and the effect of the bladder volume in eliciting such reflexes related to the PerN branch of the pudendal nerve and its firing rate. Platinum bipolar hook electrodes were used to stimulate the PerN with cathodic pulses repeated at 2-40 Hz. Confirming a spinal micturition reflex dependent on the input from PerN afferents, it was shown that the reflex depends on the bladder volume in spinal cord transected cats. 20-40 Hz pulse repetition frequencies showed more sustained results.

[10]Subjects suffered from the urgency, frequency or retention. The efficacy of the sacral nerve stimulation was compared with that of the pudendal nerve stimulation using the Medtronic InterStim system. Tined leads were placed in S3 nerve root and the pudendal nerve. In this limited study, the pudendal nerve stimulation was proven to be superior.

[11]Subjects with the NDO were selected. Tined leads were placed near the ischial spine in the Alcock's canal and the stimulation was delivered using a Medtronic stimulator. Predominantly 5 Hz and in some cases 15 Hz, 210 μs pulses, were applied. Preliminary results show the possibility of achieving continence. The major contribution of this study, however, was the surgical method proposed.

[12]This study primarily investigated the frequency dependent stimulation of the compound pudendal nerve. Platinum bipolar hook electrodes were used to deliver cathodic stimulus pulses of varying amplitudes repeated at frequencies ranging from 2-100 Hz. Continence like responses were observed at low frequencies (10 Hz) while micturition like responses were observed at mid-frequencies (33 Hz). It was suggested that this may be due to a selective activation of different afferents in the compound pudendal nerve. Namely, it was suggested that a low frequency stimulation may activate the rectal or DGN afferents while mid-rage frequencies may only activate DGN afferents. For micturition like responses the bladder volume played a significant role. Also, the stimulus at mid-frequencies should have been applied long enough before the desired response was observed.

Ref.	Year	Subject	Function	Branch	Frequency (Hz)	Duration (μs)	Notes
[49]	2006	cat	void	compound	33	100	[13]
[50]	2006	cat	both	compound	0.5-1K	100	[14]
[51]	2007	cat	void	compound	20 & 10K	200 & 50	[15]
[52]	2007	human	void	compound	1-30	100	[16]
[53]	2007	cat	void	various	1-100	100	[17]
[54]	2008	cat	void	compound	0.1-50	various	[18]
[55]	2008	cat	void	various	2-50	100	[19]
[56]	2008	rat	void	sensory	1-50	100	[20]
[57]	2008	cat	both	DGN	1-40	100	[21]

Continued on next page

[13]Platinum bipolar hook electrodes were used to deliver cathodic stimulus pulses of varying amplitudes to the compound pudendal nerve. Continuous trains or intermittent trains composed of 1 s bursts at 33 Hz separated by 0.2-0.3 s pauses in stimulation were applied. Micturition-like responses were observed. The subsequent study by Boggs *et al.* investigated the frequency dependence in more detail.

[14]The pudendal nerves of four female cats were stimulated using stainless steel bipolar hook electrodes while the nerve was accessed posteriorly. 100 μs pulses were repeated at frequencies ranging between 0.5 Hz to 1000 Hz. While the inhibitory effect generally peaked at 3 Hz stimulus pulses, the pudendal nerve stimulation at 20 Hz showed an excitatory effect. The excitatory effect was dependent on the volume of the bladder.

[15]Two platinum tripolar cuff electrodes in quasi-tripolar setting were placed around the pudendal nerve in chronic SCI cats. One was used to deliver 20 Hz stimulus while the other was used to apply a train of high frequency biphasic continuous charge balanced rectangular pulses at 10 kHz. The blocking effect of high frequency stimulus showed a considerable increase in voiding efficiency.

[16]In a study on two chronic SCI patients a needle electrode was inserted percutaneously in the vicinity of the pudendal nerve. While 100 μs pulses at different amplitudes and frequencies were applied. While low frequencies did not necessarily generate inhibition, high frequencies ($>$ 20 Hz) showed an excitatory response. It should be noted that the number of subjects was very limited. Furthermore, the exact placement of the electrode may not be very clear.

[17]Using needle electrodes inserted in different positions in the sacroiliac position, the possibility of generating a sustained bladder contraction was investigated for different pulse frequencies and amplitudes. The variability of responses demonstrated the possibility of investigating reflexes mediated by the pudendal afferents in human using similar methods.

[18]Building on the idea that bursting naturally occurs to code the sensory information conveyed by afferents, bursts of stimulus pulses repeated at frequencies ranging from 0.1-50 Hz of biphasic stimuli were applied in 8 subjects. It was found that variably patterned pulse bursting results in a greater evoked reflex bladder pressures.

[19]Platinum cuff electrodes were used to stimulate different branches of the pudendal nerve at different frequencies before and after spinal transection. The study presented evidence that two distinct micturition pathways are present. This is due to the fact that while certain frequency dependent responses are abolished upon spinal transection, the rest remain intact.

[20]In a study on rats, 100 μs pulses repeated at frequencies ranging from 1-50 Hz were delivered to the transected sensory nerve of the rat using cuff electrodes. Low intensity stimulations demonstrated an improvement in the voiding efficiency.

[21]The DGN was stimulated using cuff electrodes or percutaneously using wire electrodes. 20 s and 30 s long trains of 100 μs pulses at frequencies ranging from 1-40 Hz were applied. It was demonstrated that while at low frequencies (5-10 Hz) contraction of the bladder was inhibited, at higher frequencies (30-40 Hz) detrusor contractions and micturition-like reflexes were elicited.

Ref.	Year	Subject	Function	Branch	Frequency (Hz)	Duration (μs)	Notes
[58]	2009	cat	both	urethral	2-33	100	[22]
[59]	2010	human	inhibit	DGN	10 & 15	200	[23]
[60]	2010	human	void	urethral	10-40	200	[24]
[61]	2011	cat	both	compound	5-40	1000 (burst)	[25]
[62]	2011	human	both	urethral	2-35	200	[26]
[63]	2011	rat	void	sensory	1-50	100	[27]
[64]	2011	human	void	urethral	20	200	[28]
[65]	2012	cat	inhibit	various	1-30	100	[29]
[66]	2013	cat	both	compound	various	various	[30]

Continued on next page

[22]Using the intra-urethral stimulation of the pudendal nerve, it was demonstrated that the resulting reflexes are very much dependent on the placement of the electrodes and the stimulus frequency. This dependence was attributed to the distinct pudendal afferent pathways activated based on these parameters.

[23]In a study on neurologically stable complete or incomplete chronic SCI patients suffering from the NDO, the effect of the conditional DGN stimulation was investigated. The control signal was the EMG signal recorded from the EAS. Surface electrodes were used to apply biphasic 200 μs pulses repeated at 10 or 15 Hz. The conditional stimulation was shown to yield a high bladder capacity similar to the unconditional stimulation but the stimulation time could substantially be reduced. Further, the use of the said control signal to detect the onset of the hyperreflexive contraction of the bladder was verified.

[24]In a study on a SCI woman the urethra was stimulated over a range of bladder volumes. 200 μs pulses repeated at frequencies varied from 10 to 40 Hz were used. At 20 Hz stimulus pulse repetition frequency, sustained contractions were observed.

[25]In an attempt to demonstrate the feasibility of the transcutaneous pudendal nerve stimulation, amplitude modulated high frequency sinusoid stimulus (210 kHz) was applied for pulses of 1 ms duration repeated at a frequency ranging from 5 Hz to 40 Hz. At low frequencies (<20 Hz) an inhibitory effect was observed while at higher frequencies (20 - 30 Hz) excitatory effects were seen above certain bladder volumes.

[26]Using different intraurethral electrode placements and different stimulus pulse repetition frequencies the existence of two independent excitatory pudendal to bladder reflex pathways were demonstrated in chronic SCI patients.

[27]Using bipolar cuff electrodes, the transected sensory branches of the pudendal nerve were stimulated. 100 μs stimulus pulses repeated at frequencies ranging between 1 Hz to 50 Hz were applied either unilaterally or bilaterally.

[28]In a study on two chronic SCI male subjects the intraurethral stimulation was conveyed . 200 μs pulses repeated at 20 Hz yielded a volume dependent contraction and bladder emptying in both cases.

[29]In a study on male cats, it was demonstrated that the inhibition of bladder contractions was significantly dependent on the stimulation location, frequency and amplitude. The compound pudendal nerve and DGN were stimulated by a 30 s train of 100 μs pulses repeated at frequencies of up to 30 Hz using nerve cuff electrodes. The range of parameters that caused inhibition was larger in the case of the DGN stimulation.

[30]Tripolar cuff and bipolar electrodes along with the wireless electronics were implanted to deliver the pudendal nerve stimulation and block. The high frequency (5-20 kHz) biphasic stimulation through the tripolar electrodes and 1-100 Hz low frequency pulses through the bipolar set were delivered. The efficacy of the high frequency block and the possibility of generating a significant increased bladder capacity at the low stimulus frequency (5 Hz) were demonstrated.

Ref.	Year	Subject	Function	Branch	Frequency (Hz)	Duration (μs)	Notes
[67]	2014	cat	void	compound	33	100	[31]
[68]	2015	cat	void	DGN	33 (patterns)	100	[32]

2.8 Trans-rectal neuromodulation

The target solution presented in this thesis is primarily based on the solution proposed by Craggs *et al.* [8, 69] for a conditional trans-rectal neuromodulation of the pudendal nerve. In a study on 6 SCI patients suffering from the NDO and DSD, using a probe similar to the one shown in Figure 2.8, they showed that by the conditional neuromodulation of the pudendal nerve, hyper-reflexive contractions of the bladder were suppressed. The control signal was set to be the EMG signal from the EAS. Different features of this concept are discussed in more detail here. It was mentioned in Chapter 1 that more conservative solutions are preferred due to their generally less intrusive nature. Furthermore, such solutions generally have none or reversible side-effects which can greatly improve the QoL for patients if they are proven to be efficacious. In addition, more economic solutions are of interest as they can be more readily available for those in need. The trans-rectal neuromodulation of the pudendal nerve may provide a solution which meets all the above-mentioned criteria. Given the course of the pudendal nerve as described earlier, a trans-rectal stimulator whose electrodes are positioned in the vicinity of the ano-rectal junction is likely to expose the compound pudendal nerve to the stimulus current. Considering the contributions in Table 2.2, there may a possibility of invoking voiding or continence via a trans-rectal neuromodulation based on the stimulus frequency. Therefore, a wearable solution

[31] It was demonstrated in a study on cats that the compound stimulation of pudendal afferents would evoke a larger bladder contraction reflex, resulting in a higher voiding efficiency as compared to a single branch stimulation. Cuff electrodes were used to deliver the stimulus to every branch and the optimal stimulus parameters were based on previous studies for each individual branch.

[32] Using computational models and cat subjects, it was established that the pattern of the stimulation as well as its frequency can modulate the response of the bladder and the magnitude of the evoked contraction.

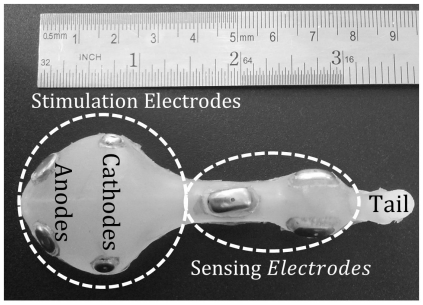

Figure 2.8: The probe developed by Craggs *et al.* [8,69] for the conditional trans-rectal pudendal nerve neuromodulation. Figure adapted from [70].

may be designed for recovering the full bladder function after SCI. The existing reported efficacies may not be quantitatively relevant at the moment but with the advent of other complementary methods and techniques they may be improved. The intra-anal and vaginal stimulations are primarily used for the acute delivery of the stimulus current to pelvic structures, generally muscles, and for therapeutic purposes [71]. In early attempts to stimulate the pudendal nerve, the required current levels were as high as 100 mA to yield a visible response [7]. Craggs *et al.* [8] also reported a similar level of the required stimulus current. The design of such probes are generally heuristic and conjectural. In one of the first attempts by Brindley *et al.* [72] a design of a trans-rectal probe to target the pudendal nerve was proposed. In that contribution, the body of the trans-rectal stimulator and the position of the electrodes were designed in a way that the electrodes were placed at the closest distance possible from where the nerve was thought to be. Similar design paradigms were implemented by Craggs *et al.* [8,69,73]. Although not thorough, such endeavours served as the starting point for the work presented in this thesis. For the chronic use of the trans-rectal stimulation, the probe on which the electrodes should be mounted should be held in place firmly while it does not damage the surrounding anatomical structures. An early contribution by Hopkinson and Lightwood [74] indicated the need for various sizes of the anal probe for the stimulation of the EAS. A more elongated probe, targeting the pudendal nerve further down the anal canal, may benefit from the opening at the

ano-rectal junction and a wider tip may hold the anal probe in place. The study by Craggs *et al.* [8] used a single size probe for all subjects based on the same reasoning.

As shown by Kirkham *et al.* [43] a conditional neuromodulation to suppress the bladder contraction may improve the efficacy of the solution. It was mentioned that the majority of cases of the NDO after SCI are accompanied by the DSD. Thus, any contraction in the bladder is mirrored by contractions in the external urethral sphincter. It was further noted that the same nerve innervates the EAS and external urethral sphincter. Therefore, it is conceivable that the EMG signal recorded from the EAS may be used as a surrogate for that of the external urethral sphincter which demonstrates the onset of the hyper-reflexive contractions of the bladder. Wenzel *et al.* [75, 76] and Horvath *et al.* [59] have shown the feasibility of using the activity of the EAS to detect the onset of the hyperreflexive bladder contractions. Craggs *et al.* [8] have corroborated this as mentioned above.

Therefore, an anal probe can conveniently record the EMG signal from the EAS with electrodes mounted on its tail and stimulate the pudendal nerve using the electrodes mounted on its tip. The study presented by Craggs *et al.* [8] similar to previous studies was only an acute test of their hypothesis. In the long run, the high levels of the stimulus current may result in the habituation of the nerve even under the conditional stimulation. For sensate individuals, such levels of the stimulus current may be beyond the pain threshold and at high levels of the stimulus current the targeting accuracy required may be lost. Any structure in the vicinity may also be stimulated, resulting in unforeseen responses. Also, high levels of the stimulus current increase the possibility of electrode or tissue damage. Therefore, the design of electrodes should be optimised to minimise the stimulus current. Even if the current is minimised, however, the challenge is that the course of the nerve is highly variable between different individuals as discussed earlier in this chapter. It should be investigated if this affects the

efficacy of a device or if a multi-electrode device is needed to vary electrode configuration from one individual to the other. Furthermore, the pelvic structures move depending on the posture of the individual. This adds to the variations of the course of the nerve.

Finally, in case the solution is used to conditionally stimulate the pudendal nerve, the design of the recording electrodes should be carefully analysed to ensure they only record from the EAS. Larger electrodes or those oriented incorrectly may record from any muscular structure in the vicinity; hence, the conditional nature of the neuromodulation can be lost. Thus, the main concern in designing a wearable conditional pudendal nerve neuromodulator is the design of its electrodes in terms of their placement and the overall design for a chronic use. The optimisation of the design of the stimulation and recording electrodes are presented in the subsequent chapters.

2.9 Summary

The purpose of this chapter was to put the fundamentals of the target solution presented in this thesis and the work presented in the subsequent chapters into perspective. Starting from the central and peripheral divisions of the human nervous system, as the most general categorisation, their role and general attributes were introduced. Then, the building-blocks of the nervous system, namely, neurons and glial cells as well as some key terms referred to in this thesis were introduced. The idea of neural circuits, the way sensory fibres convey the information collected from the receptors to the central neurons and, conversely, the way the motor fibres relay the neural signals from the central neurons to the periphery to invoke an effect with neuro-transmitters were introduced. Fundamentals of the AP generation and propagation as the stereotyped neural signal were introduced and the effects of the fibre size on the AP generation and propagation were evaluated using analytic models where possible.

The neuro-physiology of the LUT and its functions were introduced with a particular attention paid to neural circuits and their attributes. Namely, the central and peripheral control, the nerves involved and their presumed roles, the type of fibres and pathways and, finally, the kind of receptors and transmitters involved were discussed.

Introducing the general terms regarding SCI, its possible effects on the LUT functions and probable causes of those effects were discussed with a particular attention paid to the NDO and DSD. After reviewing the major categories of the LUT treatment after SCI, the pudendal nerve neuromodulation was introduced as a promising treatment method. A comprehensive review of the key contributions regarding the pudendal nerve stimulation was presented. The evidence was shown that the compound pudendal nerve stimulation may have a frequency dependent response and it may promote continence and voiding.

The trans-rectal stimulation of the pudendal nerve and previous attempts in the literature to produce a conservative treatment based on that were discussed. It was mentioned that the major issue was the high levels of the stimulus current required. However, any attempt to minimise the stimulus current should consider the variability of the course of the nerve in different individuals and in an individual in different body postures. It was further mentioned that the trans-rectal neuromodulation of the pudendal nerve may be applied conditionally when used to suppress the NDO. It was discussed that the EMG signal recorded from the EAS may be used as the control signal to indicate the onset of the hyper-reflexive contractions of the bladder. However, the recording electrodes should be designed for a chronic and unsupervised use. Thus, the motivation for the subsequent work presented in the thesis was laid out as the optimisation and design of the stimulation and recording electrodes.

Chapter 3

Stimulation Compartment Design

3.1 Introduction

The clinical basis of the electrical stimulation of excitable tissues and the limitations of the existing design of a trans-rectal pudendal nerve neuromodulator were addressed in Chapter 2. The underlying principles of the excitability in terms of the existing models are addressed here. Based on computational models, an optimised design with a minimum number of electrodes is proposed in this chapter. Starting from the HH type cable models of axons, the development of such models is reviewed. The specifics of the volume conductor modelling, the underlying mathematical formulations, approximations, boundary conditions and the numerical techniques are discussed. After reviewing the development of models of the extracellular stimulation, applications of such models and their possible limitations are discussed.

The MRI study performed to approximate the nerve trajectory and other anatomical features with the device *in situ* and an experiment involving a trans-rectal stimulation with a non-optimised design, performed to estimate tissue conductivities are presented. The rest of the chapter presents the computational models and a novel optimisation paradigm implemented to identify an optimised electrode placement for the stimulation electrodes.

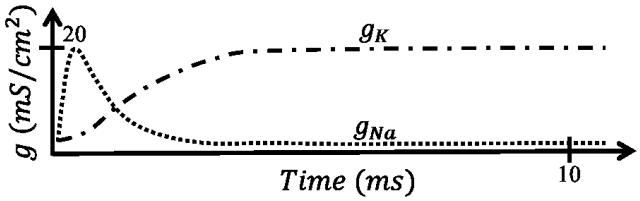

Figure 3.1: A sample conductivity versus time plot in the HH experiment for a relatively high depolarisation voltage. The major observation is that while g_{Na} rises and falls, g_K rises and stays at a fixed level. Re-drawn from [16].

A specific configuration is proposed which yields a relatively low threshold for possible and probable neuroanatomical variations of the target nerve.

3.2 Theoretical review

3.2.1 Nerve fibre modelling

After the development of the voltage-clamp technique [77], it was made possible to set the transmembrane voltage to a predetermined value and measure the transmembrane current for the said voltage in the giant axon of Loligo. HH formed a set of curves of the conductivity of potassium and sodium (g_K and g_{Na}) versus time similar to those shown in Figure 3.1 for various depolarisation voltages [16]. Apart from the overall time trace, they noticed that as the clamp voltage increases, the rate at which the conductance varies increases too. Based on the aforementioned characteristics, they decided to use the first order kinetics to formulate the observation and fit the experimental data. In the first order kinetics, the rate of change of a variable (x) in time (t) is dependent on the value of the variable multiplied by a constant (K) as shown in Equation (3.1):

$$-\frac{\partial x}{\partial t} = Kx. \tag{3.1}$$

They established a formulation for the transmembrane ionic current as shown in Equation (3.2):

$$I_{ion} = \bar{g}_K n^4 (V - V_K) + \bar{g}_{Na} m^3 h (V - V_{Na}) + \bar{g}_l (V - V_l) \tag{3.2}$$

where $\bar{g}_K$, $\bar{g}_{Na}$ and $\bar{g}_l$ are the maximum potassium, sodium and leakage channels' conductances, respectively. V_K, V_{Na} and V_l are the corresponding Nernst voltages. n, m and h are dimensionless variables which can vary between 0 and 1 and are associated with the potassium channel activation, sodium channel activation and sodium channel inactivation variables, respectively. The fact that, for instance, n is raised to a power is only showing the order of the process they could fit the data with. The way HH arrived at this formulation will become clear in the following lines.

A generic formulation can show how n, m and h change as shown in Equation (3.3):

$$\frac{d\omega}{dt} = \alpha_\omega (1 - \omega) - \beta_\omega \omega \tag{3.3}$$

where ω can be m, n or h and α and β are voltage dependent rate constants. Although HH developed a merely empirical formulation for the observations but the overall macroscopic system of equations they defined is compatible with the microscopic understanding which exists today. The description of the formulation presented here is based on the current understanding [10]. There are a large number of microscopic ion channels in the neuron membrane, each of which has some gates which may be open or closed. A channel conducts only if all its gates are open. ω can then be defined as the probability of having a gate open, α as the rate at which the closed gate opens and β the rate at which the open gate closes. Now the physical meaning of Equation (3.3) should be clear. In macroscopic terms, having many channels, the notation changes into having a fraction of the gates open or closed. Thus, $\bar{g}_{ion}\omega$ explicitly indicates the conductivity of a certain channel.

It is trivial to show that the steady-state value of ω (ω_∞) for a given clamp voltage v is given by Equation (3.4):

$$\omega_\infty(v) = \frac{\alpha_\omega(v)}{\alpha_\omega(v) + \beta_\omega(v)}. \tag{3.4}$$

Consequently, the time trace of ω is given by Equation (3.5):

$$\omega(t) = \omega_\infty(V_c) - (\omega_\infty(V_c) - \omega_\infty(0))e^{\frac{-t}{\tau_\omega(V_c)}} \tag{3.5}$$

where V_c is a given clamp voltage and τ_ω is given by Equation (3.6):

$$\tau_\omega(V_c) = \frac{1}{\alpha_\omega(V_c) + \beta_\omega(V_c)}. \tag{3.6}$$

Given the time formulation of ω in Equation 3.5 for each ion, HH raised the process to a power that best fit the experimental measurements. As the sodium channel conductivity has a transient response, a second order process is required to model the trend. HH decided to use two first order processes and account for its inactivation. Understandably, $\alpha_{activation}$ has a similar formulation as $\beta_{inactivation}$ and $\beta_{activation}$ similar to that of $\alpha_{inactivation}$ to generate a transient response.
Thus, the total transmembrane current (I_m, inward positive) is given by Equation (3.7):

$$I_m = c_m \frac{dV_m}{dt} + I_{ion} \tag{3.7}$$

where c_m is the lipid bi-layer capacitance per unit area and V_m is negative for the depolarisation case. Figure 3.2 shows the equivalent model of the HH model. This modelling paradigm constituted the building block of any research that ensued. As mentioned above, the striking feature of the HH model is that its features can have a physical meaning and it is not merely a functional model.
So far, only transmembrane characteristics of a fibre have been discussed. To be able to model an axon, one needs to consider the axial resistance of an axon to

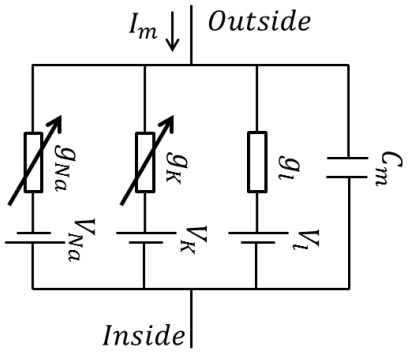

Figure 3.2: The HH model of an axon. Re-drawn from [16].

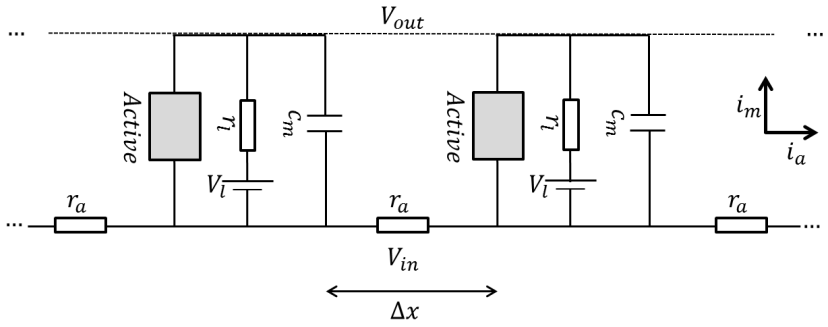

Figure 3.3: Cable model of an axon. Various features such as channel mechanisms, the axial resistance (r_a $[\Omega.m^{-1}]$), the passive membrane channel resistance (r_l $[\Omega.m]$) and the lipid bilayer capacitance (c_m $[F.m^{-1}]$) are incorporated. The active element may be replaced by the HH model or a similar model.

the current flow and model a segment of the fibre. Then, implementing the cable theory [78], it is possible to formulate a complete set of differential equations to model a phenomenon such as the initiation and propagation of APs. A cable model of an axon is shown in Figure 3.3. The purpose of the cable theory is to find a set of partial differential equations in time and space. Assuming that $\Delta x \to 0$, it is trivial to relate the axial current (i_a) and membrane current (i_m) as $\frac{\partial i_a}{\partial x} = -i_m$, in which the variations in i_a along the x axis are governed by the amount of the current *leaking out* (i_m). Also, from Ohm's law, $\frac{\partial V_{in}}{\partial x} = -i_a r_a$ is valid. Therefore, it is possible to formulate an expression for i_m as shown in

Equation (3.8):

$$i_m = -\frac{\partial i_a}{\partial x} = \frac{1}{r_a}\frac{\partial^2 V_{in}}{\partial x^2}. \tag{3.8}$$

This way, an expression for the membrane potential can be formed in time and space as shown in Equation (3.9):

$$\frac{1}{r_a}\frac{\partial^2 V_{in}}{\partial x^2} = I_{Active} + c_m\frac{\partial V_{in}}{\partial t} + \frac{1}{r_l}(V_{in} - V_l). \tag{3.9}$$

This forms the basis of any attempt in modelling the nerve fibre. For I_{Active}, HH channel mechanisms or any other channel mechanism can be substituted and by integrating Equation (3.8), it is possible to find a time trace of the variations of the membrane potential. In the following sections, the development of the HH channel mechanisms into the more elaborate models representing the human fibres are addressed.

Myelinated fibre modelling

In the development of models for myelinated fibres, one may consider two major sets of features in the model. The first set of features comprises the components of the ionic currents involved. In the HH model, one passive mechanism (g_l) and two active mechanisms (g_{Na} and g_K) were defined. As will be discussed, other mechanisms also exist in a mammalian fibre [17].

The second major set of features is the way a model represents the myelination. It is noted that the main purpose of different representations is to accurately model the experimental observations. Although the two sets of features (i.e., the underlying channel mechanisms and the formation of the cable models) are intertwined, they are treated as two separate conceptual elements for the purpose of arranging the review of the literature. The following lines will address the variations of these features as reported in the literature.

Three general models of myelinated fibres can be found in the literature and they mainly differ in their assumption regarding the internodal segments. The

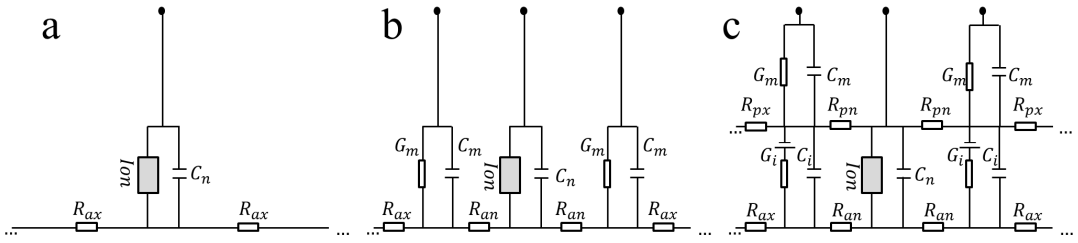

Figure 3.4: Three different cable models of myelinated axons. (a) assumes a perfect insulation for the myelin sheath, while (b) and (c) assume an imperfect insulation. (c) is superior as it considers more realistic features of the fibre. Redrawn with changes from [79].

first approach considers myelin as a perfect insulator as shown in Figure 3.4a. Notable early contributions using this approach were those of McNeal [80] and Sweeney [81]. Other studies [82, 83], including the more recent ones [84, 85] have also implemented such models. However, it has been demonstrated that the myelin is not a perfect insulator and has capacitance as well [86, 87].

The second approach in modelling the myelinated fibre is to account for the passive mechanism in parallel with the membrane capacitance to indicate the capacitive and passive current flows through the myelin sheath. One of the first contributions of this approach was that of Fitzhugh [88] based on the HH model. Goldman and Albus used the same approach to investigate the velocity-diameter relation [89]. Moore *et al.* used a similar approach with a variation of the channel mechanism [90] and Rubinstein used such representations of the myelin sheath in an analytical study of the extracellular stimulation while using the parameters of cats' auditory nerve [91]. A recent study on the spinal cord stimulation also used the same representation [92].

One of the first instances of suggesting a double layer cable model, as shown in Figure 3.4c, was by Barrett and Barrett who indicated the need for such representations in which they attributed the depolarising after-potential (DAP) to the slow capacitive discharge [93]. Blight and Someya also corroborated such results [94] and Blight further analysed the component values of such models [95]. Other key developmental models of this kind are those of Halter and Clark [96],

Bostack *et al.* [97], Awiszus [98] and that of Stephanova and Bostock [99] although in the majority of these contributions the mechanisms they proposed are not widely used in recent contributions.

Perhaps two of the most important contributions of their kind were those of Richardson *et al.* [79] and McIntyre *et al.* [17], from which various contributions ensued. Richardson *et al.* investigated the suitability of implementing these three models and McIntyre *et al.* formalised a set of equations and specifications for mammalian fibres of various diameters by replicating experimental data. The model proposed by McIntyre *et al.* is referred to as the **MRG** model hereafter.

So far, the physical form of the model and the ability of the double layer cable model to replicate the experimental data (e.g., DAP) were mentioned. However, the underlying channel mechanisms were only briefly touched upon. The following lines focus on the studies regarding channel mechanisms.

After the HH study on a squid axon (1952) [16], Frankenhaeuser and Huxley derived the model parameter values for frogs' axon (1964) [100], Chiu *et al.* did similar studies on rabbits (1979) [101], followed by Brismar's work on rats (1980) [102] and, finally, Scholz *et al.* (1993) [103], Schwarz *et al.* (1995) [104] and Reid *et al.* (1999) [105] studied on the human fibre. This shows the trend of studies which was generally a function of the methods and apparatus available.

A complete literature review on the research aimed at ascertaining the exact mechanisms involved in the human myelinated axon is beyond the scope of this thesis. The goal is to demonstrate the validity of the model used in this chapter. Thus, pertinent contributions are cited. The efforts which culminated in the formalisation of the MRG model were generally focused on replicating different components of the recovery cycle in an AP. This is particularly important as it explores the excitability of a fibre after an episode of the AP generation. As mentioned before, an AP lasts no more than 1 ms at physiological temperatures in mammalian axons. However, its reverberations last considerably longer and affect the axon's excitability for tens of milliseconds. After the absolute and

relative refractory periods, mainly due to the inactivation of fast sodium channels [17, 101], periods of increased excitability (DAP) and reduced excitability (Afterhyperpolarisation (AHP)) follow. The former is referred to as supernormal and the latter as subnormal periods [93, 94]. The DAP has been associated with the discharge of the internodal axolemma, having been charged during the AP [93]. Persistent Na channels are also attributed to DAP events [17, 106], while slow K channels are generally associated with the AHP [17, 106]. Given the passive elements involved, a double layer cable model as shown in Figure 3.4c should be used to follow the aforementioned phenomena. McIntyre *et al.* [17] used a double cable model in which between every subsequent node of Ranvier, two myelin attachment segments (MYSA), two paranode main segments (FLUT), and six internode segments (STIN) were placed. In each node of Ranvier, they devised a persistent Na channel (Na_p, only activation), a fast Na channel (Na_f, activation and inactivation), a slow potassium channel (K_s, only activation), a linear leakage (L_k) and a nodal capacitance (C_n). For all the internodal segments, the axolemma was represented by an internodal capacitance (C_i) in parallel with a linear leakage channel (G_i) and the myelin sheath was represented as a parallel combination of its capacitance (C_m) and conductance (G_m). Furthermore, the appropriate axial resistances between sections in both layers were implemented (R_{an}, R_{pn}, R_{ax} and R_{px}). They derived the channel dynamics from studies on the human axon and other membrane dynamics including the geometrical parameters from studies on the human, cat and rat for fibre diameters ranging from 5.7 μm to 16 μm. McIntyre *et al.* were able to replicate a range of observations by adjusting the parameters of their model including verifying their hypothesis regarding the DAP and AHP.

Various contributions have used the MRG model and the model has been able to predict a wide variety of neural events. In a comparative study [107] by Kuhn *et al.*, models in [80, 81] were compared with the MRG model in the transcutaneous current stimulation and the results of the MRG-based model matched the exper-

imental data best.

It should also be noted that although the model was originally developed for motoneurons, it has been shown that it is capable of modelling the afferent response as well [108]. Furthermore, an early work has demonstrated that for an stimulus current lasting less than and about 200 μs the responses of afferents and efferents are alike [109].

Numerical solution

To understand the numerical techniques involved, the cable equation is revisited for a dual compartment model as shown in Equation (3.10).

$$C_m \frac{\partial V}{\partial t} + gV = \frac{a}{2\rho_a} \frac{\partial^2 V}{\partial x^2} \tag{3.10}$$

where C_m is the specific conductivity $[F.m^{-2}]$, g is the specific membrane conductance, a is the fibre diameter $[cm]$ and ρ_a is the axial resistivity $[\Omega.cm]$. Then, boundary conditions should be applied. One of the less intrusive boundary conditions is to set the current density to zero at both ends, implying that the spatial derivative of V should be zero there. If V is considered as a separable function of time and space, $V(t,x) = V_t V_x$, $cos(\frac{2\pi f_x x}{L})$ can fulfil the above-mentioned boundary condition for a cable of L cm long, where f_x is the spatial frequency. This is particularly interesting as then a set of such functions can produce any spatial formation of the voltage as suggested by the Fourier series. Based on Equation (3.10), V_t has a time constant given by $\tau = \frac{g}{C_m} + \frac{2\pi^2 f_x^2 a}{R_a L^2 C_m}$ [110]. This shows that high spatial frequency components decay quickly in time. Clearly, the problem can be discretised in space and time. Then a method of integration, to solve the problem, should be implemented. A complete analysis of different methods and techniques is given in [110].

3.2.2 Volume conductor modelling

Modified Helmholtz formulation

A volume conductor model, is the model of the medium in which Maxwell's equations as shown in Equations (3.11 - 3.14) are solved. A valid model is based on correct assumptions and is the one in which appropriate boundary conditions are set.

$$\nabla.\mathbf{D} = \rho \tag{3.11}$$

$$\nabla.\mathbf{B} = 0 \tag{3.12}$$

$$\nabla \times \mathbf{E} = -\frac{\partial \mathbf{B}}{\partial t} \tag{3.13}$$

$$\nabla \times \mathbf{H} = \sigma\mathbf{E} + \frac{\partial \mathbf{D}}{\partial t} \tag{3.14}$$

where $\mathbf{E}$ is the electric field and is related to $\mathbf{D}$ based on $\mathbf{D} = \epsilon\mathbf{E}$, where ϵ is the permittivity of the medium. $\mathbf{H}$ is the magnetic field and is related to $\mathbf{B}$ based on $\mathbf{B} = \mu\mathbf{H}$, where μ is the permeability. ρ is the charge density and σ is the conductivity of the medium. Using the notation $\frac{\partial}{\partial t} = j\omega$, $\mathbf{E}$ is related to the scalar electric potential field, V, and magnetic vector potential $\mathbf{A}$, which is defined so that $\mathbf{B} = \nabla \times \mathbf{A}$ as shown in Equation (3.15):

$$\mathbf{E} = -j\omega\mathbf{A} - \nabla V. \tag{3.15}$$

Considering the *Lorentz condition*, in which $\nabla.\mathbf{A} = -j\omega\epsilon\mu V$, and $\nabla.\mathbf{J} = -j\omega\rho$, where $\mathbf{J}$ is the current density, and considering Equation (3.11), it is possible to derive a modified *Helmholtz equation* with a non-zero right-hand-side for the wave propagation for a loss-less medium as shown in (3.16):

$$\begin{aligned} \nabla.\mathbf{E} &= -\omega^2\mu\epsilon V - \nabla^2 V = \frac{\rho}{\epsilon} \\ \Rightarrow \nabla^2 V + \omega^2\mu\epsilon V &= \frac{\nabla.\mathbf{J}}{j\omega\epsilon}. \end{aligned} \tag{3.16}$$

For a lossy material with modified dielectric properties, $\epsilon_c = \epsilon - j\frac{\sigma}{\omega}$, (3.16) is modified as shown in (3.17) [111]:

$$\begin{aligned} \nabla^2 V + \omega^2 \mu \epsilon_c V &= \frac{\nabla . \mathbf{J}}{j\omega\epsilon_c} \\ \Rightarrow \nabla^2 V - (j\omega\mu\sigma - \omega^2\mu\epsilon)V &= \frac{\nabla . \mathbf{J}}{\sigma + j\omega\epsilon}. \end{aligned} \tag{3.17}$$

This formulation and its simplifications can be used to model any propagation of electromagnetic fields and is central in understanding what effects are ignored upon simplifications. In the context of electric fields, the impedance of the tissue, whose imaginary component is governed by its permittivity (ϵ_c), induces frequency and time development departures from the static scenarios. Considering the value of the permittivity as $\omega \to 0$ (ϵ_s), its value as $\omega \to \infty$ (ϵ_∞), the magnitude of its dispersion $\Delta\epsilon = \epsilon_s - \epsilon_\infty$ and τ as the relaxation time constant, ϵ_c was traditionally shown as in Debye's Equation (3.18):

$$\epsilon_c = \epsilon_\infty + \frac{\Delta\epsilon}{1 + j\omega\tau}. \tag{3.18}$$

In the presence of N frequency dispersions, ϵ_c is shown as in Equation (3.19) [112]:

$$\epsilon_c = \epsilon_\infty + \frac{\sigma_i}{j\omega\epsilon_o} + \sum_{n=1}^{N} \frac{\Delta\epsilon_n}{1 + (j\omega\tau_n)^{(1-\alpha_n)}}. \tag{3.19}$$

where σ_i is the static ionic conductivity and ϵ_o is the permittivity of the free space.

Poisson's formulation

Based on Ohm's law Equation (3.20) holds.

$$\mathbf{J} = \sigma\mathbf{E} = -\sigma\nabla V. \tag{3.20}$$

To be able to establish *Poisson's formulation*, a variable as source density I_v is introduced for which Equation (3.21) holds.

$$\nabla.\mathbf{J} = I_v. \tag{3.21}$$

Noting that by definition $\nabla.\Phi = \lim_{V\to 0} \frac{\oint_S \Phi.dS}{V}$, I_v is a current per volume parameter. Thus, it is possible to show *Poisson's formulation* as shown in Equation (3.22).

$$\nabla^2 V = -\frac{I_v}{\sigma}. \tag{3.22}$$

This essentially shows a specific case of (3.17) in which all the time variations are set to zero. This is accurate if $\mathbf{E}$ behaves like a static field at each instant in time. In other words, the rate at which the field travels in the medium should be considerably larger than the rate at which the source of the field varies. Under such conditions, the system is linear and temporal developments can be achieved by linearly scaling the results of the field at a given time. Such a case is referred to as the *quasi-static* assumption of the fields.

Under *quasi-static* conditions, V at (x', y', z') is given by Equation (3.23) [113].

$$V(x', y', z') = \frac{1}{4\pi\sigma} \iiint \frac{I_v dv}{r} \equiv \iiint \frac{I_v(x, y, z)}{r(x, y, z, x', y', z')} dzdydz. \tag{3.23}$$

If there is no source in the medium under discussion, then *Poisson's Equation* is simplified to *Laplace's equation* as shown in Equation (3.24).

$$\nabla.\sigma\nabla V = 0. \tag{3.24}$$

Although implemented by numerous past and recent contributions, it should be noted that the *quasi-static* condition is indeed an approximation. In a study Bossetti *et al.* [111] investigated the validity of the assumption and its relative error with respect to that of (3.17). They found that while the exact solution

deviates at a maximum value of 13%, when used to predict thresholds of the model of an excitable tissue, they observed a maximum of 16% error. They observed the majority of the error in the capacitive tissue, yet concluded that the approximation is valid for the relevant conductivities.

Choice of boundary conditions

One of the most important features of modelling is the boundary conditions set. There are boundary conditions which should be assigned to ensure the convergence of the numerical solutions or there are those that should be enforced to impose a specific physical behaviour of an entity within the model.

A first type boundary condition is the Dirichlet boundary condition in which the value of the variable, voltage in this case, is assigned to a boundary of the model. This may be zero at infinity (the most external boundary ($\delta\Omega$)) as shown in Equation (3.25).

$$V(\delta\Omega) = 0. \tag{3.25}$$

A second type boundary condition is the Neumann boundary condition in which the derivative of the variable is assigned a value at a boundary. This may be assigning the role of insulation to a boundary as shown in Equation (3.26).

$$\sigma \nabla V.\mathbf{n} = 0 \tag{3.26}$$

where $\mathbf{n}$ is the normal vector to the boundary and σ is the respective conductivity. An important consideration in building an inhomogeneous model is to assign the transition of the variable at the boundary of different media. Such a boundary condition is shown for the continuity of the normal component of the electric potential field at the boundaries as shown in (3.27) [84] in which the subscripts indicate the variables in the corresponding media.

$$\sigma_1 \frac{\partial V_1}{\partial \mathbf{n}} = \sigma_2 \frac{\partial V_2}{\partial \mathbf{n}}. \tag{3.27}$$

Robin boundary condition

The electrode tissue impedance effects as discussed in Chapter 4 may be incorporated in a model by applying *Robin boundary condition* [114] which is similar to a second type boundary condition with some modifications. This is shown in Equation (3.28)

$$\sigma \nabla . \mathbf{n} = g(V_o - V) \tag{3.28}$$

where σ is the conductivity of the domain, $\mathbf{n}$ is the normal vector to the boundary, g is the surface conductance of the electrode and V_o is the voltage of the electrode on the metal side. This does not consider any capacitive effects. Only the magnitude of the impedance in a similar *quasi-static* condition is considered.

Numerical solution

After the geometry of the model is formed, the differential equations to be solved including the simplifications are specified and the boundary conditions and initial values are defined, the problem and the differential equations should be solved numerically as deriving any analytic solution of the realistic problems is nearly impossible. Different methods may be used to solve the aforementioned differential equations numerically. Discretisation methods used are the finite difference method (FDM), finite element method (FEM) and finite volume method (FVM). How these methods differ is beyond the scope of this thesis. The FDM is not suited for complex geometries, thus, easily ruled out for the type of volume conductor model presented in this chapter. The differences between FEM and the FVM are, however, more involved and require a deeper understanding of the underlying mathematical methods. Due to the availability of well-established methods and platforms in solving the problem using FEM and its near monopoly in the literature in solving similar problems, COMSOL Multiphysics (COMSOL, Ltd., Cambridge, UK) operating based on FEM was chosen. A Brief description of FEM can be found in Appendix A.

3.2.3 Modelling electrical stimulation

So far, two major modelling components in the bio-modelling context have been introduced: cable models of an axon and models of the volume conductor. This section reviews the literature, aiming at bringing these two models together, in an attempt to model the response of the neural tissue to an extracellularly generated field. One of the first attempts to derive analytic formulations for the neural excitation as a function of the stimulus assembly parameters was that of Rushton's [115] in his study on frog's sciatic nerve. He formulated an expression to predict the effect of the electrode spacing and the orientation of an electrode pair, with respect to a fibre, on the current required to stimulate the fibre. This work together with [116, 117] provided an invaluable theoretical basis for the ensuing research. An interesting concept was the *liminal length* in [117] which agrees well with the Fourier type description stated above, aimed to quantify the minimum length of the fibre whose potential should be elevated to generate an excitation. A very large f_x (i.e., a very short spatial variation) results in a very small time constant which dies out very quickly.

Aligned with the above-mentioned goals, another important contribution was that of McNeal's [80]. Considering sub-threshold variations for all the nodes and incorporating ionic currents for the node closest to the source, he created a paradigm for the analysis of the effect of the extracellular stimulation.

Activating function

Activating function (AF) gives a heuristic understanding of the positions of the hyperpolarisation and depolarisation along an axon exposed to external stimuli. Building on the pioneering work by McNeal [80] on the quantification of the response of a fibre to extracellular stimuli, the AF was introduced by Rattay [118]. To understand the concept a segmented view of an axon is considered as shown in Figure 3.5. Defining $V_n = V_{in} - V_{on} + V_{rest}$, for the n^{th} node, the relationship

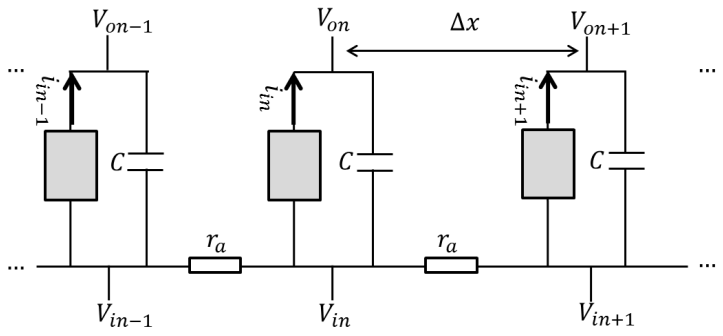

Figure 3.5: Cable model of a fibre for the description of the AF.

shown in Equation (3.29) holds.

$$\frac{dV_n}{dt} = \frac{(\frac{1}{r_a \Delta x}).(V_{n-1} - 2V_n + V_{n+1} + V_{on-1} - 2V_{on} + V_{on+1}) - (\pi d \Delta x).I_{in}}{(\pi d \Delta x) C_m} \quad (3.29)$$

where r_a is the resistance per meter and is given by $\frac{4\rho_i}{\pi d^2}$ [118], in which ρ_i is the resistivity of the axoplasm, d is axon diameter, C_m is the capacitance per m^2 and I_{in} is the current per m^2 of the n^{th} node. Consequently as $\Delta x \to 0$ for an unmyelinated fibre, the expression transforms to Equation (3.30).

$$\frac{\partial V}{\partial t} = \frac{(\frac{1}{r_a \pi d}).(\frac{\partial^2 V}{\partial x^2} + \frac{\partial^2 V_o}{\partial x^2}) - i_i(V,t)}{C_m}. \quad (3.30)$$

Therefore, at the rest potential, $\frac{\partial^2 V_o}{\partial x^2} > 0$ for positive variations of V (i.e., the AP generation). This is the basis of the introduction of the AF as the second spatial derivative of the extracellular potential. Consequently, in a similar fashion for a myelinated fibre the AF is the second spatial difference from a node to the other as shown in Equation (3.31).

$$AF = \frac{\Delta^2 V_o}{\Delta x^2} = \frac{V_{on-1} - 2V_{on} + V_{on+1}}{l^2} \quad (3.31)$$

where l is the node to node distance.

Rattay then expanded the idea to surface electrodes [119] and formed computer

simulations [120] (as opposed to analytic methods up to that point) to investigate how the subthreshold variations of the potential are governed. If merely the extracellular potential is considered, characteristics of the fibre are ignored. Such an approach may provide an insight into the development of the neuroprosthetics at an early stage. Other studies also implemented the concept in the design of the stimulation electrodes [27, 121].

Zierhofer in an analytic study [122] compared different techniques in modelling. He categorised models as the non-linear dynamic and sub-threshold. He asserted that the AF cannot be considered as sub-threshold as it does not consider the fibre characteristics and only relies on the extracellular potential. Subthreshold models are interesting as they are simple and easy to use. Zierhofer solved the underlying equations in the frequency domain to propose a new method for the sub-threshold study and showed a considerable difference with the results shown by the AF. Therefore, the use of the AF should be limited to reaching a preliminary general understanding of the sub-threshold depolarisation regions.

Hybrid models

In a realistic design scenario, more sophisticated and complex models should be implemented and simple and specific analytic models may not help significantly in the design. It was shown that the extracellular potential changes the response of the fibre by modifying the transmembrane potential locally. Therefore, it is possible to solve the potential field in a volume conductor model then insert the values as boundary conditions for a cable model having specific characteristics. This modelling paradigm constitutes the so-called hybrid model. Table 3.1 summarises some of the key contributions with reference to the volume conductor model (VCM) used and the type of the fibre model (FM) implemented.

Table 3.1: Key contributions in the literature on developing hybrid models.

Ref.	Year	VCM	FM	Approximation	Notes
[123]	1999	FDM	[80, 81]	-	1
[124]	2002	FEM	[17]	Quasi-static	2
[125]	2004	FEM	[17]	Quasi-static	3
[126]	2005	FEM	[17]	Frequency adjusted	4
[127]	2008	FEM	[17]	-	5
[107]	2009	FEM	[17, 81]	Frequency dependent	6
[128]	2010	FEM	[17]	Quasi-static	7
[129]	2010	FEM	[81]	Quasi-static	8
[130]	2011	FEM	[17]	-	9
[84]	2011	FEM	[79, 80]	Quasi-static	10

Continued on next page

[1]This study was one of the first instances of using hybrid models using a 3D volume conductor. A 3D model of the inhomogeneous spinal cord, incorporating grey and white matters and different anatomical features, was developed to investigate the spinal cord stimulation. They used human data in [104] in their model.

[2]To investigate the influence of the stimulus waveform and frequency in the spinal cord stimulation, a model of the spinal cord and a full cell model (i.e., soma, dendrites, axon) were developed. The quasi-static approximation was used.

[3]They used a 2D axisymmetric model of electrodes and the brain and a full cell model to investigate the frequency dependent excitation and inhibition of cells and the spatial extent of the stimulus penetration. The quasi-static approximation was used.

[4]They used a 2D axisymmetric model of electrodes and the brain and axon models to investigate the effect of the electrode tissue impedance on the volume of the tissue excited. The quasi-static approximation was used but the data was scaled and phase shifted for different frequencies to mimic a frequency analysis.

[5]A 3D model of the proximal human femoral nerve and an array of cuff electrodes in tandem with a double layer cable model were used to investigate the effect of the electrode configuration on the selectivity.

[6]A 3D model of the arm, representing different layers, and surface electrodes was developed to investigate the effect of the transcutaneous current stimulation when using different cable models. It was shown that the MRG model agrees well with the experimental results. A variation of Ampere's law was used to take into account the effect of permittivity.

[7]A 3D model of the forearm and a double layer cable model were used to test the influence of the electrode size on selectivity in the transcutaneous electrical stimulation. A quasi-static approximation was used.

[8]A 3D model of the torso and spinal cord and a cable model of the fibre with the myelin represented as a perfect insulator were developed/used to investigate the human lumbar spinal cord stimulation with implanted and surface electrodes. The quasi-static approximation was used and a clear description of boundary conditions was given.

[9]A 3D model of the human torso and the double layer cable model were used to investigate if the human lumbar posterior columns can be stimulated using transcutaneous electrodes.

[10]A 3D model of the rat sciatic nerve and transverse intrafascicular multichannel electrode in tandem with a cable model with perfect myelin insulation were developed. The quasi-static approximation was used and a complete set of tools for testing the model validity and boundary conditions were given.

Ref.	Year	VCM	FM	Approximation	Notes
[131]	2012	FEM	[80, 132]	-	[11]
[133]	2012	FEM	[17]	-	[12]
[92]	2013	FEM	[79]	Quasi-static	[13]
[85]	2013	FEM	[81]	-	[14]
[134]	2013	FEM	[80]	-	[15]
[135]	2014	FEM	[17]	Quasi-static	[16]
[136]	2014	FEM	[80]	Quasi-static	[17]
[137]	2015	FEM	[83]	Quasi-static	[18]

This is a collection of robust hybrid models which have been used to model various stimulation parameters. Based on the theoretical review presented so far and the extensive literature review, the framework for the modelling presented in this chapter should be readily justified as discussed in the following lines.

3.2.4 Objectives

As discussed in Chapter 2, the reported current levels for the trans-rectal neuromodulation of the pudendal nerve are excessively high. Any feasible solution

[11] A 3D model of the human sciatic nerve with an ensemble of randomly placed fascicles and a linearised MRG model were used to investigate the selectivity. A large number of computer simulations were used in this study.

[12] A 3D model of deep brain stimulation electrodes and the surrounding medium and a model of the nerve cell were used to optimise the spatial targeting of deep brain stimulation leads.

[13] A 3D model of the rat spinal cord and a full cell model, in which axons were modelled by single layer cables with the imperfect myelin insulation, were used to model the epidural electrical stimulation of spinal sensorimotor circuits. The quasi-static approximation was used.

[14] A 3D model of the pudendal nerve and fascicles and the flat interface between the nerve and electrode and the round cuff design was developed in tandem with a cable model of the axon in which the myelin insulation was perfect. Different realistic nerves were reshaped depending on the electrode assembly shape. The selectivity of different electrode configurations was investigated.

[15] A 2D axisymmetric model of the pudendal nerve and a simplified cable model of the axon were used to investigate the activation of peripheral nerve fibres by the electrical stimulation in the sole of a foot.

[16] A 3D model of the human head and deep brain stimulation leads and a double layer cable model of the axon were used to investigate an endovascular approach in the deep brain stimulation. A quasi-static approximation was used.

[17] A 3D model of the spinal cord and a cable model of the nerve fibre in which the myelin was considered as a perfect insulator were used to compare the intra and extradural electrode arrangements of the spinal cord stimulation. A quasi-static approximation was used.

[18] A 3D model of the vestibular nerve and the structures in the vicinity as well as a single layer cable model with the myelin represented as a perfect insulator were used to establish a framework for the electrical stimulation of the vestibular nerve. A quasi-static approximation was used and a very elaborate FEM model validity test was adopted.

intended for a chronic use should attempt to minimise this current as such high levels of current may increase the chance of tissue and electrode damage, there is a possibility of stimulating other structures in the vicinity and the battery of the device is exhausted rapidly if the integration of the electronics is intended.
First, a set of studies should establish the properties of the tissue in terms of its conductivity. Then, the nerve should be traced. Finally, using a hybrid model of a device *in situ* it should be investigated whether or not it is possible to minimise the stimulus current. This may be achieved by investigating the effect of placing the electrodes in different positions on the device on the threshold at which the stimulus may excite the target nerve.
Given that the target device is not an implant, the effect of variations along the trajectory of the nerve should be considered.
In the following sections, first the materials and methods in achieving the above-mentioned goals are discussed. Subsequently, the results and discussions are presented.

3.3 Material and method

3.3.1 Tissue conductivity

Very often the exact values of model parameters, such as the conductivity of a layer, are not accurately known or only a range of values may be found in the literature. A reverse verification method of the model was adopted. Such a verification method is the one in which an experiment is performed, a model of the experimental setup is made and the parameters are varied in the range reported in the literature to agree with the experimental results. This, essentially, constitutes a fine-tuning of the parameters.
With the approval of the local research and development committee, a test of the electrical stimulation of a male volunteer for the purpose of extracting the tissue conductivity data was performed. The probe shown in Figure 3.7a was

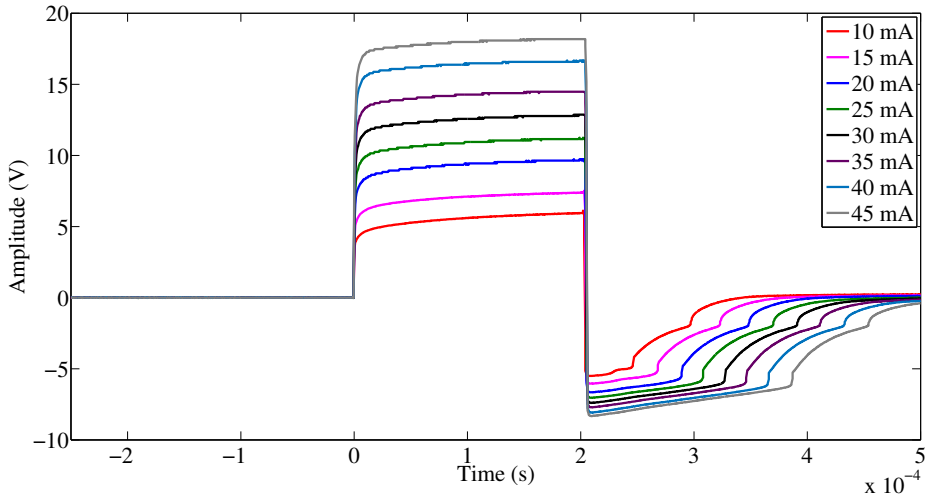

Figure 3.6: Voltage across a pair of stimulation electrodes with the device *in situ* for various stimulus pulse amplitudes. The resistance of the tissue is almost linear for the range of applied stimulus pulse amplitudes. Note that the irregular shape of the charge balancing cycle is due to the medical stimulator used which is irrelevant in the presented study.

inserted through the anal orifice of a male volunteer. As a reminder, a similar device was used in the study by Craggs *et al.* [8]. The device was made of silicone rubber and the electrodes were 316 medical grade stainless steel. One pair of the stimulation electrodes were connected to a DS7A constant current stimulator (Digitimer Ltd, Hertfordshire, UK), supplied by an isolated power supply. The voltage compliance of the stimulator was set to its maximum, 200 V, and 200 μs pulses of different amplitudes were applied (the anode as the source and the cathode as the sink) and the voltage across the pair of electrodes was recorded in each case using a DSOX2024A oscilloscope (Agilent Technologies, Santa Clara, US), also supplied by the same medical grade isolated power supply. Since the subsequent decisions in the progression of the modelling study directly relate to the aforementioned study, the results of this experiment are presented in this section. The results can be found in Figure 3.6. What is of significance for the subsequent modelling study is to ascertain whether or not the resistance is linear in the range of the stimulus currents applied. The electrode-tissue interface impedance may be modelled as a parallel combination of a resistor and a capac-

itor (R_{ct} and C_{dl}), in series with a resistor to represent the tissue (R_t) as the tissue may be considered only resistive in the frequency range of concern. The electrode-tissue modelling is discussed in detail in Chapter 4, but here only the temporal response of such a system is of interest. To arrive at this temporal temporal response, the impedance of the electrode and tissue system (Z_s) should be multiplied by the Laplace transform of a step ($\frac{I_{pk}}{s}$), where I_{pk} is the amplitude and s is the Laplace variable. Consequently, by getting the inverse transform, the temporal response may be derived as shown in Equation (3.32):

$$\begin{aligned} \frac{I_{pk}}{s} \times Z_s &= \frac{I_{pk}}{s(\frac{1}{R_{ct}}) + sC_{dl}} + \frac{I_{pk}R_t}{s} \\ &= \frac{I_{pk}\frac{R_{ct}}{R_{ct}C_{dl}}}{s(\frac{1}{R_{ct}C_{dl}} + s)} + \frac{I_{pk}R_t}{s} = V(s) \\ &\Rightarrow V(t) = I_{pk}R_t(1 - e^{\frac{t}{R_{ct}C_{dl}}}) + I_{pk}R_t u(t) \end{aligned} \tag{3.32}$$

where $u(t)$ is the step function. Thus, based on (3.32), the sharp rise of the voltage upon the application of the stimulus current is that across the tissue. The resistance is relatively linear although not completely. The slight non-linearity may be due to the variation of the contact between different episodes of the current application. For 45 mA amplitude of the applied current, the voltage across the tissue is about 16 V. This result was used in the subsequent modelling attempts.

3.3.2 MRI study

To find an approximate course of the pudendal nerve and identify the main anatomical features and their relative distances with respect to the stimulator *in situ*, an MRI study was performed. As mentioned in Chapter 2, originating from the either side of the sacral cord, the pudendal nerve enters the gluteal region through the lower part of the sciatic foramen. Turning around the sacrospinous ligament near its attachment to the ischial spine, the pudendal nerve re-enters the perineum via the lesser sciatic foramen. Running along the edge of the ischioanal

fossa, the nerve passes in the vicinity of the ano-rectal junction [36]. The MRI study intended to identify an approximate course of the nerve in this last section. With the approval of the local research and development review, the device shown in Figure 3.7a was used for an MRI study on a male volunteer. The metallic electrodes were removed and water based gel was injected in the position of the cathodes to make their positions visible in the MRI scans. Using a 1.5 T MRI instrument, a set of transverse and sagittal MRI scans was taken of the subject with the device *in situ*. The Syngo fastView software (Siemens Healthcare, UK) was used to study the MRI scans. To derive a global coordinate system, the coordinates were defined as shown in Figure 3.7. The x axis was defined along the axis of the device while y and z were defined orthogonal to that accordingly. The origin was defined inside the device between the cathodes. While the y and z coordinates were readily measured, the x coordinates were found by dividing the spacing of the transverse planes by $sin(\theta)$, where θ was the angle device makes with the horizontal axis of the sagittal plane shown in Figure 3.7b.

The cross sections of the pudendal nerve at the edge of the ischoanal fossa were approximated in the transverse planes as shown in Figure 3.7c in nine slides and their corresponding coordinates were measured. Different anatomical features and their respective sizes and positions were noted based on the transverse and sagittal planes. By a cubic spline interpolation of the cross-sections found in the MRI study, a smooth and densely sampled course of the nerve was then defined in MATLAB R2014a (MathWorks, Inc., Natick Massachusetts, US).

As discussed in Chapter 2, the pudendal nerve is paired as it symmetrically runs on the left and right sides of the pelvis. Due to the symmetry of the lateral branches, in all the subsequent modelling studies, one side of the pudendal nerve was considered in terms of the effect of the extracellular field.

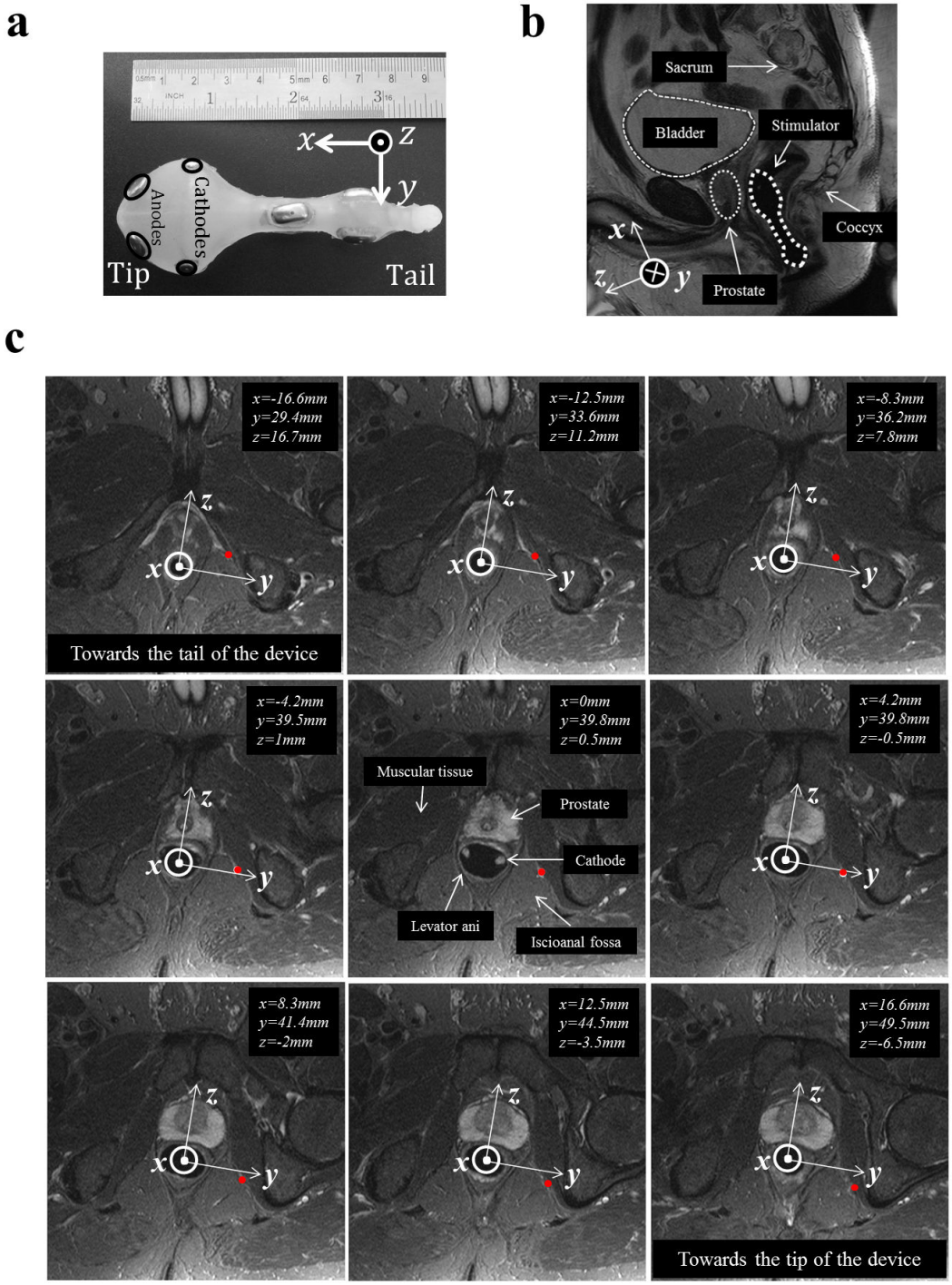

Figure 3.7: The device used in the preliminary studies and the MRI scans of the pelvic region with the device *in situ*: (a) shows the device, (b) is the sagittal plane with the anatomical features while the device is delineated and (c) shows nine transverse planes of the MRI with the cross-sections of the pudendal nerve approximated at the edge of the ischioanal fossa fatty tissue as marked by red dots. (b) adapted from [70].

3.3.3 Volume conductor model

Based on the MRI study, a volume conductor model of the stimulator and the pelvic region was constructed as shown in Figure 3.8 in COMSOL Multiphysics 4.3 (COMSOL, Ltd., Cambridge, UK). Apart from the main anatomical features around the stimulator *in situ*, three main tissue layers around it, each of which composed of structures of relatively similar conductivities, were considered. Layer 1, immediately around the stimulator, is the intestinal tissue and the levator ani muscle. Layer 2 represents the fatty tissue of the ischioanal fossa and the connective tissue between organs. Layer 3 is the pelvic floor musculature. All the subsequent simulations were run on a computer with 3.4 GHz Intel i7-2600 CPU and 16 GB RAM. A quasi-static approximation of Maxwell's equations was used to simulate the electric potential in the model. The exact methods of applying such formulations in COMSOL are mentioned here. In the *AC/DC* module of COMSOL, *Electric Currents* physics in *Stationary* setting was selected. The software solves $\nabla.J = Q_j$, $J = \sigma E + J_e$ and $E = -\nabla V$ where J is the current density, Q_j is the current source, E is the electric field and J_e is the external current density. By setting Q_j and J_e to zero everywhere in the model, a quasi-static approximation is implemented.

The subsequent stages of modelling are optimisation in nature. Thus, a linear process cannot be defined to fully understand the methods. Some features of a preceding section will be discussed in the succeeding sections.

Boundary condition and discretisation

A sphere was defined around the model as shown in Figure 3.8 and Dirichlet boundary condition ($V = 0$) was applied to the external boundaries of the said sphere. This would implement an approximation of the ground at infinity ($V_\infty = 0$). Given the insulation at the boundary of the body, this medium was set to be non-conductive ($\sigma = 10^{-10}$ S/m to avoid discontinuity). Since the current spread is mainly localized in layer 1 and spreads slightly in layer 2, as will be quantified

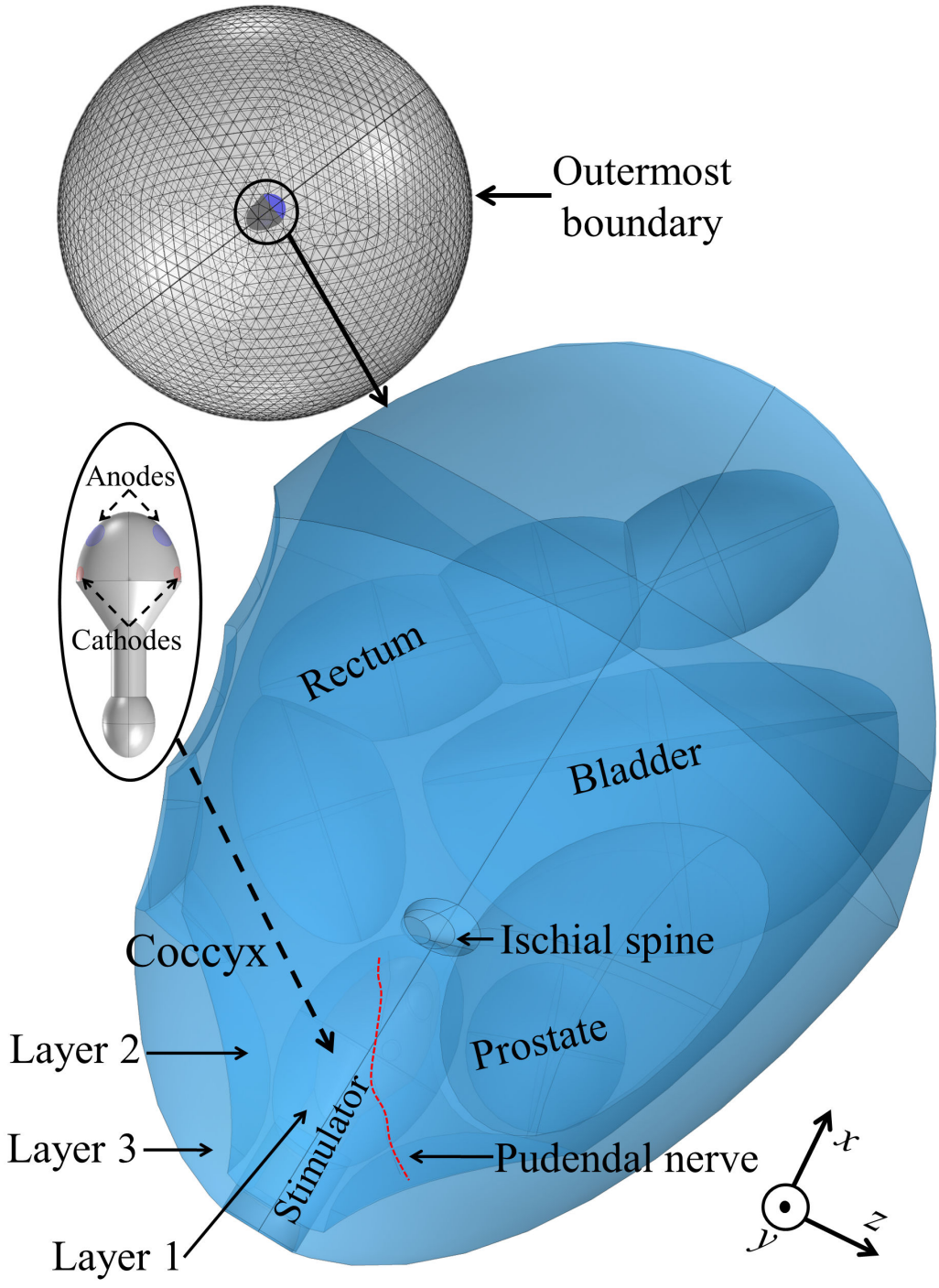

Figure 3.8: Volume conductor model of the pelvic region with the device *in situ*. The model of the device used in the preliminary study, the outer boundary of the model for $V = 0$ at infinity approximation, and different pelvic features are explicitly defined. Figure adapted from [70].

in the subsequent section, ignoring the other body structures is assumed not to affect the modelling outcome. For implantable devices, the conductivity of the engulfing medium is generally set to that of saline. However, given the size of the stimulator and that the external boundary of the model extends almost to the boundaries of the body, this medium was set as insulation. The model was discretised using non-uniform free tetrahedral elements, while it was more finely meshed in layer 1 and 2 by adjusting the maximum element size. This resulted in a total of about 1.2 M elements (about 1.6 M degrees of freedom).

The electrodes were defined as equipotential surfaces on which the current density distribution was non-uniform. In all the following cases, the anodes were set as the source of a total of 1 mA while the same amount was set to sink in cathodes. This was implemented in COMSOL by *Terminal* current of a negative value for the cathodes and a positive value for the anodes. The electrode-tissue interface contact impedance was ignored under the quasi-static assumption as only the potential at the tissue side is of interest. The way current density re-distributes itself on the surface of the equipotential electrode is an important feature which has been incorporated in the model.

After adjusting the conductivity of different media as discussed in the subsequent section, the radius of the external sphere was changed from 50 cm to 200 cm in steps and the resulting simulated electric potential along the trajectory of the nerve was recorded. These variations would only introduce a shift in the electrical potential along the nerve. When the radius of the external sphere was set to 90 cm, even doubling the radius size would result in less than 1% change in the result. Thus, the radius of the external sphere was set to 90 cm.

By adjusting the maximum element size in layer 1 and 2, the number of elements was changed from about 1.2 M to 7 M in steps. The results, in terms of the electric potential along the nerve, changed only by about 1% while the simulation time at the lowest discretization level was 3% of that of the highest. Above this discretization level, the computer ran out of memory. Thus, about 1.2 M element

count size was considered to be sufficient.

Conductivities

The body of the stimulator was set to be non-conductive ($\sigma = 10^{-10}$ S/m). A range of values are reported for the conductivity of the muscle and fat at low frequencies. The conductivity of layer 1 in the model was set between 0.2 S/m and 0.4 S/m in steps and the conductivities of the rest of the components of the model were set to their typical values. The corresponding simulated maximum voltage drop between the electrodes was recorded in each case. Similarly, the conductivity of layer 2 was set to 0.03 S/m and 0.05 S/m and the maximum simulated voltage drop was recorded. The variation in the maximum voltage drop due to variations in the conductivity of layer 1 was 214.5 V/S while variations in the conductivity of layer 2 resulted in 15.78 V/S of variation in the maximum voltage drop. This confirms that the current is mainly confined to layer 1. The conductivity of layer 2 and other components in the model were set to their typical values and the conductivity of layer 1 was swept across a range reported in the literature. A conductivity resulting in the maximum voltage drop across the electrodes consistent with the previous experimental measurements shown in Figure 3.6 was assigned to layer 1. All the conductivities were assumed to be isotropic due to the complex formation of the structures. Table 3.2 summarises the conductivities of different components of the model.

It is expected that the electrode-tissue contact impedance has a minimal effect on the simulated neural activation thresholds in a current-controlled bipolar stimulation setting. This is due to the fact that the contact impedances of the electrodes and the impedance of the tissue are all in series and the same current should pass through them. This agrees with the previous studies [107, 126].

3.3.4 Nerve model

Myelinated afferent fibres in the pudendal nerve were modelled by double-layer cable models based on the MRG model with an explicit representation of nodes

Table 3.2: Conductivities of different structures in the developed model.

Model component	**Structure**	**Reported conductivity $S.m^{-1}$ (selected values)**
Layer 1 (intestinal tissue, muscle)	Rectal-anal wall, levator ani muscle	0.2 - 0.4 [112, 138–140] (0.4)
Layer 2 (connective tissue, fat)	Ischioanal fossa, ligaments	0.03 - 0.05 [112, 138–140] (0.04)
Layer 3 (muscle)	Pelvic floor, obturator	0.3 - 0.4 [112, 138–140] (0.4)
Prostate	Prostate	0.3 - 0.4 [112, 138–140] (0.4)
Bladder	Bladder	0.2 [112, 138–140] (0.2)
Rectal content	Feces or gas	0.1 or 10^{-5} [141] (0.1 or 10^{-5})

of Ranvier with active and passive properties. The compartments between the subsequent nodes only had passive properties. The compartments with passive properties between every two active nodes included two MYSA compartments, two FLUT compartments, and ten STIN compartments. The number of STIN compartments was increased compared to the original MRG model to follow the curvature of the nerve well.

The fibre diameters based on the contribution by Schalow *et al.* [142] were set to follow a normal distribution of 12 μm mean with a standard deviation of 1 μm. It should be noted that as the overall study is a comparative study of different stimulation scenarios, the exact mean diameter may not affect the outcome. As shown in Figure 3.9, the geometric properties of each fibre were linearly interpolated with respect to the fibre diameter to derive the values based on experimental data reported by McIntyre *et al.* [17].

In Matlab, a fibre diameter value within the distribution stated above was generated. A node of Ranvier was then randomly placed between 0 and Δx of the arc-length of the nerve previously generated, where Δx was the corresponding node to node distance for the said fibre diameter. All the passive compartments, whose geometric parameters were found by a linear interpolation based on the fi-

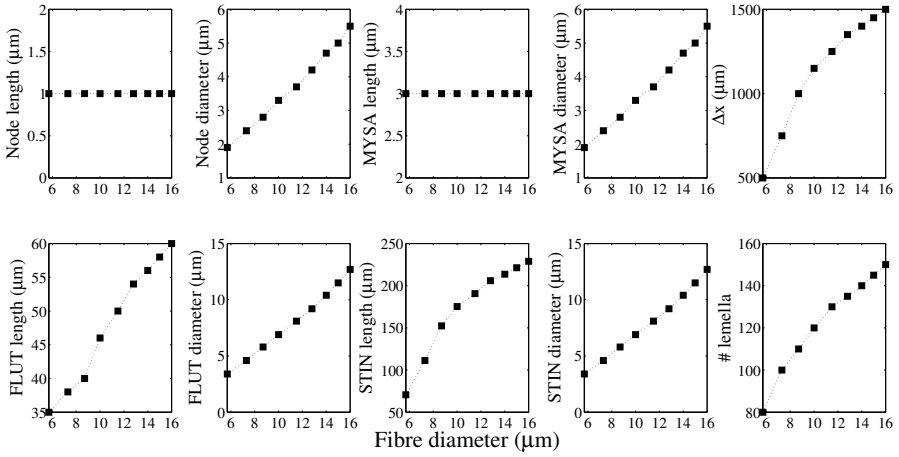

Figure 3.9: The geometric parameters of fibre models as a function of the fibre diameter based on [17].

bre diameter, were placed along the arc-length between every subsequent node in sequence until no more compartments could be added. The fibre was terminated by a node. These steps were repeated 100 times for this approximately 5 cm long nerve section. The geometric properties of all the fibres and the number of compartments and their position along the arc-length of the nerve were exported to Neuron 7.3 [143] to create 100 double layer cable models of the myelinated axon with imperfect insulation of the myelin sheath. The electrical parameters of the fibres were set consistent with what is shown in Table 3.3 based on the work in [17] for 2000 channels per μm^2 for fast Na channels and 100 channels per μm^2 for slow K channels. The underlying HH-type differential equations for the channel mechanisms were imported based on the work in [17] which can be found in Appendix B. These formulations can be accessed in [144] with the accession number 3810. The temperature was set to $36°C$.

A backward Euler integration with a time step of 10 μs was used to run the simulations. For all the compartments in the models, the number of segments or the spatial discretisation level was set to one (i.e., *nseg=1*) and unless otherwise stated the simulation was run for 10 ms. For higher discretisation levels the computer on which the simulations were running was not suitably fast.

Table 3.3: Electric properties of the model [17].

Property	Value
Nodal capacitance (c_n)	2 $\mu F/cm^2$
Internodal capacitance (c_i)	2 $\mu F/cm^2$
Myelin capacitance (c_m)	0.1 $\mu F/cm^2$
Axoplasmic resistivity (ρ_a)	70 Ωm
Periaxonal resistivity (ρ_p)	70 Ωm
Myelin conductance (g_m)	0.001 S/cm^2
MYSA conductance (g_a)	0.001 S/cm^2
FLUT conductance (g_m)	0.0001 S/cm^2
STIN conductance (g_m)	0.0001 S/cm^2
Maximum fast Na conductance (g_{Naf})	3 S/cm^2
Maximum persistent Na conductance (g_{Nap})	0.1 S/cm^2
Maximum slow K conductance (g_{Ks})	0.08 S/cm^2
Nodal leakage conductance (g_L)	0.007 S/cm^2
Na Nernst potential (E_{Na})	50 mV
K Nernst potential (E_K)	-90 mV
Leakage reversal potential (E_L)	-90 mV

3.3.5 Hybrid model

Coupling FEM results with the Neuron model, it was possible to simulate the response of the nerve to the extracellular potential generated by the trans-rectal stimulator. The electric potential vector along the nerve was exported to Matlab from COMSOL. This vector was interpolated and assigned to every compartment. A time vector and a potential vector were constructed to generate 200 μs pulses as used by Craggs *et al.* [8] in their study.

To simulate various stimulus current levels, the potential vector was multiplied. This is valid under the quasi-static approximation. The time and potential vectors were exported to the Neuron model and applied as the extracellular potential in each compartment (i.e., *e_extracellular*). For various applied current levels, equally spaced steps of 10 mA maximum length, the percentage of the fibres activated (PA) (n=100) along the trajectory of the nerve derived in the MRI study was recorded between 0 and 100%. The activation was defined as observing an action potential in the first and last nodes of a fibre. Thoroughout the rest of the presented study, the same method of the hybrid modelling is applied (i.e.,

volume conductor model + cable model). This method is schematically shown in Figure 3.10.

3.3.6 Nerve trunk modelling

In the model, the variations of the position of the fascicle containing the fibres in the nerve and the variations of the position of the fibres within a fascicle were ignored as more extensive set of variations are explored in this work. Also, since epineurium (EP) engulfing the fascicles is composed of a fatty tissue, and given that the nerve is passing through the fatty tissue of the ischioanal fossa in the area under study, the distinction between the two fatty tissues was not made. Furthermore, endoneurium (EN) and perineurium (PE) tissue layers in and around the fascicles were ignored. The EN has a distinct anisotropic conductivity (longitudinal=0.571 S/m, transverse=0.083 S/m) [127]. The PE, surrounding each fascicle and constituting 3% of the fascicle diameter, has a conductivity of only 0.002 S/m [127]. The dimensional ratios and the fact that the nerve is not placed in a single plane would increase the modelling complexity and the computation time would increase considerably if these features were to be incorporated.

To verify to what extent these assumptions change the results, a line, connecting the first and last cross-sections found in the MRI study, was formed to approximate the nerve. A cylinder of 4 mm diameter was defined around the linear approximation of the nerve to represent the EP. Another cylinder of 300 μm diameter was defined around the nerve to represent the EN. A thin layer of 9 μm was defined around the EN to represent the PE. This was done in COMSOL using *Contact Impedance*. Then, four more fascicles on four corners of the EP were defined as shown in Figure 3.11. To set the conductivity of the EN, a conductivity tensor was defined by defining a local coordinate whose main axis was defined in the direction of the nerve. The following lines summarise the methods in defining the conductivity tensor. Assuming a local Cartesian coordinate system for the nerve (x', y', z') in which the nerve trajectory is elongated along the x' axis, the

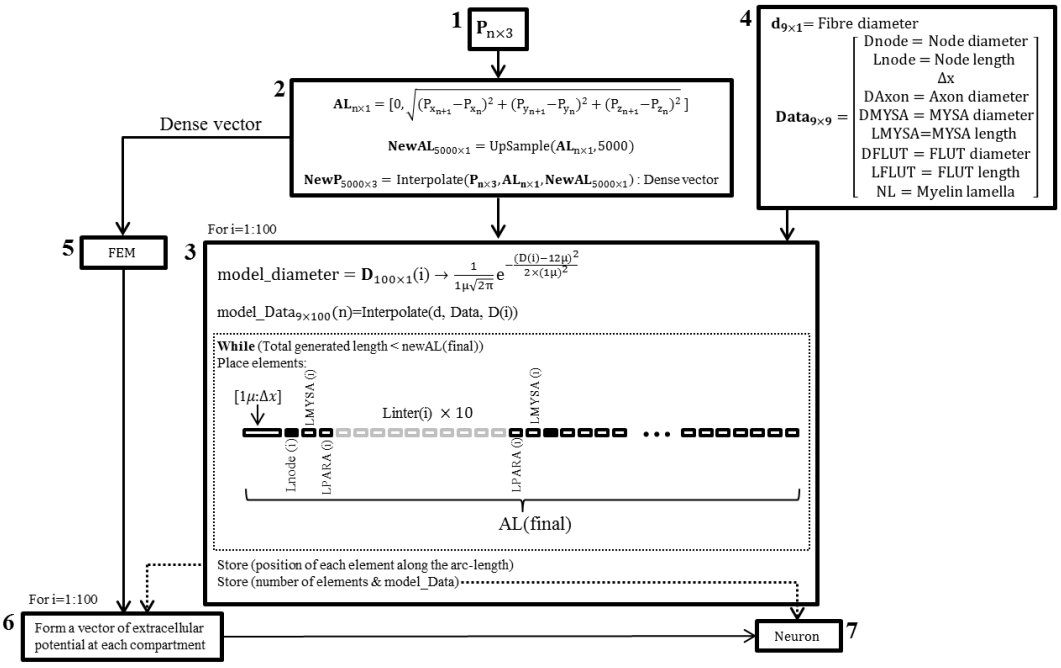

Figure 3.10: Hybrid modelling method schematic. This figure comprises of 7 blocks. In block **1** the coordinates of the cross-sections of the nerve trajectory (based on the MRI study or later the variations) are shown as a matrix (**P**). In block **2**, a vector (**AL**) is defined by considering the point to point distance of each cross-section in **P** as the arc-length of the trajectory. This arc-length vector is up-sampled and interpolated based on the initial coordinates and arc-length to generate a denser matrix of the coordinates along the initial trajectory of the nerve (**NewP**). **NewP** is used in block **5** in the FEM model to represent the nerve trajectory. The arc-length of **NewP** is also used in block **3** as will be described. In block **4**, nine fibre diameters and the corresponding experimental data are introduced. In block **3**, the following procedure is repeated 100 times. First, a random fibre diameter from a normal distribution is generated (model_diameter). Based on the said diameter, the model data (model_Data) are generated by linearly interpolating the data introduced in block **4**. The starting point of the fibre along the trajectory defined by **NewP** is uniformly randomly varied from 1 μm to Δx which is the node to node spacing for the intended fibre diameter. All of the sections are placed one by one in the appropriate order starting with a node while the incremental length of the fibre being formed is compared with the final element of **NewAL**. Adding sections continues until the difference between the length of the trajectory formed in block **1** and the fibre being formed exceeds Δx+ Lnode. The fibre is terminated with a node. The primary output of block **3** to block **6** is the arc-length vectors formed of the increments based on the length of each section for each fibre. The electric potential is solved along the main trajectory in block **5** and the data is presented versus the arc-length of the trajectory to block **6**, in which for the 100 fibres generated in block **3** appropriate electric potential vectors are generated. The said electric potential vectors, the number of elements and model_Data for each fibre are passed to block **7** to calculate the dynamic response of the fibres.

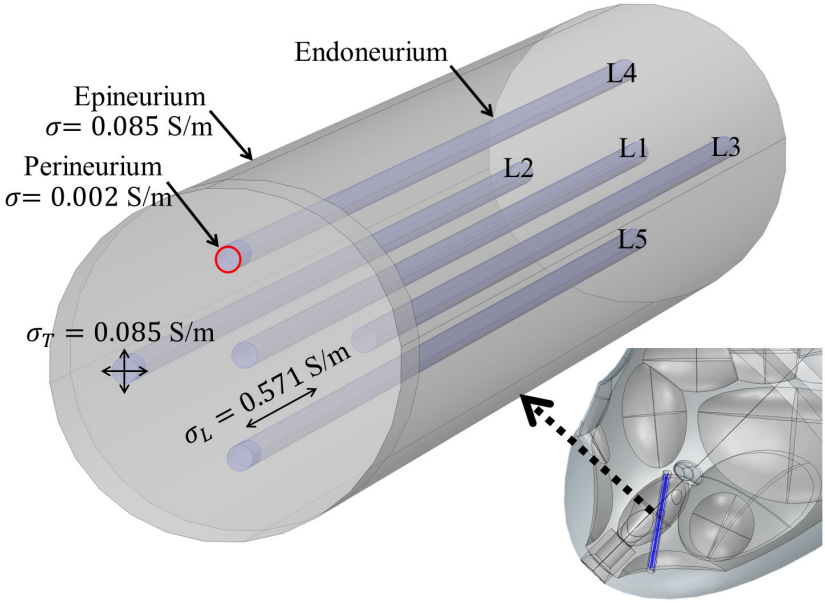

Figure 3.11: The linear approximation of the nerve and different tissue layers for five fascicles. The most central fascicle is the one that the trajectory derived based on the MRI study lies within. Figure adapted from [70].

conductivity of the EN is defined by the tensor shown in (3.33).

$$\sigma' = \begin{bmatrix} \sigma_L & 0 & 0 \\ 0 & \sigma_T & 0 \\ 0 & 0 & \sigma_T \end{bmatrix} \tag{3.33}$$

where σ_L and σ_T are the longitudinal and transverse conductivities, respectively. The variables x', y' and z' can be found based on x, y, and z in the global system as follows:

$$x' = \begin{bmatrix} cos(\theta_2) & 0 & sin(\theta_2) \\ 0 & 1 & 0 \\ -sin(\theta_2) & 0 & cos(\theta_2) \end{bmatrix} \begin{bmatrix} cos(\theta_1) & -sin(\theta_1) & 0 \\ sin(\theta_1) & cos(\theta_1) & 0 \\ 0 & 0 & 1 \end{bmatrix} \begin{bmatrix} 1 \\ 0 \\ 0 \end{bmatrix} \tag{3.34}$$

$$y' = \begin{bmatrix} cos(\theta_1) & -sin(\theta_1) & 0 \\ sin(\theta_1) & cos(\theta_1) & 0 \\ 0 & 0 & 1 \end{bmatrix} \begin{bmatrix} 0 \\ 1 \\ 0 \end{bmatrix} \tag{3.35}$$

$$z' = x' \times y' \tag{3.36}$$

where θ_1 and θ_2 are the angles of rotation around z and y' axes, respectively. Then the transformation matrix Q can be formed:

$$Q = \begin{bmatrix} x'_x & x'_y & x'_z \\ y'_x & y'_y & y'_z \\ z'_x & z'_x & z'_x \end{bmatrix}. \tag{3.37}$$

Subsequently, the conductivity tensor in the global coordinate system can be found as follows:

$$\sigma = Q\sigma' Q^T. \tag{3.38}$$

For various applied current levels in 10 mA steps, the PA (n=100) along the linear approximation of the nerve without the EP, PE, and EN was simulated. Then, the percentage of the fibres activated along the linear approximation of the nerve at the centre and its four corners of the EP with the PE and EN in place were simulated. The deviations of each approximation were noted. It will be shown that these approximations do not affect the decision making process in the optimisation process.

3.3.7 Optimisation

To re-iterate the objectives, the ultimate goal is to identify a configuration of the electrodes with which the activation of the nerve is achieved at the lowest possible current level. There is a limited space onto which the electrodes can be mounted on the body of the device. Utilising all the possible space on the surface of the device, modifying the original design slightly, a model of the device with 26 electrodes on its surface was developed as shown in Figure 3.12. All of the structural design parameters, expressed in Chapter 2, were maintained in the alteration. The electrodes were all designed to be 5 mm in diameter only based on practical considerations. The primed electrodes (i.e., 1′, 2′, ...) are facing the

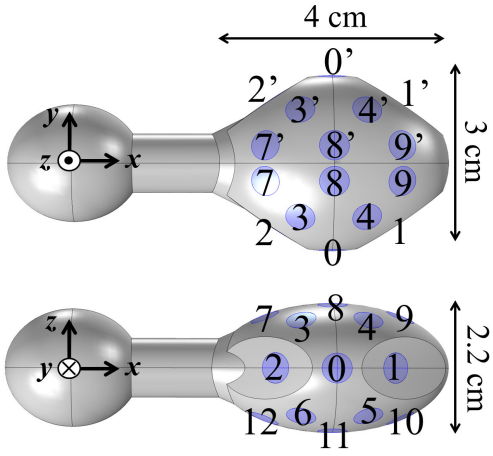

Figure 3.12: The first iteration of the modified design for optimisation. The primed electrodes face the lateral branch of the pudendal nerve which is not studied here.

lateral branch of the pudendal nerve which is not studied here. Having developed a design with a multitude of electrodes, one should devise a paradigm with which the current is applied. At this stage only the bipolar stimulation with a cathode and an anode was considered.

There are numerous possibilities of implementing two electrodes out of the existing 13 electrodes. Given that 0 electrode was identified to be the closest electrode to the target nerve, the number of possibilities could be minimised by incorporating this particular node in all the configurations to be tested. Having established this paradigm, there are 24 possible configurations by considering forward (i.e. using 0 electrode as cathode and x electrode as anode) and reversed (i.e. using 0 electrode as anode and x electrode as cathode) configurations. A naming convention regarding the configurations is introduced to be used throughout this chapter. The naming follows a $\#_{cathode}\#_{Anode}$ format where # refers to the corresponding number (e.g. 01 means that 0 electrode was used as cathode and 1 electrode as anode).

For all of the possible configurations, the current was increased from zero whilst the PA was monitored for a random population of the fibres. The current level at which 50% activation was achieved was noted. Based on the results (as presented

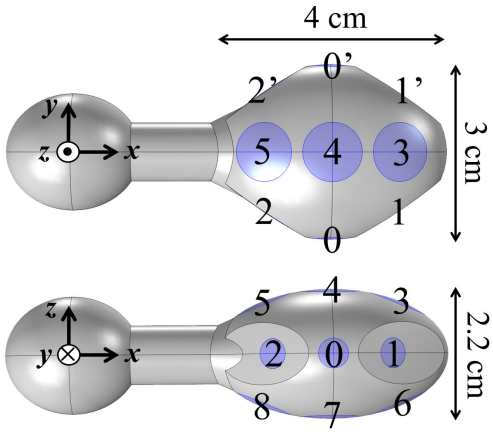

Figure 3.13: The second iteration of the modified design for the optimisation. Figure adapted from [70].

in the Results Section, considering the similarity of the level of the required current) the adjacent electrodes on the axis of the device were merged and the middle electrodes were removed to reduce the number of the electrodes. The resulting design is shown in Figure 3.13 in which the electrodes shared as the sink or source between $0'$ and 0 were designed to be 10 mm in diameter. For this new design, for all the possible configurations the current was varied from zero and the PA was noted from 0 to 100.

To have a heuristic view of the possible positions of the depolarization and hyperpolarisation along the course of the nerve, a normalized AF as the second spatial difference of the extracellular electric potential along the course of the nerve was calculated for the 100 random population of the randomly placed fibres for all of the 16 possible configurations. For the reversed configurations, to find the extracellular electric potential along the nerve, the electric potential simulated using FEM was multiplied by -1 to reduce the number of simulation runs. This is valid under the quasi-static approximation as the system is linear. For each fibre, the node to node distance (Δx) was based on the interpolation of experimental data as shown in Figure 3.9.

An important study is to investigate what the effects of different populations of 100 axons on the results are. This is important as the modelling process produces

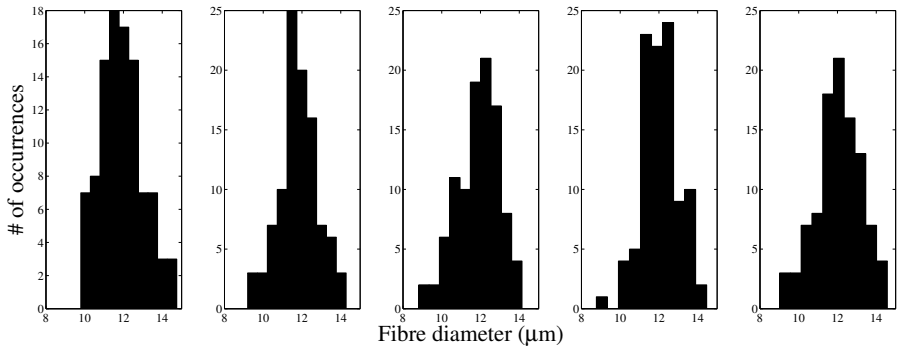

Figure 3.14: Histogram of diameter in 5 different populations.

different populations of the fibre diameter similar to the five populations shown in Figure 3.14. To test this, for the configuration yielding the lowest required threshold of the stimulus current, the variations in the required current for ten different populations were investigated.

As mentioned in Chapter 2, the pudendal nerve has been shown to have a frequency dependent neuromodulation response. Thus, for 10 consecutive pulses repeated at 5 Hz and 35 Hz the variations in the PA upon each pulse was simulated. Note that these variations are foreseen due to the long recovery cycle following an AP.

3.3.8 Nerve variation

The course and branching of the pudendal nerve has been shown to be variable in different individuals [35,37,141]. Also, the trajectory of the nerve with respect to the trans-rectal stimulator may be changing in different body postures. Thus, any optimization study should consider these variations. The variation of the position of the re-entrance of the nerve into the perineum has been quantified with respect to the ischial spine in cadaveric and ultrasound studies [37, 141]. Four points as shown in Figure 3.15 were selected along the trajectory of the nerve found in the MRI study. A variation pattern as defined in the variation matrix (V) in (3.39) was implemented (e.g., $a_x \pm 1$ means that the x component of point a can be changed uniformly randomly between -1 mm and +1 mm from

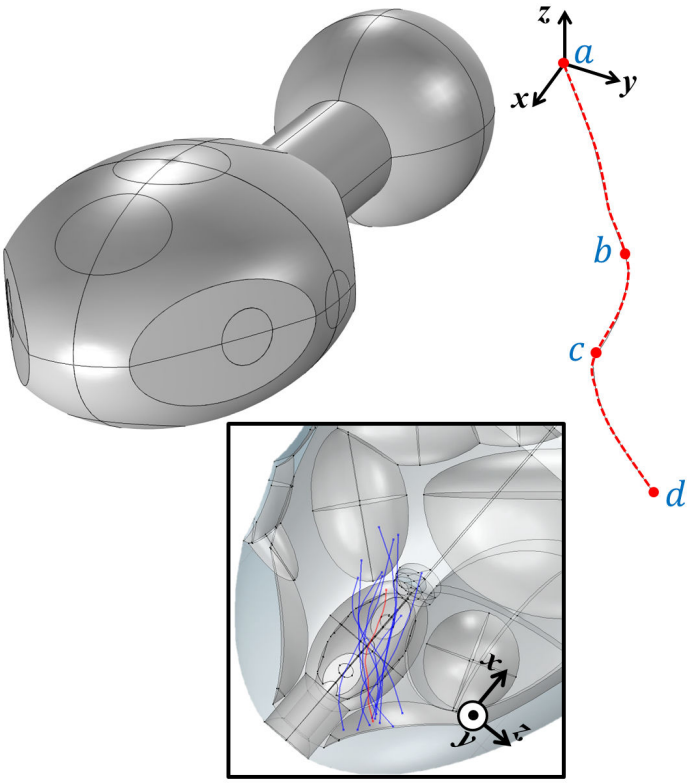

Figure 3.15: Four points along the nerve trajectory found in the MRI study which were varied to generate an ensemble of trajectories. The inset shows the resulting variations. Figure adapted from [70].

the point found in the MRI study):

$$V = \begin{bmatrix} a_x \pm 1.5 & a_y - 1 & a_z \pm 1.5 \\ b_x \pm 1 & b_y - 1 & b_z \pm 1 \\ c_x \pm 1.5 & c_y \pm 1.5 & c_z \pm 1 \\ d_x \pm 1.5 & d_y \pm 0.5 & d_z \pm 1.5 \end{bmatrix}. \tag{3.39}$$

The criteria for defining the matrix were to ensure that the resulting trajectories were generally confined in layer 2, as they anatomically would be, and they varied approximately to an extent reported in the literature. A total of 10 variations (here referred to as V1-V10) of the nerve were defined by the cubic spline interpolation of the four points in each case in Matlab. A minimum length of 4 cm was enforced for the trajectories. Also, a minimum distance of 5 mm was

enforced between all the similar points across different trajectories (e.g., between a points). If the trajectory was placed outside layer 2, the corresponding points were shifted or the trajectory was truncated manually after it was generated to place the whole length of the trajectory inside. Anatomic constraints imposed on generating the variations were as follows:

$$\begin{aligned} a_x < b_x < c_x < d_x \\ a_y < b_y < c_y < d_Y \\ a_z > b_z > c_z > d_z. \end{aligned} \tag{3.40}$$

This would ensure that the overall trajectory consistently originates near the ischial spine and terminates near the organs it innervates. The inset of Figure 3.15 shows the resulting variations. The dynamic response of each variation in terms of the PA versus the required current levels for a 200 μs stimulus pulse for 100 axons randomly placed along each of the trajectories was simulated as before for every configuration. Further, the AFs for each fibre and for each variation and for each configuration were also calculated based on the simulation results.

3.3.9 Tripolar configurations

As it will be shown in the Results Section, the outcome of the AF study indicated that the positions of the depolarisation and hyperpolarisation are the same for a given nerve trajectory and for all the electrode configurations in the majority of cases when similar types of configurations are considered (e.g., forwards configurations). It is trivial to show that a linear addition of the sources results in a linear addition of the voltages under the quasi-static assumption. This was also the assumption used in generating the temporal traces of the voltage. This, consequently, results in the linear addition of the AF which interprets into having the same position of depolarisation if the original sources resulted in depolarisation in similar positions. Based on this idea, the configurations requiring the lowest levels of current were merged. As 0 electrodes were used in all the configurations, this

resulted in a tripolar configuration. The benefit of a tripolar configuration is that understandably the field becomes more focused and current spread is reduced as also demonstrated in the literature [125].

3.3.10 Charge density

For the bipolar configuration resulting in the lowest required current, the charge density per area per phase for a 200 μs pulse along the diameter of 0 electrode was simulated for amplitudes ranging between 10 mA to 50 mA. It is noted that this is independent of the configuration as 0 electrode is present in all the configurations. For the same configuration and amplitude range, the charge density per area per phase along the main trajectory of the nerve was also simulated. The result of this specific study may be used to define the limits of the safe charge injection.

3.4 Results

3.4.1 Approximation of the nerve

Figure 3.16 shows the PA versus the amplitude of the 200 μs stimulus pulses for the main trajectory, the linear approximation of the nerve connecting the first and last points found in the MRI without the EP, PE, and EN tissue layers (Ln), the linear approximation of the nerve with all the tissue layers and four other fascicles around it in place (L1), and those of the fibres in the other four fascicles (L2-L5). There are various features of this plot which should be considered. Firstly, the current levels involved should be noted. The level is slightly higher than the levels reported based on the experimental trans-rectal stimulation of the pudendal nerve [8]. It has been shown that the MRG model results in a higher simulated threshold [17] but this might be due to the simplified nature of the model. Regardless of the exact value, as the study presented here is an optimisation attempt, the relative values should be considered. The other point is that the linear approximation of the nerve yields a relatively similar response, thus, this approximation is suited

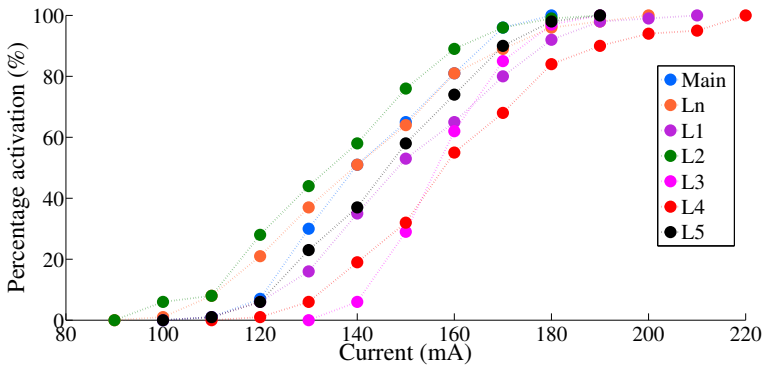

Figure 3.16: The percentage activation versus the required current amplitude in the main trajectory and the linear approximations of the nerve. Figure adapted from [70].

to investigate the result of other approximations. In the 50% activation region, the effect of having different fascicles around the target fascicle, the variation of the position of the fascicle and accounting for the EP, PE, and EN tissue layers introduce an average of about 15% variation. As it will be shown this is insignificant compared to the variations introduced by implementing different configurations. Nonetheless, these variations should be considered in a way that a configuration is not optimised unless it yields at least a 15% lower current level.

3.4.2 Thirteen electrode device

Figure 3.17 shows the required amplitude of a 200 μs pulse to activate 50% of the population of fibres for all of the 24 configurations (including forward and reversed configurations). This shows that the best configuration in terms of the lowest required current needs below 10 mA amplitude to activate the population while the worst configuration needs just below 140 mA. This result justifies the need for the optimisation process. Another feature of this result is that the electrodes placed between 0 electrode and the ones just off the main axis of the device (e.g., 4 and 3) yield relatively similar current levels compared to the ones near the axis. Therefore, they may be removed. Also, as a practical note, the electrodes just adjacent to each other near the axis of the device may be merged. This last point is not derived based on the results shown in Figure 3.17 but is

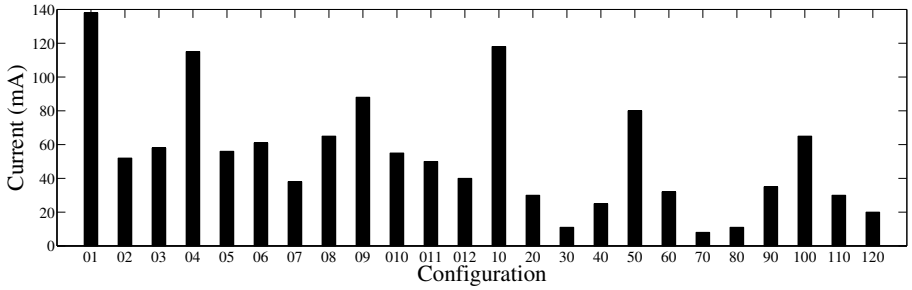

Figure 3.17: The required amplitude of a 200 μs pulse to activate 50% of the population of fibres for different configurations. Figure adapted from [145] with changes.

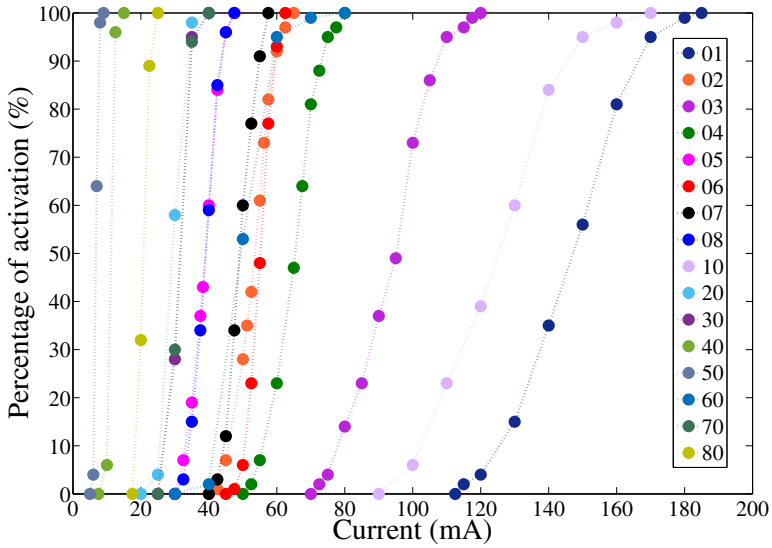

Figure 3.18: PA versus the amplitude of a 200 μs pulse for all of the configurations in the main trajectory. Figure adapted from [70].

merely a practical consideration.

3.4.3 Nine electrode device

Figure 3.18 shows the PA versus the amplitude of a 200 μs pulse for all the configurations while Figure 3.19 shows the AF along the length of the nerve for a population of 100 fibres for each possible configuration. Note that each coloured trace in Figure 3.19 is due to 100 traces. Regarding the PA versus current a very large difference between the best and worst configurations is observed, where the best is the one requiring the lowest level of current. The difference is nearly 20 fold, far more than the 15% error margin. The observations with

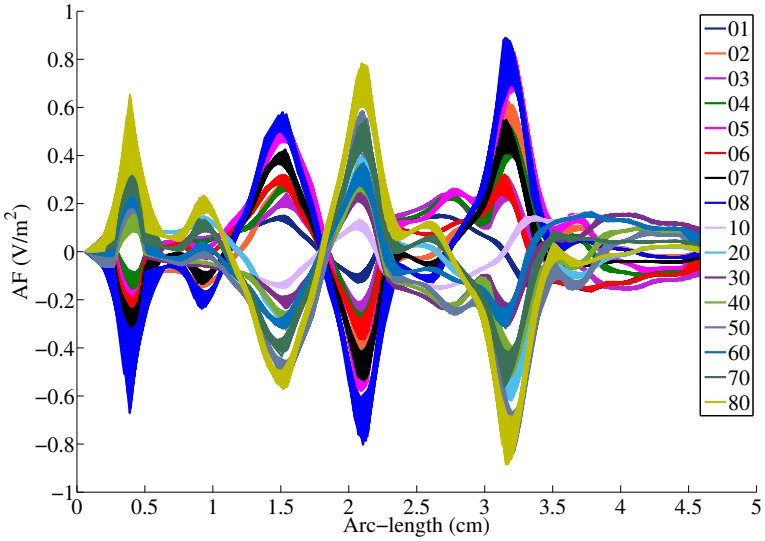

Figure 3.19: AF along the length of the nerve for a population of 100 fibres for each possible configuration. Figure adapted from [70].

respect to Figure 3.19 are equally interesting. The stochastic positioning of the fibre along a fascicle and the variation of the diameter of the fibres do not shift the AF plot as much as implementing different configurations does. Thus, the traces due to different configurations are discernible from each other. The other interesting feature of the results is that the position of the hyperpolarisation and depolarisation remains the same for all the forward configurations and for all the reversed configurations, respectively.

Effect of fibre population and frequency

Running the simulation for ten different ensembles of 100 axons for the configuration requiring the lowest level of current (50), the limits of the PA versus current curve showed negligible variations (±1%) although the slope showed slight variations in some cases (a maximum of 9%). This shows the validity of the 100 axon population as being sufficiently large to decide on the level of the current required. Using electrode configuration 50 and for a 100-axon random population, the 200 μs pulses were repeated at 5 Hz and 35 Hz. The amplitude was set to a level resulting in 100% activation for the first pulse. For the 5 Hz pulse repetition frequency, the time between every subsequent pulse was sufficiently large

to yield 100% activation for every pulse. However, for the 35 Hz pulse repetition frequency, the PA was at $86\% \pm 7\%$ (mean $\pm$ standard deviation) for 10 consecutive pulses. Thus, higher amplitudes may be required at higher frequencies to maintain a desired level of activation.

3.4.4 Nerve variations

Figure 3.20 shows the PA versus the amplitude of a 200 μs pulse for all the variations of the nerve and for all the configurations. For all the variations of the nerve the same two configurations require considerably lower current levels (40 and 50). A striking result is that no other configuration demonstrates a low required current level consistently across all variations. The range of the required current amplitudes also changes across variations and across the configurations although these variations are negligible for the two configurations (i.e., 40 and 50). For all the variations, the PA versus the current amplitude curves due to different configurations in each variation are parallel. That is, they generally do not cross each other. Only in one case for V9 and configuration 60 that is not the case. This means that generally the level of recruitment and the threshold consistently rise across different configurations. Figure 3.21 shows the AF plots for all configurations and for all the variations of the nerve. As before, each coloured trace shows the AF for a random population of 100 fibres, randomly placed along the nerve. Interestingly, for all the forward configurations and all the reversed configurations, in the majority of cases the peaks in the AF are in the same position. Only in V4 and V7 do the AF plots seem to peak at slightly different positions. Thus, the positions of depolarisation and hyperpolarisation essentially remain the same for all the configurations.

3.4.5 Tripolar configuration

Merging bipolar configurations 40 and 50 for which the lowest level of current amplitude was required to activate the population of fibres, thus, forming a tripolar

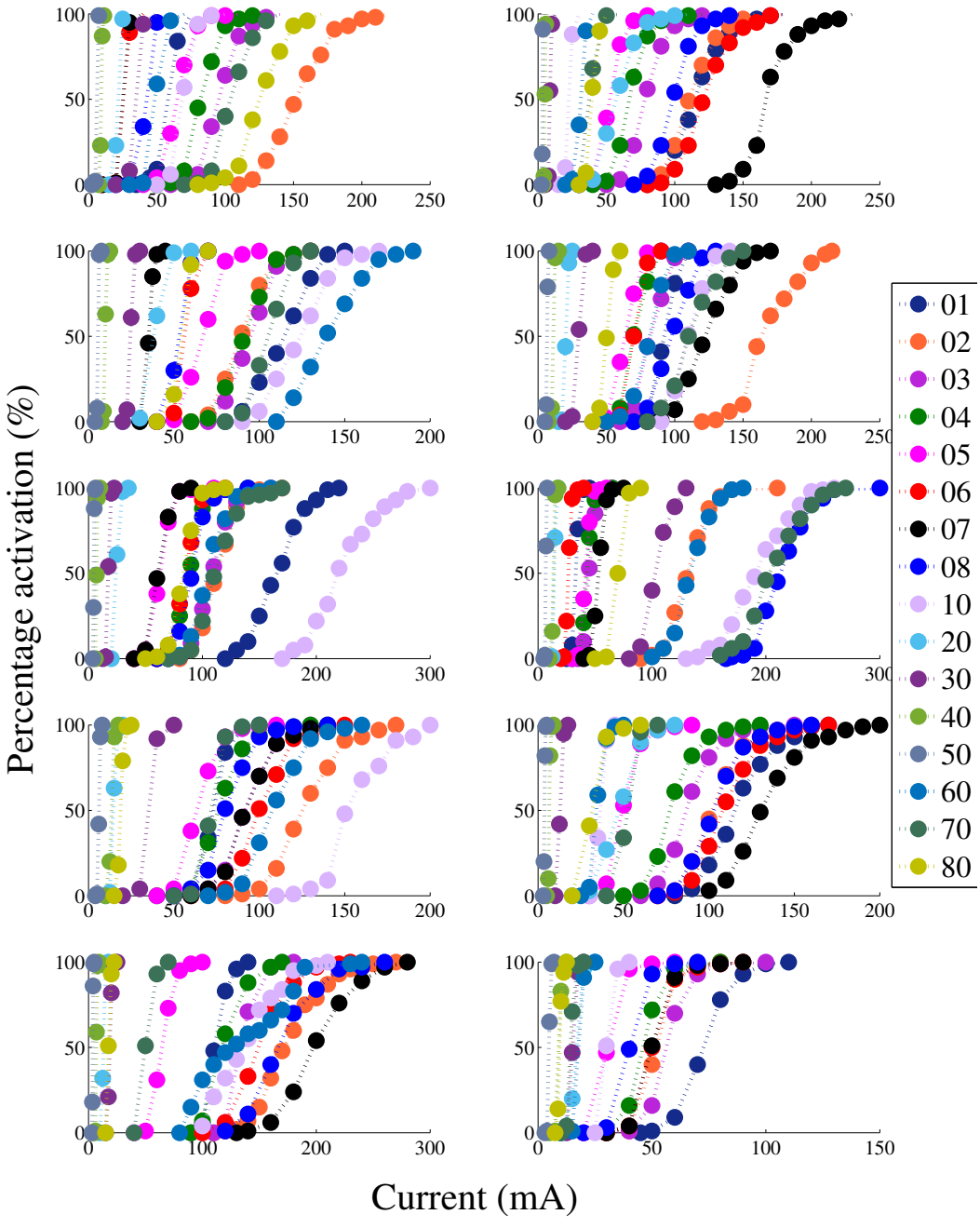

Figure 3.20: PA versus amplitude of a 200 μs pulse for all the variations of the nerve and for all the configurations. Figure adapted from [70] with changes.

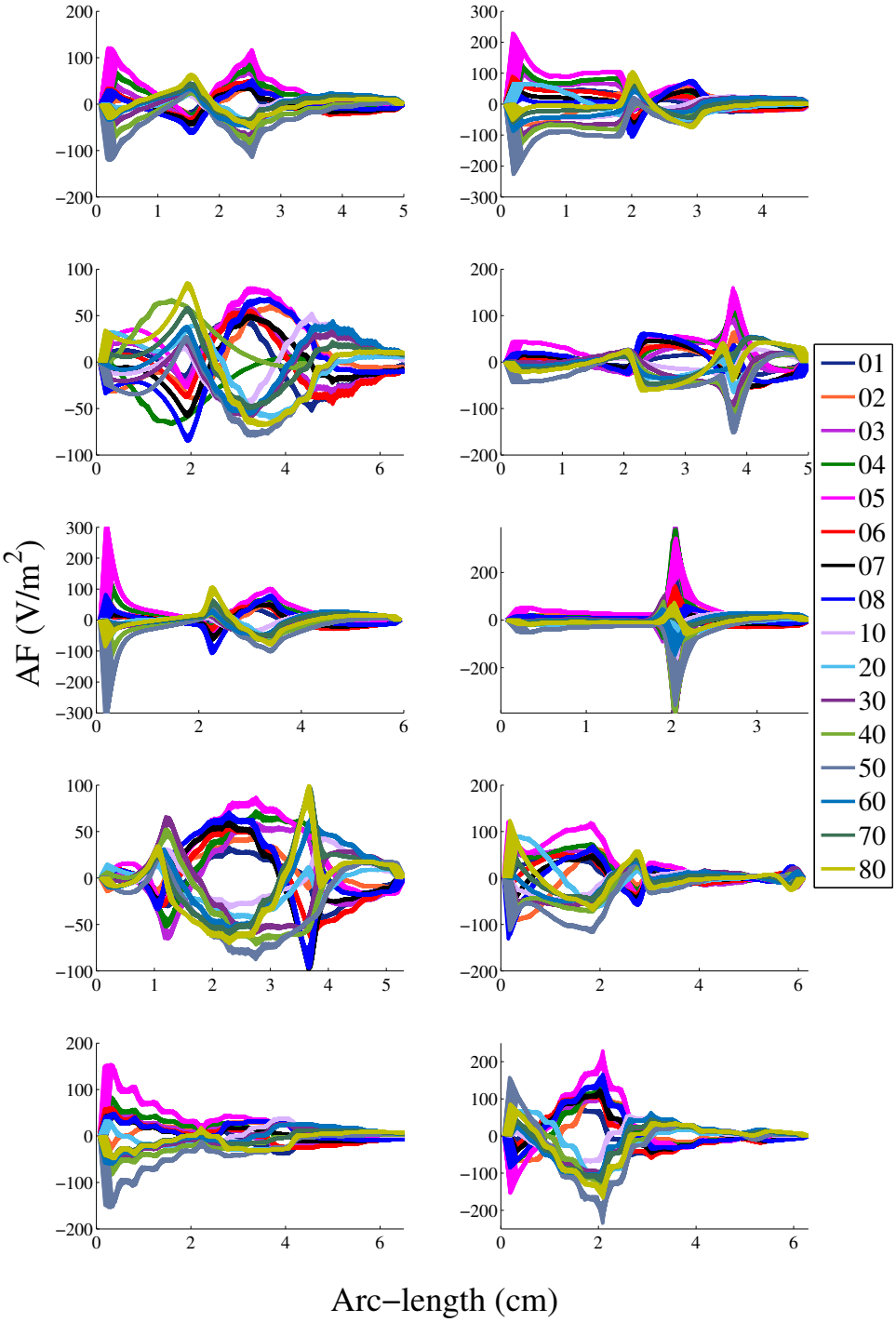

Figure 3.21: AF plots for all configurations and for all the variations of the nerve.

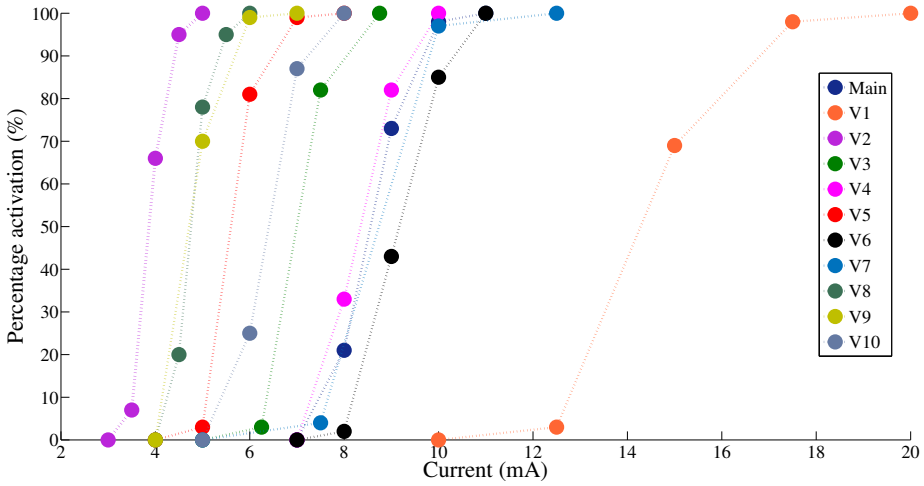

Figure 3.22: PA versus amplitude of a 200 μs current pulse for (4-5)0 configuration for all the variations. Figure adapted from [70].

configuration referred to as (4-5)0, Figure 3.22 shows the PA versus the amplitude of current for the said configuration for all the variations including the original. As predicted, the level of the applied current remains relatively the same for the tripolar configurations formed by merging the two bipolar configurations yielding similarly low thresholds. Only in the case of V1 has it increased slightly. The result is of significance in terms of the clinical trial of a multi-electrode device, the minimisation of the number of electrodes and the relative movement of the device as will be addressed in the Discussion Section.

3.4.6 Charge density

Figures 3.23 and 3.24 show the charge per area per phase along the diameter of 0 electrode and along the main trajectory of the nerve, respectively, for a 200 μs pulse using configuration 50, for different amplitudes. The well-known effect of having higher current densities at the edges of the electrode due to the equipotential surface of the electrode is observed. The results of both figures are of significance in safety considerations regarding the solution as will be discussed in the subsequent section.

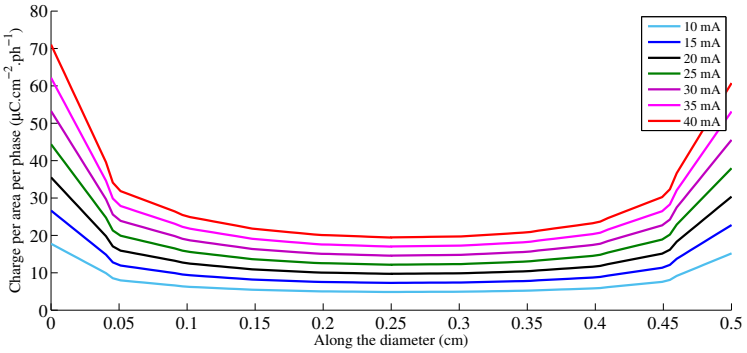

Figure 3.23: Charge per area per phase along 0 electrode diameter for a 200 μs pulse of different amplitudes using configuration 50. Clearly, current density is considerably higher at the edges of the electrode.

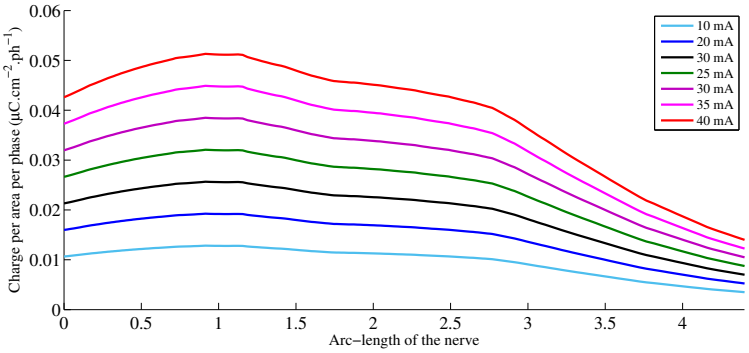

Figure 3.24: Charge per area per phase along the pudendal nerve for a 200 μs pulse of different amplitudes using configuration 50.

3.5 Discussion

Other studies based on computational models of the intraurethral electrical stimulation of the pudendal nerve with different electrode sizes and shapes [27] and using a cuff multi-electrode on the proximal pudendal nerve trunk [85] have investigated the possibility of achieving selectivity and reducing the activation threshold. However, no such study has investigated the dynamics of neural activation for the trans-rectal stimulation of the pudendal nerve as presented here. It was established that models are powerful tools in the design of neural prosthesis. It was discussed that hybrid models are the ones in which the extracellular potential field is found in a volume conductor model which is then used as the boundary condition in a cable model of the fibres. Based on the review given, hybrid models were proven to be powerful tools in the design of the neural prosthesis.

The two elements of the model, the volume conductor and cable model, were formed based on human data. The MRI study established a realistic approximation of the trajectory of the nerve and anatomical features while the conductivities of the inhomogeneous media were defined based on well-established data in the literature and human experiments. The validity of the volume conductor model, in terms of the boundary conditions and discretisation level, was scrupulously verified to ensure the model is a valid representation of the target structure. The MRG cable model was used as a powerful model based on mammalian fibre data which has been verified to yield reliable results by various contributions in the literature. Also, the validity of the model for the transcutaneous stimulation has been confirmed by Kuhn *et al.* [107]. A normal distribution of the fibre diameter based on the available information in the literature and, consequently, different physiological parameters were used to model a nerve. Experimental physiological parameters were linearly interpolated with respect to the fibre diameter to derive the values for any arbitrary fibre diameter. Given the relatively narrow distribution and that enough experimental data were available the interpolation

approximation was deemed to be valid. It was verified that ignoring the spatial distribution of the fibres in the nerve and different fascicles do not affect the outcome of the study but significantly reduce the the simulation run time and the model complexity. Note that the dimensional ratio is very large if one is to consider the EP, PE, and EN tissue layers and the corresponding spatial variations result in extremely long simulation times. Given that this work is essentially an optimisation study, such simplifications are essential but it should have been verified up to what extent they might have affected the outcome as was done here.
The AF and dynamic response of the nerve were investigated for various electrode configurations. Understandably, the number of configurations possible is limited by the shape and size of the device. Electrodes of the same size (5 mm diameter) were mounted on a slightly modified design. The electrode size was not a feature of this study but merely a practical choice based on manufacturability. Reducing the size of the electrodes increases the current density and may reduce the threshold but a relatively large size was chosen for an improved contact and a reduced charge density.
Having developed a method to minimise the number of configurations, in the first iteration 13 electrodes were used but it was shown that four of the electrodes may have been removed without reducing the degrees of freedom in the design. A spectrum of the required current levels was observed, spanning above 150 mA. Although the load driven by different configurations may be slightly different (i.e., the voltage drop across the electrodes may be slightly different), but this variation is not significant compared to the difference in the voltage drop across the electrodes when the applied current varies from about 10 mA to 150 mA. Furthermore, the difference between the minimum and maximum required current levels are much larger than the errors caused by the approximations. This indicated a real possibility of improving the solution considerably. An interesting feature of this study is that the anode is placed closer to the nerve compared to the cathode when the lowest threshold is observed. This may be counter-intuitive

as the stimulation is generally near cathodes. However, it is important to note that there is about 2 cm distance between the closest electrode and the nerve. Thus, the general controlled assumptions such as those in implants are not valid and indeed this shows the significance of the model. A great improvement compared to the original design was achieved. However, it was crucial to consider the variations of the trajectory of the nerve as indicated in the literature and the movement of the nerve in different body postures.

The ensemble of the 10 anatomically possible and probable nerve trajectories formed, proved to be a powerful tool in investigating the effect of variations in the trajectory. The same two configurations (i.e., 40 and 50) yield a considerably lower threshold for all of the variations. This can reduce the system complexity considerably. If different configurations had been shown to be the optimal configurations in different variations, a multi-electrode reconfigurable stimulator would have been required. Given the variation of the nerve trajectory in different body postures, this would have also affected the efficacy of the solution. This is a greatly convenient outcome.

The other interesting outcome of this study was that it was shown that a tripolar configuration formed by merging the two bipolar configurations yielding similarly low thresholds would yield an equally low threshold. This was associated with the fact that the position of the depolarisation was in the same place along the nerve. Although this locally reduces the current density on a single electrode and may increase the threshold but it has been shown that it reduces the current spread. Also, as two paths are provided for the stimulus current, the maximum voltage compliance is reduced in this case. So, the fact that the given bipolar configurations depolarise the same location along the nerve means that their merger does not *dilute* the field and the benefits of using a tripolar configuration are also achieved.

This also has a significant benefit in a clinical test setting. If a multi-electrode configuration is used, finding a tripolar configuration which yields similar thresh-

olds is straight forward by merging the best bipolar ones. This establishes a very specific test protocol.

The fact that the most desirable electrodes are next to each other is convenient as this shows that slight movement of the device does not affect the efficacy of the solution. An electrode may be placed midway between the space both electrodes cover. Therefore, a very specific suggestion may be produced as a result of the study presented in this chapter. The anode should be placed on the apex of the thicker side of the device, pushing towards the pudendal nerve, while the cathode should be placed caudally, looking towards the organs when inserted.

The amount of the charge per area per phase along the nerve is on the safe side of the limit for a safe charge injection into the nerve [146]. However, the injected charge per area per phase observed based on the simulations on the anode shows the significance of reducing the stimulus current as attempted in this chapter.

A complete description of the electro-chemistry of the charge injection through electrodes may be found elsewhere [147] but a summary is mentioned here. As an electrode is put into contact with an electrolyte (human tissue) a potential develops which is primarily governed by the Nernst formulation and is referred to as the equilibrium potential of the electrode. As the current is injected through the electrode, the current initially charges the double-layer capacitance. The potential of the electrode rises above the equilibrium, at which time the potential dependent reversible and irreversible Faradaic processes may occur. Such reactions are dependent on the fastness of the kinetics of the said reactions and the speed of the mass transport. A kinetically fast process with respect to the mass transport, requires a small over-potential, defined as the variation of the electrode potential from its equilibrium potential, to lead to a significant amount of current flowing. As the reactants, consequently, do not move away from the surface, applying current in the reversed direction may force the reactions to be reversed (i.e., biphasic charge balanced stimulation). Kinetically slower reactions are limited by the mass transport. Thus, the reactants move away from the surface

as the reactions occur at higher over-potentials. These reactions are referred to as the irreversible Faradaic processes while the former result in the adsorption of charges to the surface and are reversible. One of these irreversible processes is the electrolysis of water. This may happen above and below a certain positive and negative potential, respectively, for a given electrode material. The range of the potential below these limits (safe limits) is referred to as the water window. The electrolysis of water results in pH changes and gas formation. The dissolution and depassivation of the metal at the surface are other common damages [147]. Therefore, it is important that even if a charge balancing paradigm is followed, the injected charge within a phase is in the safe limits.

Safe charge injection limits for stainless steel are about 40-50 $\frac{\mu C}{cm^2}$ per phase [148]. Therefore, the minimisation of the stimulus current was necessary as proposed in this chapter as stainless steel electrodes are selected at this stage of the development due to their availability and mechanical properties.

It should be noted that the electrode material forms a very important feature of the design. The safe limits of the charge injection, as mentioned for stainless steel, and the general electrical properties of the electrode should be taken into account. Under most neural stimulation conditions, the Faradaic processes dominate [149]. Thus, it is important to ensure a given material can safely deliver the required charge. At this stage of the design, given the optimisation work presented in this chapter, stainless steel theoretically can safely deliver the required charge. However, after the clinical tests in which the average amplitude of the required stimulus is ascertained, if the required current is proven to be higher than safe limits, other choices of material may be considered.

3.6 Summary

A thorough theoretical review of the nerve and volume conductor modelling was given. Starting from the fundamentals of the HH type neural tissue models, the

general concepts of the cable theory were discussed. The chronological and conceptual development of different cable models of the neural tissue especially that of a myelinated fibre were reviewed. Then, the fundamentals of volume conductor models, in terms of the underpinning equations solved and their approximations, the choice of the boundary conditions and the way they are solved numerically were discussed. Focusing on the main topic of this chapter, different methods of simulating the extracellular stimulation were put forth. Namely, the AF concept and the hybrid models which are used in this study were discussed. A summary of key contributions in the use of hybrid models were presented with the focus on the methods used. This concluded the theoretical review in this chapter.

To remind the reader of the objective of this chapter, the models were developed to investigate if the stimulus current delivered by the trans-rectal stimulator could be minimised. Thus, a valid volume conductor model in tandem with a model of the nerve should have been used. An MRI study was performed on a male volunteer to get an approximate trajectory of the nerve and to form a 3D understanding of different anatomical features around the device *in situ*. After forming a 3D model of the pelvic region and the device, based on experimental measurements and the existing data in the literature the conductivity of different layers of the model were set. Through a rigorous iterative method, the validity of the boundary conditions used, the model formation and discretisation methods were tested and verified. With tested methods in the literature, a cable nerve model was developed comprising random positions and fibre diameter distributions. The approximations in the hybrid model, namely the exclusion of the nerve fascicle tissue layers were investigated as to how much they affected the results.

In the first iteration, a modified design with a multitude of electrodes was developed. The electrode closest to the nerve was used in all the configurations which were tested. The number of the electrodes in the first iteration was reduced by omitting those which would not limit the degrees of freedom in the design and yielded a similar response when compared to another electrode. In the second

iteration, for all the possible bipolar configurations, the PA versus the required current was simulated. In addition, the AF for the random populations of the fibres for all the bipolar configurations were calculated. At this stage two configurations requiring a considerably lower current amplitude was identified.
Given that the course of the nerve may vary amongst different individuals or in the same individual in different body postures, a method of generating a possible and probable ensemble of trajectories was developed. After generating ten different trajectories, a model of the nerve was formed in each case and the PA versus the required current for all the bipolar configurations was simulated. It was verified that even when considering the variations of the nerve trajectory, the same two configurations yielded considerably lower thresholds. In such configurations, the anode should be placed close to the nerve on the device while the cathode should be placed caudally. Furthermore, it was shown that in this case the tripolar configuration formed by merging the two desirable bipolar configurations yields an equally desirable response.

The outcome of this study is very significant as this may essentially render the trans-rectal neuromodulation of the pudendal nerve a viable solution for the chronic use as the most limiting factor previously stated in the literature is the high level of the current required.

Chapter 4

SEMG Compartment Design

4.1 Introduction

The EMG is the study of muscular tissues by recording and analysing the electrical signal travelling along muscle fibres. A comprehensive historical review of the way the EMG concept and apparatus evolved to become a viable solution in the early days of the study of the muscle activity is presented in [150]. The aim of this chapter is to demonstrate the theoretical and experimental evidence for a practical and optimized design of the recording apparatus for the conditional trans-rectal neuromodulator whose stimulation compartment was optimised in Chapter 3.

After a brief physiologic description of muscular structures, the theoretical basis of the design is presented. The subsequent sections of this chapter present the materials and methods regarding the experiments, results and the ensuing discussions.

4.2 Theoretical review

4.2.1 Muscle types

The three major types of muscles are smooth, cardiac and striated [150]. The smooth type was mentioned in relation to the detrusor, the smooth muscle of the urinary bladder. This type is generally characterised as the muscle with an involuntary control for the contractility of hollow organs [150]. The smooth muscle can also be found in the walls of blood vessels, the uterus and various tracts in the body [151]. Namely, they can be found in reproductive, gastrointestinal and respiratory tracts. Smooth muscles lack the cross-striation, hence the name. A smooth muscle fibre's diameter ranges between 2 μm to 10 μm [151]. This type of muscle is generally classified as either single or multi-unit.

Unlike smooth and cardiac muscles, the latter of which is only found in the heart, striated or skeletal muscles are generally controlled voluntarily. As the target muscle (i.e., EAS) from which the EMG signal is recorded in the device described in this thesis is of the striated type, this type of muscle is described in more detail in the following section.

4.2.2 Striated muscles

The structural unit of the striated (skeletal) muscle is the muscle fibre. Muscle fibres can have a length ranging from a few millimetres to 30 cm [150]. They have a diameter ranging from 10 μm to 100 μm [151]. A small group of muscle fibres is supplied by the terminal branches of a motor fibre. Functionally, the skeletal muscle is composed of two sets of muscles fibres: extrafusal muscle fibres which result in the actual motion and intrafusal fibres in the form of a spindle, engulfed by extrafusal fibres. Muscle spindles are the receptors through which afferents receive the sensory information, acting as proprioceptors [151].

Three types of lower motor neurons innervate striated muscle fibres. The α-

motoneuron supplies extrafusal fibres, the β-motoneuron innervates both extrafusal and intrafusal fibres and the γ-motoneuron supplies only intrafusal fibres. The motoneuron innervation of muscle spindles generally controls their sensory responses. The cell body of the α-motoneuron, the nerve fibre and its terminal branches and the group of the fibres innervated by the said motor neuron constitute a motor unit (MU) which poses as the functional unit of the motor system. Upon the arrival of an AP to the neuromuscular junctions of an MU, all of the fibres contract almost simultaneously and may be shortening to about 57% [150] of their resting length depending on the type of the contraction as will be discussed later. The innervation zones (IZ) have been shown to be usually located in the middle of the fibres in the human and other species [151]. The number of fibres controlled by a single MU has been shown to depend on how fine the required movement is. For finer movements the said number has been shown to be usually smaller [150]. The number of MUs per muscle in humans range from 100 to 1000 [151]. Based on the speed of contractions and fatigability, three types of MUs are identified: the slow twitch (S or I), the fast-twitch and fatigue-resistant (FR or IIa) and the fast-twitch and fatigable (FF or IIb). Type I MUs are resistant to fatigue [150].

One of central features regarding the striated muscle recruitment is the force generated due to activities of a muscle. The force is modulated by the number of MUs recruited and their recruitment frequency. The level of the force generated is proportional to these factors and is in the range of 20 to 50 $\frac{N}{cm^2}$ [151]. These factors (i.e., the number of recruited MUs and their discharge frequency) also determine the electrical activity of the muscle. Therefore, considering a relationship between the EMG signal and force is plausible.

Before further analysis of the EMG signal and the corresponding muscular activity, an important note on various muscle activation scenarios should be mentioned. Although generally referred to as muscle contraction, this can be considered as a misnomer as contraction may imply shortening. There are three types of muscle

contractions: the concentric contraction in which muscle shortens, the eccentric contraction which leads to the muscle lengthening and the isometric contraction for which the muscle length remains constant. These scenarios occur due to the MU activity but there is also a scenario in which the muscle passively stretches [152].

4.2.3 Electrical activity of a muscle

The underlying phenomena that result in electrical activities in a muscle and consequently lead to the generation of the EMG signal can be explained using HH models as used for neurons in Chapter 3. The membrane cell of a muscle cell is more complex than a neuron. Namely, this is due to the existence of a network of branching tubules radially penetrating into the fibres, providing radial pathways for current [151]. As a first order approximation, however, HH type models have been shown to model electrical properties of the muscle. Thus, the propagation of the AP along the fibre and its excitability can be explained following the same principles. The AP is generated at the IZ, travels along the sarcolemma (muscle fibre membrane) and extincts at the extinction zone (EZ) (tendons). The time trace of the AP follows the same morphology as described in the case of the AP in neurons. The physiological range of the CV in a muscle fibre is between 2 $\frac{m}{s}$ to 5 $\frac{m}{s}$ [151, 153, 154].

The EMG signal, recorded either intramuscularly or by surface electrodes of different configurations, is essentially due to the electric field formed as the result of the AP generation and propagation. Wire or needle electrodes can penetrate the muscular tissue to effectively show the transmembrane potential. The recording area of such methods is focused and can be readily used to analyse the AP due to a single MU [151]. Understandably, such methods are not suited for the target application of this thesis due to their intrusive nature. Thus, in the subsequent sections of this chapter only the SEMG is considered. Using surface electrodes, fields can be recorded after they travel along a volume conductor. Depending on

the way surface electrodes are arranged and the linear operation performed on the signals recorded from different sites, the recorded EMG signal varies. Although the design of the SEMG apparatus for the acquisition of an adequate EMG signal may be more challenging but their non-invasive nature makes them more attractive for an application such as the one mentioned here. In the following section the underlying concepts of the SEMG recording are addressed.

4.2.4 Recording SEMG

The surface recording refers to a situation in which at least one electrode of a certain area is placed on the surface of the body at a distance away from the target muscle. Firstly, it is important to realise what the nature of the signal being recorded is. For an intuitive and relatively simple understanding of the SEMG signal, one can consider the induced tripolar field due to the AP propagation as the main source. This concept was mentioned in Chapter 2 when the propagation of the AP was discussed. As the ion concentration in and around the fibre is perturbed, an electrical field is induced, as shown in Figure 4.1, and intracellular and extracellular currents flow. The resulting tripole travels along the fibre as the AP propagates. The said field due to the momentary extracellular current can then propagate extracellularly in the volume conductor in a manner modelled by Maxwell's equations, also partly revisited in Figure 4.1. It has been shown that the overall effect of the volume conductor is a low-pass filtering of the propagating field [151]. This low-pass effect is a function of the distance of the recording assembly from target MUs.

4.2.5 Simulating SEMG

Finding the right parameters in designing the recording apparatus for the SEMG signal has been intertwined with modelling attempts presented in the literature aimed at simulating this signal [155–182]. Such studies generally endeavour to explore the effect of physiological and experimental factors on the recorded sig-

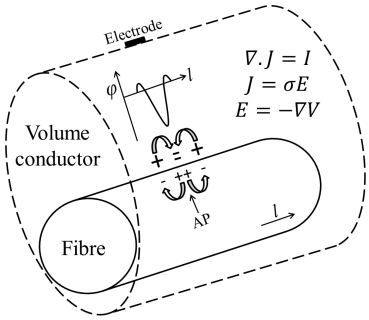

Figure 4.1: The schematic of an extracellular recording. Figure shows the induced tripole due to the generation and propagation of the AP and some Maxwell's equations governing the propagation of the induced field. The schematic is not to scale.

nal. Namely, the number of MUs [163], their spatial distribution [157, 161, 162], their firing rate [169], the number of fibres in each MU [164], their diameter distribution and their length [157] as well as the properties of the multilayer volume conductor [164–166] and the exact shape of intracellular APs [157] are some of the physiological factors.

In addition, the spatial configuration [164, 166], position [162, 177], shape [161] and size [167] of electrodes, spatial and temporal sampling frequencies [166], signal conditioning and the nature of operations performed on the recorded signal [158, 160] constitute the experimental features of interest.

It should be noted that an AP due to an MU (MUAP) is the summation of spatially and temporally dispersed APs of individual muscle fibres in a given MU. The AP of an individual fibre can be expressed using the convolution of the transmembrane current and a weight function. The weighting function can be thought of as the impulse response of the volume conductor. Heuristic and functional methods provide the alternatives to the actual solution of the partial differential equations, governing wave propagation in the said volume conductor for which the quasi-static approximation can be used [174]. As mentioned, the volume conductor has different layers, some of which have anisotropic properties. The starting point in a modelling attempt can be to use an analytic expression for

the spatial distribution of intracellular potential due to an AP for a single fibre at a given point such as the one shown in Equation (4.1) [182] as a modified Rosenfalck expression [183]. Variations of this model have been implemented in several contributions with adjusted coefficients (i.e., A, B and C) [157, 162, 174, 182] depending on the best fit for experimental measurements.

$$V(z,t) = Az^3 e^{-Bz} - C \tag{4.1}$$

where z is the axis along the fibre in question. The transmembrane current due to this perturbation can then be calculated based on core conductor model using Equation (4.2) [182,184] in which the transmembrane current per unit membrane area is approximated by merely knowing the intracellular spatial distribution of potential:

$$J(z) = \frac{\sigma_i a}{4} \frac{\partial^2 V(z,t)}{\partial z^2} \tag{4.2}$$

where σ_i is the intracellular conductivity and a is the fibre diameter. Similar to the methods used to calculate the transmembrane current of a nerve fibre, it is possible to computationally solve the current due to all the channels involved and arrive at a numerical solution for the transmembrane current. However, the focus here is only to develop an intuitive understanding of the underlying processes, thus, the analytic approximations should suffice. For a given time (t) Equation (4.2) can be thought of as an n pole source, where n is the sampling frequency along the z direction.

Using a cylindrical coordinate, the electric potential φ produced by the extracellular current along the fibre can be found by integrating the sources at z_o positions as shown in Equation (4.3) using Green's theorem and a line source approximation [182, 184]:

$$\varphi(r,z) = \frac{2}{4\pi\sigma_r} \int \frac{2\pi a J(z_o)}{\sqrt{\frac{\sigma_z}{\sigma_r} r^2 + (z - z_o)^2}} dz_o \tag{4.3}$$

where r and z are the radial and axial separations, respectively, and σ_r and σ_z are the corresponding conductivity values, radial and in the direction of the fibre, respectively. These analytic expressions provide the basic tools for the analysis and modelling of the recorded field due to a fibre at the surface in the majority of key initial efforts on EMG modelling. This simple model can then be enhanced to become more realistic.

The first point of improvement is the incorporation of a multi-layer anisotropic volume conductor. The skin, fat and muscle layers may be incorporated in the volume conductor. Analytically, the approximation of Maxwell's equation as shown in Equation (4.4) [166] and described in detail in Chapter 3 may be used to solve the potential at every layer. The boundary conditions enforced are as follow: the orthogonal component of the current in layer boundaries is continuous, the parallel component of the electric field is continuous at the boundary and the field diminishes to zero at infinity [166].

$$-\nabla\sigma(x,y,z)\nabla.\varphi(x,y,z) = I \tag{4.4}$$

Analytic solutions can be found by considering every layer as a system with a specific impulse response. Then, the convolution of an input with the impulse response of the first stage and, consequently, the convolution of the output of the first stage with the impulse response of the second layer can produce the input to the third layer. The process may be simplified by solving the problem in the spatial frequency domain and indeed the majority of the subsequent analyses are presented as such.

After arriving at a more realistic volume conductor model, one should develop a realistic model of the signal generated at fibre and consequently MU levels. As a source current is generated at an end-plate it travels on either direction and the generated source sinks in tendons. Thus, the progressive generation and extinction of the source should be incorporated in the model [165, 174]. Therefore,

the finite sizes of the volume conductor and fibre should be considered. The next stage in having a more complete model is to have an ensemble of fibres with a stochastic distribution of their diameters in a realistic geometrical distribution. The variability of the diameter of the fibres leads to the variability of their conduction velocity which leads to a temporal dispersion. Also, if fibres are oriented along different directions, fibre pinnation should be accounted for [185]. More realistic analytic models to predict the behaviour of MUAPs should consider the morphological variability of IZ and EZ locations. These can be modelled by subjecting the MUAPs to the same temporal dispersion caused by these variations due to the width of the IZ. The variability of neural transmission has a less pronounced effect on the observed dispersions. Thus, it may be ignored in the model. On the other hand, a feature which may be of significance depending on the application is the firing frequency parameter of MUs [151].

Considering the additive noise $v(nT_s)$, the recorded SEMG at a specific point may be found using Equation (4.5) [163]:

$$SEMG[n] = \sum_{i=1}^{M} \sum_{k=-\infty}^{+\infty} \varphi_{ik}(nT_s - \Phi_{i,k}) + v(nT_s) \tag{4.5}$$

where T_s is the sampling period, M is the number of MUs, i is the number of MUAPs in the signal due to ith MU, φ_{ik} is the kth MUAP in the signal due to the ith MU, $\Phi_{i,k}$ is a random variable representing the occurrence time of φ_{ik} and v is the added noise. This model will be revisited when the amplitude estimation of SEMG signals is mentioned. This way a robust model of the SEMG can be developed.

Considering the complex models developed, a systematic understanding of this physiological phenomenon is built. Apart from this, the conclusions drawn in terms of design specifications based on these models are of particular interest. In deriving design strategies in this chapter, when a modelling conclusion is used, experimental results are used to corroborate or complement them.

From a single point recording, it is possible to derive the underlying expressions for different spatial filtering paradigms and for different shapes of electrodes. The following addresses these points.

4.2.6 Multi-point recording

Features such as electrodes' material, physical properties (i.e., shape and size), position, quantity, and the linear operation performed on the detected signal recorded from the electrodes constitute the most important elements in designing an SEMG acquisition electrode assembly. Understandably, these design parameters are affected by the nature of the recorded signal. The electrode material primarily affects the electrode tissue interface as will be described in this chapter. The effects of physical properties of an electrode can be perceived based on the information provided so far. After a field is produced, it propagates in the volume conductor and arrives at the surface of the skin. A metallic surface, as an equipotential surface, can be thought of as a spatial averaging filter. Considering infinitesimally spaced recording points below the metallic surface on the outer boundary of the skin, the effect of the metallic electrode is similar to averaging the value of the field in all the mentioned points. Although it is dependent on the electrode shape and fibre orientation, a relationship between the spatial frequency and the temporal frequency can be achieved which implies similar filtering effects in time. The equipotential surface of the electrode may also modify the field in the vicinity of the skin which was not mentioned in the intuitive picture drawn above.

For the exact cut-off frequencies and the frequency response of different electrode shapes, a more elaborate analysis is required. Before the effect of the electrode shape is considered analytically in the next section, the transfer function of an array of point electrodes is discussed. The notation can then be used to derive the transfer function of any shape of recording electrodes. Considering an array of point electrodes similar to the one shown in Figure 4.2 in two dimensions, it

is possible to derive analytical expressions for a system of recording electrodes and by extension for different shapes of electrodes. The impulse response of the

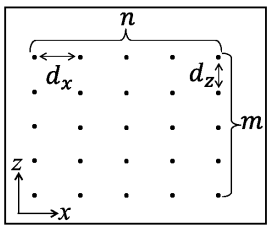

Figure 4.2: The schematic of n by m recording points. The array is placed on the surface of the skin on the xz plane. The idea can be expanded to derive the expressions for the frequency response of electrodes of any shape as well as any array.

system shown in Figure 4.2, $h(x, z)$, can be shown analytically as in Equation (4.6) [151, 161]:

$$h(x,z) = \sum_{i=1}^{n}\sum_{r=1}^{m} w_{ir}\delta(x - i \times d_x)\delta(z - r \times d_z). \tag{4.6}$$

where $w_i r$ is a vector containing the weighting coefficients associated with every recording point and $\delta(.)$ is a Dirac delta function. Consequently, the transfer function of the array, $H(k_x, k_z)$, in terms of the corresponding spatial wave numbers, k, can be calculated as shown in Equation (4.7) [161]:

$$H(k_x,k_z) = \iint h(x,z)e^{-jk_x x}e^{-jk_z z}dxdz = \sum_{i=1}^{n}\sum_{r=1}^{m} w_{ir}e^{-jk_x id_x}e^{-jk_z r d_z} \tag{4.7}$$

Two widely used linear recording configurations, single differential (SD) and double differential (DD), and the corresponding transfer functions are shown in Figure 4.3 [151]. Assuming that the direction of propagation is along the x axis as shown in Figure 4.3, the spatial frequency (f_x) is related to the temporal frequency (f) based on the CV (ν) [161]:

$$f = f_x \nu. \tag{4.8}$$

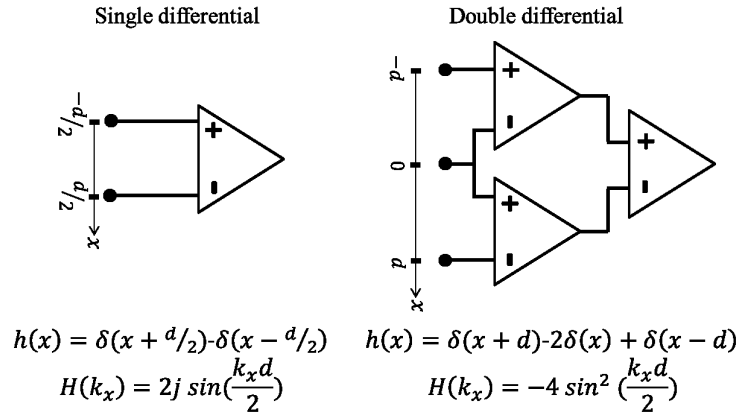

Figure 4.3: Impulse responses and transfer functions of SD and DD configurations. Similar to the paradigm mentioned in the text, considering the electrode spacing the impulse response of a recording system may be derived. Figure redrawn and altered from [151].

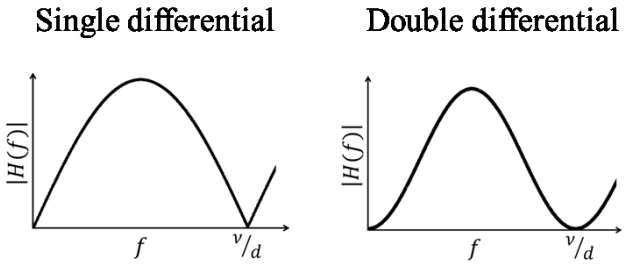

Figure 4.4: Linear plot of the frequency response of the SD and DD configurations. The shape of the frequency response is of great significance in understanding the underlying filtering effects imposed by any array operation. Figure redrawn and altered from [151].

Subsequently, the spatial transfer functions shown in Figure 4.3 can be transformed and plotted as shown in Figure 4.4. The significance of the inter-electrode spacing (IES) should be clear from the frequency responses. Apart from a frequency modification, the IES can change the depth of recordings as well. For instance, as the electrodes are placed further apart in a single differential recording, the depth of the recording increases. This has been formulated empirically by showing the relationship between the recorded signal (V) and the IES as shown in Equation (4.9) [186]:

$$V = \frac{V_o}{(\frac{r}{r_o})^D} \tag{4.9}$$

where V_o and r_o are constants, the latter of which is related to the distance from the centre of an MU, D is a function of the IES and r is the separation parameter. the quantification of the values in Equation 4.9 has been attempted in the literature. It has been demonstrated that for a large IES it may be possible to increase the contribution of further away MUs but a small IES does not necessarily focus the recording on superficial MUs. Other methods for focusing the field, including the use of the DD configuration, may reduce the recording volume.

4.2.7 Electrode shape

Considering that d_x and d_z tend to zero while n and m tend to infinity in Equation (4.7), for a given shape and size of an electrode, it is possible to derive the electrode transfer function $H_e(k_x, k_z)$ by performing a two dimensional integration across the area of the electrode, A, as shown in Equation (4.10) [161, 175]:

$$H_e(k_x, k_z) = \frac{1}{S} \iint_A e^{-jk_x x} e^{-jk_z z} dx dz \tag{4.10}$$

in which a weighting operation is implied in the averaging effect which was explained earlier. It has been shown that using Equation (4.10) the transfer function of rectangular and circular electrodes can be analytically derived. It has been shown that for rectangular electrodes of dimensions $(a \times b)$ the spatial transfer function is as follows [161]:

$$H_e = sinc(\frac{ak_x}{2\pi}) sinc(\frac{bk_z}{2\pi}). \tag{4.11}$$

Further, for a circular electrode of radius r, the spatial transfer function can be shown as in Equation (4.12) [161].

$$H_e = \frac{2J_1(r\sqrt{k_x^2 + k_z^2})}{r\sqrt{k_x^2 + k_z^2}} \tag{4.12}$$

where $J_1(.)$ is the Bessel function of the first kind and first order.
In the case of a rectangular electrode, depending on the direction of propagation, it is possible to use Equation (4.8) to calculate the temporal frequency modifications due to the electrode. However, this relationship is not valid for a circular electrode but numerical solutions have been presented in the literature [161].

4.2.8 Electrode array

It is possible to arrive at a general expression in which the effects of electrode and array operations are considered as follows:

$$H_s(k_x, k_z) = H_e^{ir}(k_x, k_z) \sum_{i=1}^{n} \sum_{r=1}^{m} w_{ir} e^{-jk_x i d_x} e^{-jk_z r d_z}. \tag{4.13}$$

Given the expressions provided above, it is possible to calculate the transfer function of any electrode system including a linear or two-dimensional array of circular or rectangular electrodes. A desired recording assembly should with high fidelity approximate or estimate the corresponding intracellular recording. Understandably, due to practical reasons in recording, such as the contamination of the desired signal with unwanted ones, at least two electrodes are used in recording SEMG apart from the reference electrode. Therefore, understanding arrays is of significance in the context of SEMG recordings.
The issue of the spatial sampling was touched upon when the SD and DD configurations were compared, in which cases a linear array of two and three electrodes are used, respectively. The spatial resolution of the SEMG is limited. An SEMG recording assembly with relatively large electrodes may be incapable of distinguishing the activities of different MUs within a muscle as the SEMG signal is the summation of contributions from different MUs within the volume of detection. In a more drastic situation, the cross-talk between SEMGs recorded from different muscles may contaminate the recorded signal. Depending on the application of the acquired SEMG signal, the issue of the spatial resolution should be

designed with care. Although in the target application in this thesis no such fine characterisations are required, the design of the sensor for the target application relies on the data derived from such fine characterisations of the EAS. Namely, the positions of the IZs and EZs, which are crucial in positioning the electrodes, require a high resolution array to be located. Also the CV of the MUAP is important as it directly affects the required electrode spacing and size.

Understandably, more datum entities may contribute to having more degrees of freedom and consequently the ability of drawing more specific conclusions. The SEMG by default reduces data due to the low-pass effect of the volume conductor. Overall, any array from the one formed of two electrodes to high density arrays should be thought of as spatial filters. For instance, it has been shown that by assigning specific weightings to the electrodes in a two dimensional array of electrodes, it may be possible to reverse the effect of the isotropic layer beneath the recording site [164]. In addition, the depth-dependent low-pass filtering of a volume conductor can be used to only record superficial sources by forming two-dimensional filters to selectively target specific sources. This process is referred to as de-blurring [166]. Also, it has been shown that arrays may be used to make the recording assembly impervious to slight variations of the fibre orientation and also improve the CV estimation [164]. It is worth reiterating that depending on the application, these features may be implemented.

There are various features of the recorded SEMG which may be of significance. Namely, the amplitude of the recorded signal (as will be discussed in detail), its frequency spectrum and the CV of the MUAP are of clinical significance. Apart from the general activation of a muscle, these features may be used to estimate the level of contraction, generated force [187], muscle fatigue [188], or to derive neural activity data [159]. The following sections address how different parameters regarding the electrode assembly change the recorded data. In addition, it is shown how different electrode assemblies are affected by physiological variations.

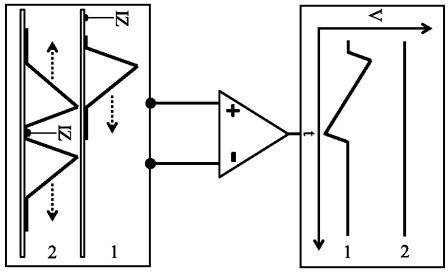

Figure 4.5: Schematic of two travelling APs and the SD recording. It is shown that the IES and the position of the recording site is of great significance. Choosing the recording site on top of the IZ may lead to diminishing signal levels.

Electrode position

If a linear array is placed in parallel with a fibre, the signal in time domain and in the parallel axis become correlated due to the relationship in Equation (4.8). The signal can be traced from the point of generation at the IZ, along its path through the fibre until it terminates at a tendon. This way, it is possible to estimate the CV of a fibre and spot the positions of the IZs and EZs. It has been shown that the recorded signal near innervation and extinction zones are substantially attenuated and this helps in finding their positions using high resolution spatial arrays.

A schematic view of the concept is demonstrated in Figure 4.5 in which the SD recording is performed. It is shown that a phase cancellation may occur if electrodes are placed around an IZ.

Also, it is important to understand what the nature of the recorded signal is. As the potential travels along a fibre, depending on the spacing between the recording poles, a signal output trace is generated. As the IES is reduced, the system becomes like a differentiator. It can be shown based on Figure 4.3 that a double differential signal with infinitesimally small IES is a second order differentiator. It should be clear now that depending on the application, the number and position of electrodes are defined. If the positions of the IZs and EZs are to be found, an array of high density electrodes should be placed along the fibre extension. At the sites that the signal is diminished the zones are located. However, if one is to find

the CV [160] or a general muscular activity and force [187], it is suggested that the electrodes should be placed between an IZ-EZ pair [177]. Farina [188] and Merletti [189] for trapezius and biceps brachii muscles, respectively, followed an approach in which by varying the IES and the electrode position while monitoring the root mean square (RMS) and mean spectral frequency (MNF) of the signal, the optimal positions of the electrodes were defined. The RMS has a dip near an innervation zone while the MNF peaks there. They estimated the position at which a premeditated variation and shift in the electrode positioning has a minimal effect on the aforementioned estimates. Although the outcome is very particular to the specific muscles they studied but the results were consistent with the rule of thumb which states that in recording, the end of fibre and end-plates should be avoided.

Electrode size, shape and spacing

Based on modelling results, it has been shown that the electrode size and shape may affect the CV estimation from the SEMG [161, 164]. However, for an application like the amplitude estimation, the effects have been discussed with respect to the reduction of noise. This will be discussed in detail later in this chapter. Other contributions [188, 189], in an attempt to standardise these design parameters [190], have defined a general guideline on the size and spacing. For instance the IES has been suggested to be about 20 mm. The indicators they used to arrive at such conclusions are generally based on the minimisation of variations and errors. However, these studies do not consider the fibre size as an input and generally generate a global design parameter which may not be accurate for smaller fibres. De Luca notes [191] that based on trial and error, 1 cm long and 1 mm wide bars separated by 1 cm reach a reliable trade off between the signal amplitude and focus. Again, this is a practical note and based on the theory and the characteristics of specific muscle fibres the design should be directed. In addition, for two electrodes and under particular conditions, such as no skin preparation,

more practical considerations and studies should be taken into account.
The application presented in this thesis is based on the detection of the level of the muscular activity. These estimations are referred to as the amplitude estimation as will be discussed in the following section.

4.2.9 Amplitude estimation

It was mentioned that the amplitude of an SEMG signal can be used as a measure of the corresponding muscular activity. On a historical note, Inman *et al.* [192], using a full-wave rectifier and an RC low pass circuit, implemented a continuous EMG amplitude estimator. In amplitude estimation terminology, this circuit comprises three system modules of: a detector, a smoothing module and a relinearisation module. The ensuing research was focused on the analysis and implementation of other non-linear modules. The mean absolute value (MAV) and RMS since then were widely implemented. Before discussing why these mathematical tools and methods are used, the stochastic nature of an EMG signal is explored based on the discussions presented in the previous sections.

Statistical nature

The analytic expression for an SEMG signal was given in Equation (4.5). If the occurrence time of MUAPs, $\Phi_{i,k}$, is considered to have a normal distribution, the frequency spectrum of the point process has been shown to be given by Equation (4.14) [169].

$$S(\omega) = \frac{1}{\mu} \frac{1 - e^{-\sigma^2\omega^2}}{1 + e^{-\sigma^2\omega^2} - 2e^{-\sigma^2\omega^2} cos(\mu\omega)} \tag{4.14}$$

where ω is the angular frequency and σ and μ are the standard deviation and mean of the inter-spike delay, respectively. This shows that the spectrum value tends to a constant value at high frequencies. Indeed, it has been demonstrated that by substituting the experimental values for μ and σ (considering mean firing rates between 8-35 Hz and a 15 % coefficient of variation of the mean inter-spike delay), the flat segment of $S(\omega)$ is reached at frequencies near 30 Hz [151]. Given

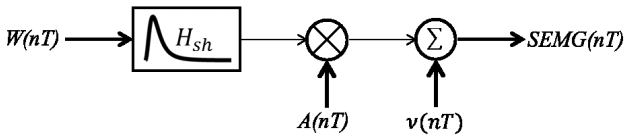

Figure 4.6: Block diagram of a functional model of SEMG. A white Gaussian noise is fed into a shaping filter, its amplitude is modulated and noise is added. Figure redrawn from [151] with changes.

the required filtering used in SEMG signal recordings, it may be concluded that the stochastic firing pattern has little effect on the frequency spectrum of the SEMG signal. This implies that the frequency spectrum of SEMG signals is essentially due the frequency characteristics of MUAPs and is affected by the CV, the position of units and the recording assembly as discussed earlier. Therefore, it is possible to introduce a functional model of the SEMG signal which is devoid of the intricacies of stochastic firing patterns [155, 158, 193, 194]. The schematic of such a model is shown in Figure 4.6 in which the spectrum of a white Gaussian noise (zero mean, wide sense stationary and correlation-ergodic) input is shaped to that of the SEMG and subsequently modulated with a given amplitude depending on the level of contraction. Various noise features can then be added for a true functional representation of the SEMG signal. The white noise input approximates the probability density function of the SEMG which is then shaped to its spectral shape and modulated by its amplitude. The shaping filter has been empirically defined by Shwedyk *et al.* [193] as in Equation (4.15):

$$H_{sh} = \frac{n f_h^4 f^2}{(f^2 + f_l^2)(f^2 + f_h^2)^2} \tag{4.15}$$

where n is a normalising coefficient and f_l and f_h are the low and high frequency controls. These values may be adjusted to define the empirically observed SEMG frequency range of about 10-500 Hz. Amplitude estimation is essentially a method in which $A(nT)$ in Figure 4.6 is defined. Mathematically, the EMG amplitude estimation is to report the standard deviation of a non-white random process

buried in noise.

Under an isometric, constant force, and non-fatiguing contraction, it is generally assumed that the EMG amplitude should be constant and this assumption defines the fidelity of the estimate. This fidelity is quantified by the dimensionless signal to noise ratio (SNR) as shown in Equation (4.16) [195]:

$$SNR = \frac{\mu}{\sigma} \tag{4.16}$$

where μ and σ are the mean and standard deviation of the amplitude estimate over a window of processed samples.

It can be shown that if the recorded samples were noise free, independent and identically distributed (IID), depending on the kind of distribution of the samples, different maximum likelihood estimates could perfectly determine the amplitude. However, as the signal is non-stationary due to its dynamic behaviour, there are sources of contamination and samples are not completely IID as will be described, it is important to consider the deviations from a perfect model in the following sections.

Signal contamination

After the acquisition of a signal, the first stage of the functional blocks of an amplitude estimator should be the one which filters the unwanted signals out. The added contamination is an impediment in an acceptable estimation of the SEMG amplitude. Thus, different forms of contamination are discussed here.

For reasons which will become clear towards the end of this chapter, as an electrode and tissue are brought into contact a half-cell potential develops. This may be in the order of 1 V. Any imbalance in the recording electrodes may manifest itself as a large differential signal at the output, completely masking the SEMG signal. It has been shown that the effects of this imbalance may be minimised by the choice of the material of the electrodes. This has been shown for stainless steel [196] and Ag-AgCl [197] electrodes which are electrically stable. For conven-

tional applications of the SEMG, skin preparations should eliminate the resulting effects [197]. However, more practical considerations should be implemented in the target application of this thesis.

An important source of contamination is the motion artefact which is mostly below 20 Hz [197]. This contamination may be due to the relative movement of an electrode and has been shown to be attenuated by recessed electrodes [197]. However, in the target application this method cannot be used as no conductive gel is applied or if applied it dries out much sooner that the span of usage. The motion artefact may be due to the relative movement of the skin and the corresponding variations in the potentials of the volume conductor. Various adaptive methods have been proposed for the elimination of this artefact [198–200]. The major motivation for not simply filtering out the artefact is that the major amplitude components of the SEMG signal may be eliminated. This may have consequences in specific applications but the muscle activation may be still visible [201]. The other motion artefact is due to the cable movement and the subsequent coupling of electromagnetic waves whose major components may range up to 50 Hz [197] for an EMG signal. Simply shielding cables does not eliminate this source [202, 203] but at this stage of developing the device more robust solutions, such as the use of active electrodes, are not considered [204]. An appropriate design of electronics may also minimise the effect of unwanted signals.

Statistical bandwidth

It was mentioned that if samples are IID, specific maximum likelihood estimates may be used to estimate the amplitude depending on the type of random distribution. Thus, it is understandable that it has been shown that by de-correlating samples, the SNR and consequently the fidelity of a recorded signal increase, a phenomenon which is associated with increasing the statistical bandwidth of the signal [194, 205]. This process is referred to as whitening. The first stage of whitening is understandably to estimate the power spectrum of a recorded signal.

Blackman and Tukey [206] were the pioneers in proposing a discrete time truncated version of the Wiener-Khinchin [207] formulation for the power spectral density as shown in Equation (4.17):

$$\hat{S}_{xx}(k) = \frac{1}{N}\sum_{n=0}^{N-1} \hat{R}_{xx}(n) e^{\frac{-j2\pi kn}{N}} \tag{4.17}$$

where N is the sampling period and $\hat{R}_{xx}(n)$ is the estimate of the autocorrelation function, R_{xx}, as shown in Equation (4.18):

$$R_{xx}(n) = \frac{1}{N}\sum_{l=0}^{N-n-1} x(l)x(l+n). \tag{4.18}$$

This approach is performed in two stages, negative values can appear in the estimate and might have a poor resolution.

The other approach which is perhaps more intuitive is to perform a discrete Fourier transform (DFT) such as the fast Fourier transform (FFT) on a windowed ($w(n)$) segment of the signal. The windowing is known to minimise the spectral leakage. This method is shown in Equation (4.19):

$$\hat{S}(k) = \frac{1}{N}|\sum_{n=0}^{N-1} x(n)w(n)e^{\frac{-j2\pi kn}{N}}|^2 \tag{4.19}$$

This method, also, has its limitations. Namely, the only way to improve the resolution is to record for a longer period, there is an assumed periodicity and spectral smoothing is required due to the inherent instability.

A predictive model which overcomes the shortcomings mentioned for the other two methods is the auto-regression or all-pole model. This model works based on the assumption that the value of any sample can be predicted by a linear weighted aggregate of the previous samples and a white noise driving force. Thus, the power

spectral density can be shown in Equation (4.20) [197]:

$$\hat{S}(k) = \frac{1}{N} \frac{T\sigma^2}{|\sum_{n=0}^{p} a_n e^{-j2\pi knT}|^2} \tag{4.20}$$

where a_n is the auto-regression coefficients, p is the order of the model, T is the inter-sample distance and σ^2 is the variance of the noise. Various methods can be used to calculate the coefficients. Using a discrete moving average filter as shown in Equation (4.21) it is possible to whiten the signal [195, 197].

$$\varphi_w(l) = \frac{1}{\sqrt{b_o}}\varphi(l) + \frac{-a_1}{\sqrt{b_o}}\varphi(l-1) + ... + \frac{-a_p}{\sqrt{b_o}}\varphi(l-p) \tag{4.21}$$

where $\varphi(.)$ is the signal and $\varphi_w(.)$ is the whitened signal.

Various contributions have analysed different features of whitening such as different implementations of the autoregressive filter and adaptive whitening [208–212]. It has been shown that similar effects may be achieved using an adjusted IES [194, 213] which will impose much less complexity in the design. From the theoretical analysis presented above, it is clear that the operations are involved and the complexity-efficacy of the target application should be considered. Although the evidence for improvements of the amplitude estimation is shown but none of these techniques have been widely implemented [214]. For an online processor, the complexity increases significantly. Thus, it should be investigated whether signals are decorrelated or not by adjusting only the IES.

The other issue regarding the amplitude estimation is the fact that a single channel can only monitor a segment of a target muscle. Thus, it has been proposed that by combining recordings from multiple sites it is possible to increase the SNR of the estimated amplitude [194, 213, 215, 216]. To improve the SNR, sites should be temporally and spatially uncorrelated. In the case of correlated sites, de-correlation filter should be used. This filter can be derived from the eigenvalues and eigenvectors of the inter-site covariance matrix [215]. As before, the

applications implementing such methods are sensitive to the exact level of the associated muscular activity, which is not the case in the target application of this thesis. If a multi-channel recording is considered, more functional blocks are required to spatially de-correlate the sites and aggregate the final samples. Depending on the application and the level of the SNR required, the appropriate modules should be incorporated in the design. It is worth re-iterating that the appropriate design trade-offs, in terms of the level of power consumption, system complexity and functionality, should be taken into account.

Maximum likelihood estimate

Traditionally, the distribution of the EMG amplitude has been represented by a Gaussian distribution [217,218]. It has been shown that if a Laplacian distribution is considered, MAV yields the best SNR. However, experimental studies have shown little or no difference in the SNR performance of these estimators [219]. Therefore, in the remainder of this chapter the assumption is that the EMG signal has a Gaussian distribution and as it will be shown the RMS estimator is the maximum likelihood estimator.

Assuming a signal trace is filtered and whitened, samples may be considered to be IID. Going back to the main functional model of the SEMG, it was mentioned that a white zero-mean Gaussian noise is passed through a shaping filter and multiplied by the amplitude which is a function of the muscular activity. The mentioned amplitude imposes itself as the standard deviation of the Gaussian distribution representing the SEMG samples as shown in Equation (4.22):

$$SEMG(nT) = \frac{1}{\sqrt{2\pi}\sigma(A)} e^{\frac{-SEMG(nT)^2}{2\sigma(A)^2}} \tag{4.22}$$

where A is the said activity. The goal is to find under what circumstances for a given estimate of a muscular activity ($\hat{A}$), the probability of having a set of SEMG samples ($SEMG_o$) is at its maximum for a range of muscular activity as

defined by Equation (4.23):

$$\frac{dp(SEMG|\hat{A})}{dA} = 0. \tag{4.23}$$

Thus, for N samples of the SEMG signal, it is possible to derive the conditions as shown in (4.24) by considering the log-likelihood function:

$$\begin{aligned}
&\frac{d}{dA}p(SEMG|A) = \frac{d}{dA}\prod_{n=1}^{N}\frac{1}{\sqrt{2\pi}\sigma(A)}.e^{\frac{-SEMG_n^2}{2\sigma(A)^2}} \\
&\Rightarrow \frac{d}{dA}ln(p(SEMG|A)) = \frac{d}{dA}\sum_{n=1}^{N}ln(\frac{1}{\sqrt{2\pi}\sigma(A)}.e^{\frac{-SEMG_n^2}{2\sigma(A)^2}}) \\
&= \frac{d}{dA}(-Nln(\sqrt{2\pi}) - Nln(\sigma(A)) - \frac{\sum_{n=1}^{N}SEMG_n^2}{2\sigma(A)^2}) \\
&= \frac{\frac{d\sigma(A)}{dA}}{\sigma(A)}(\frac{\sum_{n=1}^{N}SEMG_n^2}{\sigma(A)^2} - N) = 0 \\
&\Rightarrow \sigma(A) = \sqrt{\frac{1}{N}\sum_{n=1}^{N}SEMG_n^2}
\end{aligned} \tag{4.24}$$

which shows that the RMS of the samples can be used as an estimate of the standard deviation as the amplitude of the zero mean random process. What was not discussed in relation to the maximum likelihood estimate was how one should choose N, the number of samples for a given estimation. In a dynamic setting, it has been shown that the noise of the estimate (the standard deviation of the amplitude estimate as defined in Equation (4.16)) diminishes as the number of samples increases [213,220,221]. The smoothing function of the window length is, thus, obvious. However, in such a setting excessively large windows fail to follow the variations of the amplitude. Thus, depending on the application, a reasonable trade-off should be sought. Alternatively, it has been shown that an adaptive window length may improve the performance of the estimator [221]. Yet again, since the bladder activation is a relatively slow process, using large smoothing windows is possible. Based on the discussions so far, the SNR for an RMS estimator can be shown as a function of the number of independent channels

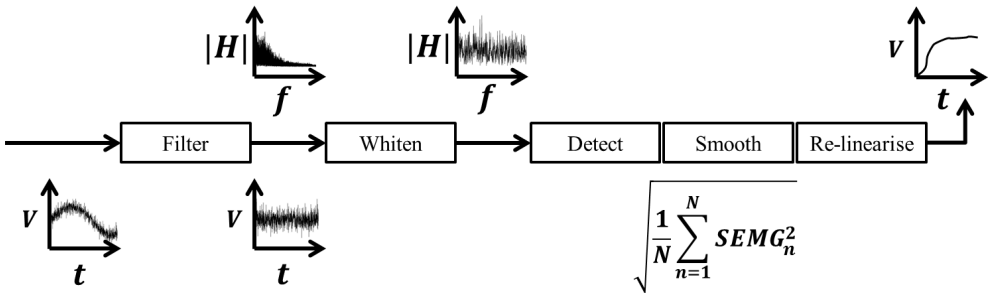

Figure 4.7: Block diagram of the amplitude estimation steps. While the RMS has been mentioned in the figure, other methods of the maximum likelihood estimation have been also proposed. The figure was drawn based on the concepts and figures in [151].

N, the statistical bandwidth B_s and the window length in time, T_s, as shown in Equation (4.25) [187, 213, 220, 221]:

$$SNR = \sqrt{2T_s 2B_s N} \tag{4.25}$$

in which understandably T_s is a function of the number of samples and the sampling frequency. The overall system of the amplitude estimate is shown in Figure 4.7.

4.2.10 SEMG from EAS

What was mentioned so far gives all the necessary theoretical background to decide on different features of the design of an SEMG amplitude estimation system. The physiological parameters should lead the design, in such a way that in designing the electrodes, the orientation of muscle fibres and the positions of IZs and EZs, the relative size of muscle fibres, and the CV of the target fibres should be considered. The complex anatomy of the EAS involves striated muscle fibres which are arranged in a relatively circular fashion. However, the fibres may cross anteriorly towards the centre of the perineum variably in different individuals. From the anal orifice towards coccyx, different annular sections (subcutaneous,

superficial and deep) have been identified. At different sections, particularly at deeper segments, the muscle is traversed by other muscular structures in the vicinity [222].

Early devices for the EAS SEMG inspection incorporated ring electrodes placed along the anal canal for single differential recordings [223]. Given that the muscle fibres are generally circular, it is likely that with this configuration electrodes are placed on different fibres. In such a configuration the contraction of the EAS results in the MUAP propagation and a level of signal is recorded. However, the acquired signal does not follow any of the aforementioned analysis and is probably merely due to the temporal correlation of activities in different MUs in the same muscular structure. Binnie et al. [223] compared the level of rectified smoothed signals between a bipolar recording in which ring electrodes were placed along the anal canal and the other with rectangular electrodes (2.5 mm $\times$ 20 mm) placed circumferentially at the same depth of the anal canal. They recorded higher levels of the signal for the latter case as predicted by the presented theory. However, they placed electrodes on either side of the anal canal (six and twelve o'clock) which does not consider the fibre length and the possibility of recording from different sides of an IZ as well as frequency filtering effects. In other early clinical studies involving the EAS EMG recording, electrodes were usually placed around the anus. This method to a higher degree suffers from the obscurity of the underlying recorded physiological parameters. Moreover, a perianal recording may record from any perineal muscle [224].

After a relative standardisation of the SEMG acquisition methods and the analysis of underpinning elements, the majority of the studies involving the EAS EMG recording used rectangular electrodes placed circumferentially with a relatively small spacing [153, 154, 222, 225–231].

The advent of the multi-channel recording apparatus for the recording from the EAS and the development of appropriate decomposition algorithms led to thorough studies on the EAS. The proof of concept study by Merletti *et al.* [222]

demonstrated the possibility of identifying the position of IZs and EZs as well as the CV of fibres. They used a plastic anal probe, 14 mm in diameter with 16 circumferentially mounted equally spaced rectangular electrodes. The electrodes were Ag bars 1 mm in width, 10 mm in length and spaced 2.75 mm from one another. They acquired single differentially and clockwise by adjacent electrodes and used decomposition algorithms to identify unit MUAPs. It should be noted that every electrode averages the contribution from different MUAPs, hence such decompositions are necessary.

Using similar methods Enck *et al.* in a study on healthy individuals (n=52) identified the position of IZs and EZs at different depths from the orifice [225]. The statistical distribution of these zones is of great interest in the design of the SEMG sensor in this thesis. They demonstrated that while the signal tends to be stronger near the orifice, the zones were less populated anteriorly and posteriorly (at 12 and 6 o'clock) on the circumference. Using similar devices, an estimate of the CV was derived in [153]. This is particularly important as the study showed a very low level of the CV at the surface of the electrodes with a considerable variation across the population. Therefore, any study should consider these variations. In a study by Mesin [229] it was theoretically proven that the signal recorded from circular fibres at a constant depth in the muscle and aligned with the recording array has a zero spatial mean. Thus, mono-polar recordings were estimated based on single differential recordings analytically with little error. It was demonstrated that the misalignment of the array, variations in the depth and deviations from the circular formation result in considerable errors in estimations. Cescon *et al.* [230] building up on that study tried to investigate the anatomy of the EAS and the general considerations in recording the SEMG based on [229]. Corroborating the existing understanding of the EAS structure, they noted that the contribution of the common mode is lower at a lower depth of the anal canal. They noticed that the circular formation is very likely to be relatively well-formed at a lower depth of the anal canal.

This concludes the theoretical review of all the issues directly related to the SEMG recording for the amplitude estimation. The following section focuses on the issues surrounding the electrode-tissue impedance as it was touched upon earlier.

4.2.11 Electrode-tissue impedance

As it was mentioned before, one of the important issues surrounding contacting a recording electrode to the human body is the generation of an electrical impedance at the interface of the electrode and tissue. This topic is involved and an accurate analysis is beyond the scope of this thesis. Understanding the underlying principles of an accurate modelling paradigm requires an intricate understanding of the electro-chemical processes. However, a heuristic understanding of the electrode-tissue interface loading effect is of great interest in designing the recording apparatus. The goal is to have a functional electrical equivalent model describing the electrode-tissue interface if the impedance at different frequencies is known.

When a metallic electrode comes into contact with an electrolyte, at the surface it may lose electron (oxidation), in which case the corresponding ions are released in the electrolyte. the reduction of ions and their deposition on the electrode is also possible. Such interactions at the interface and further adsorption of ions generate a separation of charges at the interface which may lead to quasi-capacitive effects at the interface. The actual process is much more complex but the brief description mentioned here should suffice to arrive at a functional understanding of the interface and a model. The capacitive and pseudo-capacitive effects of the interface may be referred to as the double layer (DL) [232].

Apart from the said effects, depending on the level of the applied signal and the electrode material, there is an actual charge transfer across the interface due to the oxidation and reduction processes occurring [233, 234]. Thus, there are two parallel current flows involved at the interface: the capacitive/pseudo-capacitive

current and the Faradaic current. Hence, the overall impedance may be modelled by a parallel combination of a charge transfer resistor (R_{ct}) and a double layer capacitor (C_{dl}). The expression shown in Equation (4.26) based on Butler-Volmer equation defines R_{ct} [233, 235].

$$R_{ct} = \frac{RT}{nFJ_o} \tag{4.26}$$

where R is the gas constant, T is the temperature [K], F is the Faraday constant, n is the number of electrons and J is the current density.

Faradaic currents are dependent on the existence of ions at the interface. Therefore, it is important to account for the time it takes for the ions to diffuse and reach the surface. This process essentially further impedes the Faradaic processes. So, in the equivalent circuit representing the interface an extra element referred to as the Warburg element should be placed in series with the resistor representing the Faradaic processes. The expression for the Warburg impedance is given by Equation (4.27) [233, 235]:

$$Z_W = \frac{(1-j)D}{\sqrt{\omega}} \tag{4.27}$$

where D is the diffusion coefficient [$\frac{\Omega}{\sqrt{\omega}}$]. For recording electrodes in which case a limited current level through electrodes exists the DL effects of the interface is of greater significance. It has been shown that for a solid electrode tissue interface the DL demonstrates a frequency dispersion of the capacitance. This effect is attributed to the physiochemical effects at the interface and the surface roughness. It has been shown that these effects may be modelled by replacing C_{dl} with a constant phase element (CPE) [235]. Different representations of the impedance of the CPE can be found in the literature but the one shown in

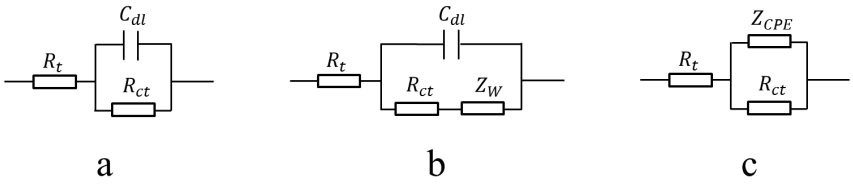

Figure 4.8: Equivalent electrical models of the electrode-tissue impedance. a: the interface is modelled using a simple RC circuit b: Warburg element is implemented to represent the ion diffusion dependent Faradaic current c: using Z_{CPE} to ensure the frequency dispersion of the capacitance is modelled.

Equation (4.28) has been shown to better represent the effects [236].

$$Z_{CPE} = \frac{1}{Q(j\omega)^{\alpha}} \tag{4.28}$$

where Q is a coefficient analogous to capacitance in a capacitive impedance and α is an exponent between zero and one and is a measure of the departure from capacitive effects.

Figure 4.8 shows the aforementioned models in which R_t is the resistance of the tissue. If there are two electrodes involved, another parallel combination of Faradaic and non-Faradaic currents closes the loop. In that case R_t is a function of the medium resistivity and electrode spacing. Models shown in Figure 4.8a and Figure 4.8c are of interest due to their simplicity and accuracy, respectively. The impedance of the model shown in Figure 4.8a can be written as in Equation (4.29) [237]:

$$\begin{aligned} Z &= \frac{1}{\frac{1}{R_{ct}} + sC_{dl}} + R_t = \frac{R_t + R_{ct} + s(R_{ct}C_{dl}R_t)}{1 + sR_{ct}C_{dl}} \\ &= (R_t + R_{ct})\frac{1 + \frac{s}{\frac{1}{R_{ct}C_{dl}} \times \frac{R_t + R_{ct}}{R_t}}}{1 + \frac{s}{\frac{1}{R_{ct}C_{dl}}}} \end{aligned} \tag{4.29}$$

where s is the Laplace variable. This representation of the impedance as shown in Equation (4.29) helps in understanding the frequency behaviour of the model more intuitively. At low frequencies ($s \to 0$) the impedance tends to $R_{ct} +$

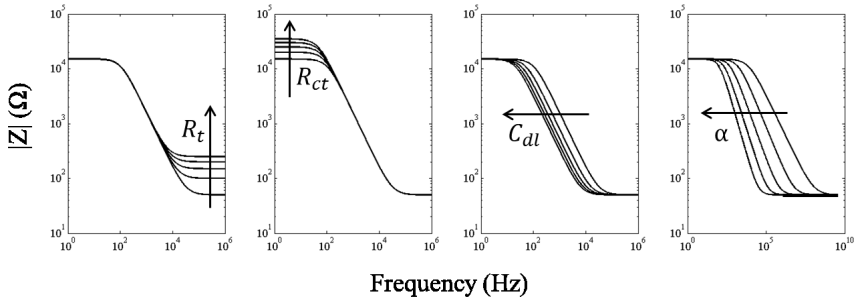

Figure 4.9: The effect of variations in different components of the electrode and tissue impedance. The arrow points in the direction of increasing every component. For instance, R_t is increasing in 100 Ω increments, R_{ct} in 1 KΩ increments, C_{dl} in 1 nF increments and α in 0.1 increments.

R_t. The value of C_{dl} essentially shifts the corner frequencies. In the case of Z_{CPE}, s is raised to a power, hence the rate at which the magnitude of the impedance changes at a range of frequencies varies. This functional understanding of the combined effects of the tissue and interface is helpful in understanding the effect each one has in the frequency response of the aggregate system. Any attempt in modelling the impedance should consider these bounds and assign the corresponding limits. Figure 4.9 demonstrates the effect of linear variations of each of the factors in the combined impedance of the interface and tissue.

4.2.12 Modelling CPE

Given that the frequency dispersion of the capacitance may be attributed to surface roughness [238, 239] and considering a model of fractal formations [240] for a porous surface, an RC ladder may be used to approximate the effect that the CPE element functionally represents [241]. Figure 4.10 shows a schematic of a two-dimensional pore. The same idea can be applied in three dimensions and a further distribution of pores in a fractal fashion may be considered. An aggregate effect may be considered. Partly functionally and partly physiochemically modelling the effects observed due to the impedance of the interface, a useful model of it may be developed. How complex the model should be in terms of the number of ladder stages and dimensions depends on the case in which the

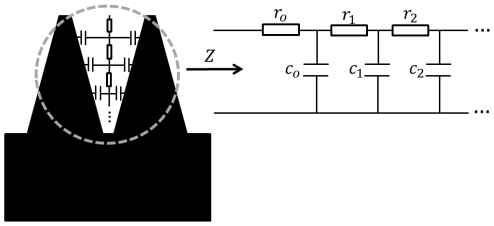

Figure 4.10: Two dimensional schematic of surface pore of an electrode and the corresponding impedance. This is simply a two dimensional representation of the pore but a fractal pattern may develop in three dimensions. The aggregate effect of the impedance may still be represented by a single ladder. Figure drawn based on figures and concepts in [149].

model is applied. For a ladder shown in Figure 4.10, the expression to calculate the impedance is given in Equation (4.30):

$$Z = r_o + \cfrac{1}{j\omega c_o + \cfrac{1}{r_1 + \cfrac{1}{j\omega c_1 + \cfrac{1}{r_2 + \ldots}}}} \tag{4.30}$$

4.2.13 Design objectives

The main objective of the design is to be able to record the SEMG signal, correlated only with the activity of the target muscle with an acceptable SNR using a minimum number of electrodes made of stainless steel. The electrodes should make a sufficient contact with the tissue while the tissue is minimally prepared. Thus, based on the theories provided, electrodes should be designed. However, practical considerations should lead the design in a sense that a trade-off should be sought to change the best theoretical design to a practical design with the best performance.

4.3 Materials and methods

The following section describes in detail the materials and methods implemented to achieve the above mentioned objectives.

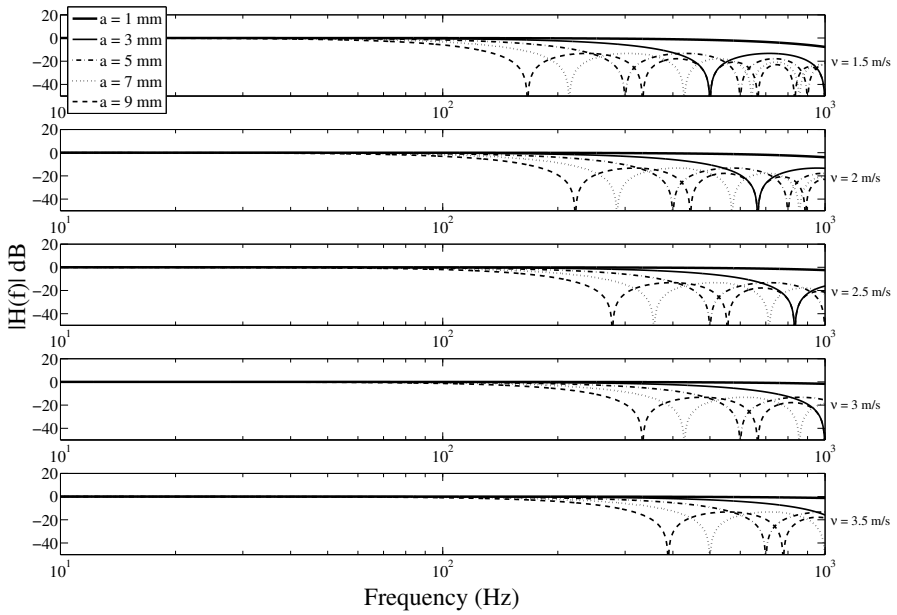

Figure 4.11: Frequency response of rectangular electrodes of different widths for different CVs. For all CVs, $a \leq 5$ mm will ensure that the majority of the SEMG power is below the first dip.

4.3.1 Designing the electrode size, shape and position

Given that fibres are generally circularly arranged in the EAS and as electrodes should be placed along the fibre direction, the electrodes should be placed circumferentially. One should minimise the electrode extension along the fibre to ensure the metallic surface low-passing is minimised. However, this theoretical rule is limited by the possibility of manufacturing electrodes and by the necessity of having a sufficient electrode-tissue contact. Based on Equation (4.11) for five electrode widths the frequency response of the metallic surface is shown for various CVs in Figure 4.11. For all CVs, if the electrode width (a) is less than 5 mm, the first dip is placed above that of the SEMG bandwidth. For $a \leq 3$ all the SEMG bandwidth is completely below the first dip. Having elongated electrodes help in recording from a pool of MUs. Thus, having rectangular electrodes is favourable. There is a limit to how long the rectangular bars can be. Given that the fibres are not completely circular, elongated segment of the bar may contribute to the low-pass filtering of the electrodes. As the electrodes go

further in the anal canal, there is more chance of recording from other muscular structures in the vicinity. Based on the studies on the SEMG acquired from EAS, 1 cm bars should be sufficiently large to record from a pool of MUs and small enough to avoid a considerable cross-talk if they are placed in 1 cm depth from the anal orifice.

4.3.2 Design of recording paradigm and IES

Using three electrodes, it is possible to form a DD configuration which has been shown to limit the recording volume as a spatial filter. The DD recording demonstrates the same bandwidth as the SD but has inherently higher gain as shown in Figure 4.12. However, it should be noted that for small muscle fibres the electrode assembly should take as little space as possible to avoid facing IZs and EZs. There is a minimum electrode spacing due the possibility of shorting electrodes as also reported in the literature [230]. Also, the chance of electrode failures increases as the number of electrodes increase. Thus, considering a minimum spacing of 5 mm and noting that the electrodes also have a finite width, a system involving three electrodes may be too large for short muscle fibres such as EAS. The issue of focusing the volume to avoid cross-talk may be addressed by placing the electrodes at a lower depth in the anal canal [230]. Figure 4.13 shows the low-pass effect of a larger IES for SD configurations. From the considerations mentioned above and the results shown in Figure 4.13 it is possible to adopt a 5 mm IES as the appropriate spacing. It also seems to be the right IES as it does not suppress the low frequency components of the SEMG significantly. It is possible to combine the effects of the electrode spacing ($d = 5$ mm) and electrode size for an SD configuration by multiplying the transfer functions of the electrode and the configuration as shown in Equation (4.31):

$$H(f) = sinc(\frac{a}{\nu}f) \times 2jsin(\frac{\pi d}{\nu}f). \tag{4.31}$$

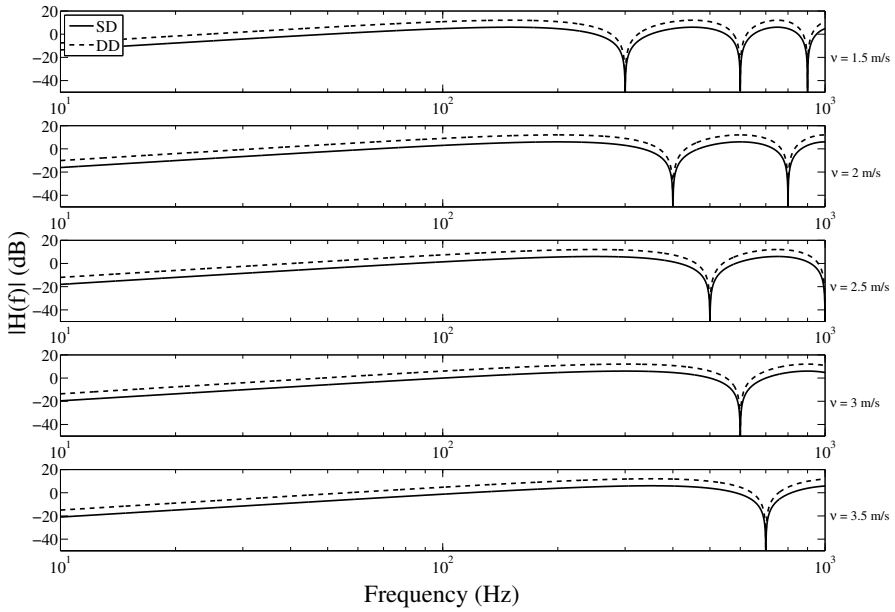

Figure 4.12: Frequency response of the SD and DD configurations for 5 mm IES for different CVs. The limiting factor is the CV as observed at the surface of the electrode. Also the sensitivity of the DD configuration is higher at lower frequencies.

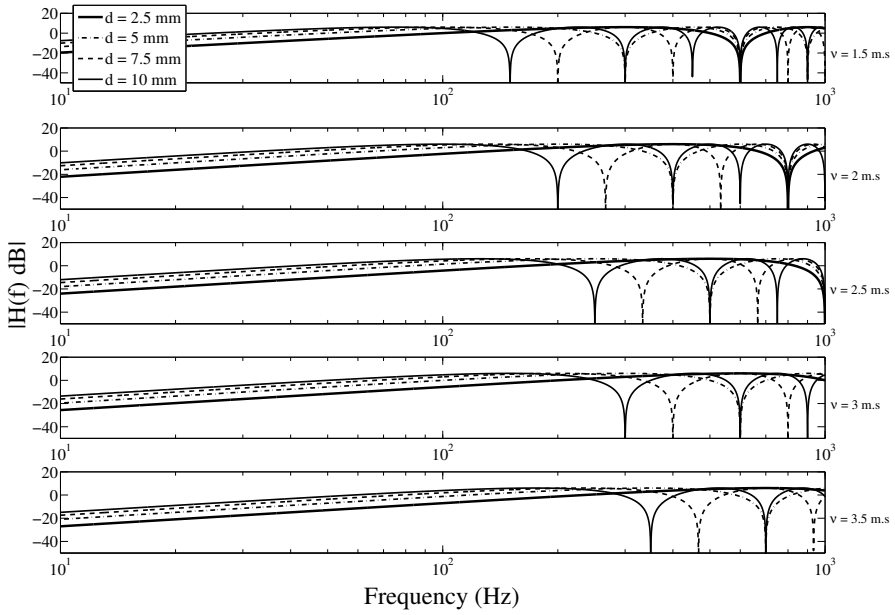

Figure 4.13: Frequency response of the SD configuration for different IES for different CVs. For a smaller IES there exists a reduction in the sensitivity at low frequencies. for all CVs, $d = 5$ mm has its first dip above the SEMG frequency spectrum and does not show a major reduction in its sensitivity at low frequencies.

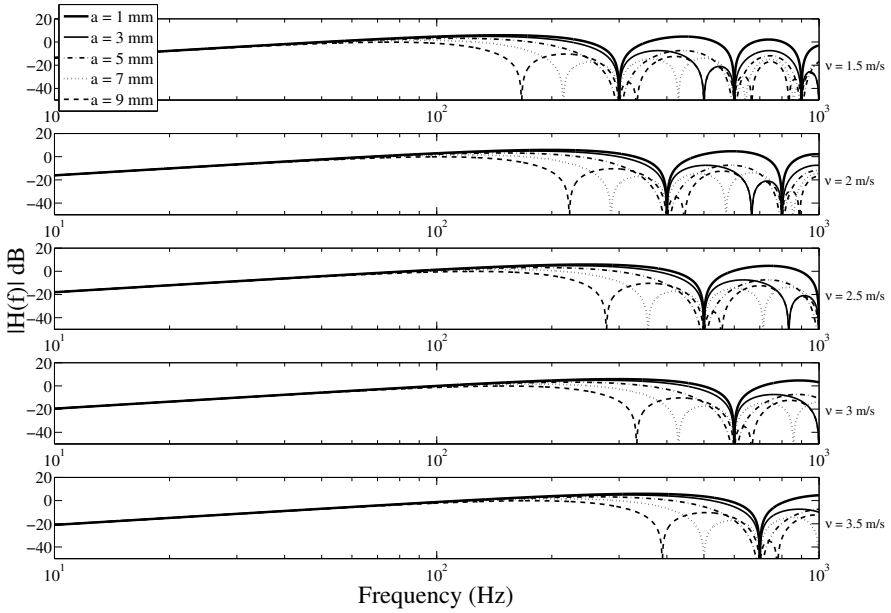

Figure 4.14: Frequency response of the SD configuration using electrodes of different width (1 mm - 9 mm) and IES = 5 mm for different CVs. Low frequency and high frequency sensitivities should be noted in designing the system.

For a large IES ($d \geq 5mm$) the chance of suppressing a part of the SEMG increases depending on the CV as shown in Figure 4.14.

4.3.3 Probe size

A variation has been reported with respect to the size of the anal canal in different individuals as discussed in Chapter 2. The structural design of the probe on which the electrodes are mounted is beyond the scope of this thesis although a general overview of the overall design will be given in Chapter 5. It is likely that several sizes of the probe may be required for individuals of different sizes. At this point the diameter of the probe is set to be just below 2 cm, not very different from the previously used designs.

4.3.4 Testing theory

Based on the presented theory and simulations as described above, a set of specifications were produced which are summarised in Table 4.1. The point worth reminding is that the main objective is to be able to record a signal correlated

Table 4.1: Suggested SEMG probe specifications based on the theoretical analysis.

Design parameter	Suggestion
Recording configuration	SD
Electrode shape	Elongated along the probe axis (rectangular, oval)
Electrode size	1-3 mm along the fibre direction and 1 cm along the probe axis
Electrode position	1 cm from the anal orifice
Probe diameter	1.8 cm

with the muscular activity. Existing commercial anal probes implement considerably larger electrode sizes. One of the main factors in a practical design of the recording electrodes is that they should make contact at all times. This may be achieved more readily using larger electrodes. Also, larger electrodes may produce larger signal amplitudes due to the overall averaging effect of the metallic surface of electrodes. In addition, larger electrodes may be able to operate under the no-preparation condition better. Furthermore, although suggestions indicated that the electrode spacing should be small enough to ideally place electrodes between an IZ and its EZ, yet it may be possible to record a sufficient SEMG signal indicative of the muscular activity even if the rules are not completely followed. Also, if the electrodes are widely separated the chance of electrode shorting is reduced. Therefore, in the one-off test, whose description is presented in this chapter, it is imperative to also investigate the acquired signal due to larger electrode spacings and sizes beyond the suggested specifications.

A set of four electrode specifications were produced to test all the hypotheses derived from the theoretical analyses and all the practical considerations mentioned above as shown in Table 4.2. It is noted that a one-off test on one subject does not necessarily predict the result of the same study on a large sample group. However, it is enlightening as it puts design strategies into perspective by indicating the relative gain required for a given design, giving an indication as to whether or not a design may have a chance of producing an adequate SEMG signal, and yielding an estimate of the signal processing specifications in a pre-clinical study. The outcome of theoretical analyses, the existing data in the literature and the

one-off test should be able to produce sufficient insight into designing the first prototype.

Table 4.2: Specifications of probes to test theory and practicality.

Probe	No. of electrodes	Electrode size	Electrode spacing	Notes
A	2	15×20 mm	13.5 mm	[1]
B	4	10×20 mm	5 mm	[2]
C	4	3×10 mm	5 mm	[3]
D	4	1×10 mm	5 mm	[4]

4.3.5 Manufacturing devices

Figure 4.15 shows the manufactured [5] SEMG devices. The body of probes A and B were made by machining solid rods of polyether ether ketone (PEEK). The white anchors were made from acetal rods and the tip from acrylic rods. The electrodes were made from 316 medical grade stainless-steel and were screwed to the body by machining recesses into the body in their places. The gaps at the edges of the electrodes were filled using henkel loctite hysol medical epoxy. The body of probes C and D were designed using FreeCAD (a freely available 3D drawing package) and fabricated using 3D printing out of VeroWhite material. The tip, anchor and the black cable housing compartments were made out of acetal. The electrodes were made by rolling stylets from hypodermic needles and pressing them into the body like staples. This process produces rectangular

[1] Large electrodes are placed laterally, similar to the existing commercial devices. The electrodes are more elongated than suggested theoretically. A reference ring placed $\sim$ 4 cm from the anal orifice is implemented to test the possibility of using an internal reference.

[2] Electrodes are smaller than in A but have a similar elongation. An array of electrodes is placed to test the effect of the electrode position and spacing. Thus, Electrodes are larger and more elongated than theoretically suggested.

[3] An array of electrodes within the boundaries of theoretical suggestion should be implemented to test the effect of the electrode position and spacing. Electrodes are aggregated on one side of the bearing cylinder to increase the chance of placing the array on one side of an IZ and EZ.

[4] An array of electrodes at the minimum manufacturable theoretical suggestion should be implemented to test the effect of the electrode position and spacing. Electrodes are aggregated on one side of the bearing cylinder to increase the chance of placing the array on one side of an IZ and EZ.

[5] The devices were manufactured in collaboration with Dr. Sandy Mosse in UCL department of medical physics and biomedical engineering.

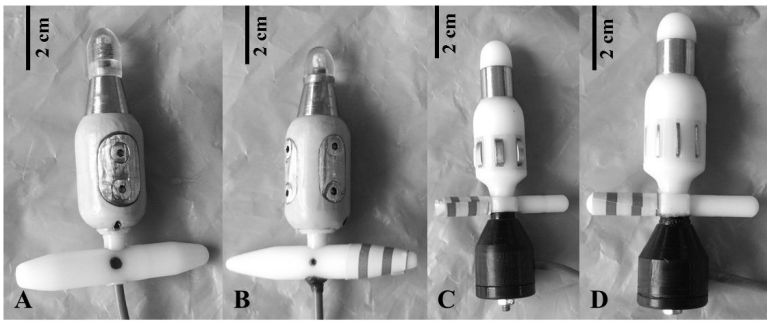

Figure 4.15: Manufactured intra-anal SEMG probes. Different electrode specifications were manufactured to test the theory and practicality of different designs. The specifications of each probe and the associated test hypothesis can be found in Table 4.2

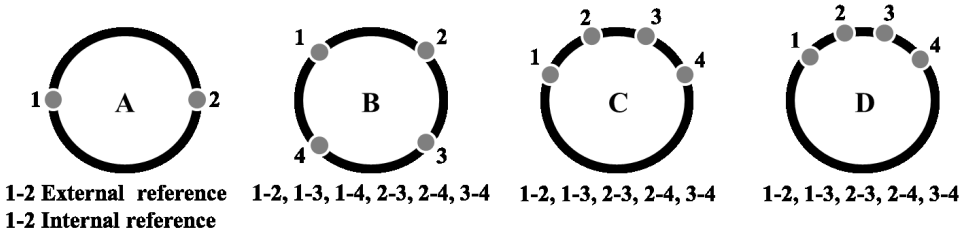

Figure 4.16: Electrode and configuration naming pattern for SEMG probes. As the probes are inserted the top side is placed facing up, thus, the electrodes face the sacrum.

electrodes with round ends. The gaps were filled using the same epoxy as before. A multi-core screened wire was used and each core was soldered to an electrode on one end and to a one pole jack plug on the other. The screen was floating in all cases.

4.3.6 Experimental protocol and apparatus

Figure 4.16 shows a schematic depicting the electrode naming pattern used in this section for each probe. In addition, the SD recordings which were planned to be carried out using each probe during the experiment are shown below each schematic. For probe A, since there are only two electrodes, one SD recording is possible. One SD recording was planned to be recorded using an external adhesive reference electrode placed on the abdominal region of the subject and the other using the ring electrode at the tip of the probe as reference. For probe

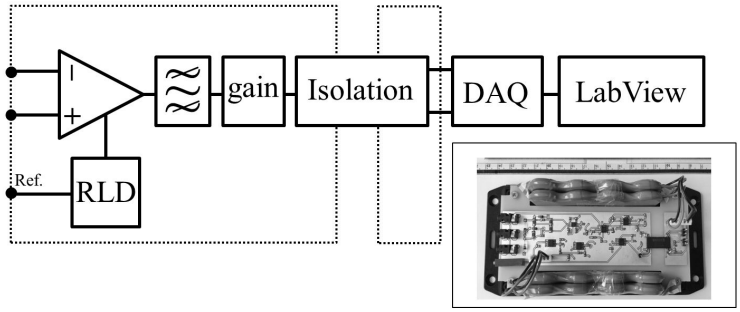

Figure 4.17: Schematic of the SEMG recording experiment setup. Electrodes are connected to the PCB via shielded wires connected to audio jack plugs. Signals are recorded single differentially with an initial gain of ×500. A right-leg-drive (RLD) circuit is used to reduce the common mode signal. A secondary gain stage (MAX gain= ×6) is used after filtering the signal (0.2 Hz - 1062 Hz). An isolation stage ensures patients' safety while conveying the signal to a personal computer running LabView via a DAQ. The inset shows the custom made electronics.

B, by acquiring an SD recording, implementing different electrodes, the effects of electrode placements and spacings were planned to be investigated. For probe C and D, the spacing was confined to a maximum of one electrode in between. Similarly, the effects of electrode placements and spacings were planned to be investigated utilising different electrodes.

A battery operated pre-amplifier with a right-leg-drive (RLD) circuit based on the work presented in [242] was designed and implemented on a printed circuit board (PCB). The gain of the pre-amplifier was set to ×500. After a band-pass filtering stage (0.2 Hz -1062 Hz) a secondary gain stage was devised (×1 - ×6), yielding a total gain of ×3000. Using electric isolation (ISO122, a precision low-cost isolation amplifier, Texas Instruments Inc.) the subject side was isolated. An NI DAQ 6008 (National Instruments Corporation) was used to acquire signal with a 12 bit resolution at a rate of 5 Ks/s on a personal computer (PC). Data were recorded and the signal was processed at the first stage in LabView (National Instruments Corporation). In LabView, the raw data, filtered data (30 Hz - 500 Hz using a 10th order Butterworth) and filtered data passed through a notch filter ($\sim$ 50 Hz) were set to be visually inspected at the time of the experiment. Figure 4.17 shows the schematic of the apparatus.

4.3.7 Experiment

With the approval of the local research and development review, the subsequent studies were performed on a male volunteer. Throughout the experiment, a clinical scientist was present as the supervisor of the experiment. Each of the devices was tested for intact connectivity of all electrodes just prior to the insertion. The devices were inserted through the anal orifice of the subject. All the configurations shown in Figure 4.16 were tested in sequence. For each configuration, the subject was prompted to contract his EAS three times, first and last times strong and a weaker second time. Each contraction lasted less than 10 s and the overall recording took about 60 s for each SD configuration. The gain was set to about $\times 1600$ as it was verified after the experiment by recording the value of the potentiometer which controlled the gain. The gain was set to a level that a reasonable swing could be observed without saturation.

Electrode 3 connection in probe B and 4 in probe C failed after insertion, resulting in the experimenter not being able to test 3 of the configurations as originally intended. However, since enough data were acquired to judge on the efficacy of the configurations, no further experiment incorporating the test of the said three configurations was deemed necessary. In all the subsequent processing and presentations of the data, the data due to the failed electrodes were excluded. The connection failure is assumed to be due to rotations of the back compartment of the probes after insertion. A total of 14 sets of configurations were tested.

4.3.8 Post-processing

All the subsequent signal processing steps were performed in Matlab (MathWorks, Inc., Natick Massachusetts, US).

Filtering

The acquired signal was down-sampled to 1 Ks/s. This was done for the limitations imposed while implementing digital filters in Matlab. Thus, the sampling

rate was reduced to that allowed by the Nyquist rule. Given that a considerable movement of the electrode tissue interface is plausible under the conditions the SEMG recording is to be performed, the high-pass corner frequency was set to 30 Hz to suppress the movement artefact sufficiently in the first set of investigations. This proved to be an appropriate filtering level for the preliminary inspection as will be demonstrated for each electrode setting. The corner frequency of the low-pass filter was set to 500 Hz. A second order Butterworth band-pass filter was implemented with the said specifications.

Frequency spectrum

Cooley-Tuckey decomposition algorithm was used to perform an FFT of the acquired signal to inspect the frequency spectrum of the recorded data due to each electrode configuration. This is important as one may be able to spot any unexpected frequencies present in the spectrum and judge on the validity of the acquired signal, in terms of the amount of the SEMG signal present.

Sample independence

To investigate how de-correlated samples are, in each case, the autocorrelation of the dataset was calculated for all possible lags. The autocorrelation for a given lag (k) was calculated as defined in Equation (4.32) for a zero mean process [243]:

$$r_k = \frac{1}{\sigma^2(N-1)} \sum_{n-1}^{N-k} \varphi_n \varphi_{n+k} \tag{4.32}$$

where σ is the standard deviation of the samples and φ is the recorded sample.

Amplitude estimation

The RMS of the signal was calculated as a measure of the amplitude of the signal. The smoothing window length was set to 1 s as shown that this window size enhances the SNR. In addition, it has been shown that this window size is appropriate for the target application as reported in the literature [8].

The best electrode design

A visual inspection of the filtered signal, frequency spectrum, auto-correlation plot and the RMS was sufficient to reveal probe C as the one from which the acquired signal was most correlated with the muscular activity. Therefore, further investigations were performed on the said signal.

Smoothing window and high-pass corner frequency

The following study was performed to identify the right parameters in terms of the filtering and windowing for a signal only containing the SEMG signal. A segment of the recorded signal using the selected configuration during a contraction episode was selected. For high-pass corner frequencies ranging from 10 Hz to 30 Hz, the SNR of the RMS of the signal for the said segment was calculated for different smoothing windows from 100 ms to 500 ms. The higher smoothing windows were not tested given the duration of contractions and the subsequent SEMG signal available. Essentially, higher smoothing windows would not consider the SNR on a sufficiently large ensemble. In addition, this selection would ensure that any muscular activity is detected and by proxy the activities of the bladder are monitored without any delay in the target application of this thesis.

Filter order

The order of the used Butterworth digital filter (30 Hz - 400 Hz) was changed from 1 to 5 and the SNR of the RMS amplitude estimate whose smoothing window was set to 500 ms was calculated. The smoothing window and frequency range were set based on the study in the prior stage.

4.3.9 Electrode tissue impedance

Having a pair of 316 stainless steel electrodes (3 mm $\times$ 10 mm, $\sim$ 5 mm spacing) *in situ*, they were connected to a precision impedance analyser 6500B series (Wayne Kerr Electronics) supplied via an isolated power supply. The inspection voltage was set to 20 mV to avoid non-linearity and the impedance magnitude and phase

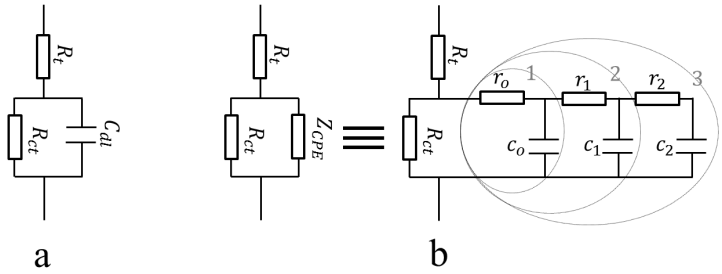

Figure 4.18: The two general models used to model the electrode tissue impedance. a: a simple RC circuit B: single or multi-stage ladder to represent Z_{CPE}

were recorded between 20 Hz to 200 KHz.

4.3.10 Electrode tissue modelling

In essence, modelling the electrode tissue impedance is a curve fitting exercise. However, it differs from a conventional curve fitting scenario in that there are two sets of data to be fitted simultaneously with respect to the frequency as the main variable. These two sets are the real and imaginary components of the impedance or its magnitude and phase.

Four different circuits were used to model the electrode tissue impedance: one with a simple capacitor representing the DL and three others in which a Z_{CPE} was used to model the DL effects. The two general circuits and the ladder approach in modelling the Z_{CPE} are shown in Figure 4.18. For the Z_{CPE}, an RC ladder of one, two and three stages were used which are referred to as Z_{CPE1}, Z_{CPE2} and Z_{CPE3} hereafter. The impedances of these circuits were modelled in Matlab and were divided into their respective real and imaginary components. The measured impedance was also decomposed into its real and imaginary components in a vector of two columns. A non-linear curve-fitting in least square sense was then used to fit the data by minimising the expression shown in Equation (4.33) using the trust-region-reflective algorithm based on the interior-reflective Newton

method [244]:

$$\sum_{n=1}^{N}(Z_{model}(RC, f_n) - Z_{experimental})^2 \tag{4.33}$$

where N is the number of data points, Z_{model} is a two-component (real and imaginary) impedance model, RC is a vector of resistor and capacitor coefficients, f_n is the frequency vector at which the impedance measurements were taken and $Z_{experimental}$ is a two column vector of real and imaginary measured data.

As the number of coefficients increases, the degrees of freedom and possibilities for the values the coefficients can assume increase. Therefore, it is important to define the lower and higher bounds of the coefficients to ensure realistic values are produced in the procedure. Given Equation (4.29) and the general bounds of any RC impedance at low and high frequencies, it is possible to assign the corresponding values to R_{ct} and R_t coefficients by considering the maximum and minimum values of the impedance at low and high frequencies, respectively. It should be noted that this method only produces a functional model and not necessarily one which portrays all the underlying physiochemical effects. Another way to incorporate such elements in the model is to assign values consistent with estimates of the respective coefficient in the literature. For instance, R_{ct} may be orders of magnitude larger than the maximum value observed in measurements within the frequency limits involved. If these more realistic values are to be incorporated in the model, more components (coefficients) may be required. This was the case in the present study.

4.4 Results

This section shows the results and the description of the results based on the experiments whose procedures were presented in the previous section.

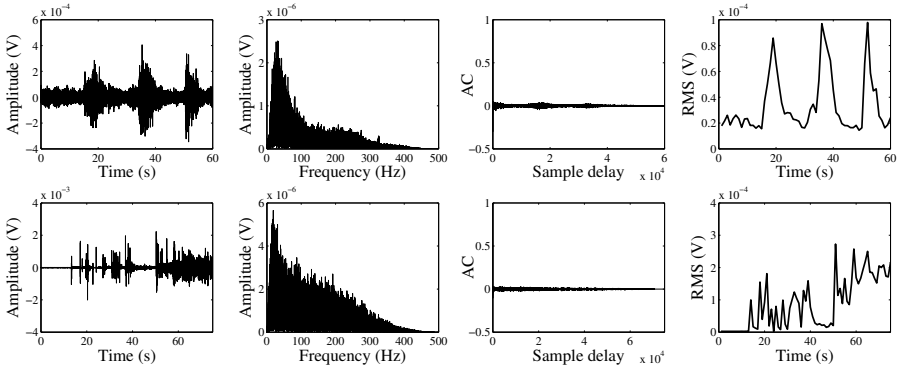

Figure 4.19: Probe A processed data. Top row shows 1-2 configuration implementing the internal reference electrode. Bottom row shows 1-2 configuration using the external reference electrode. The first column from left is the filtered signal (30-500 Hz), the second column is the frequency spectrum of the signal, the third column is the autocorrelation of the signal and the fourth column is the RMS with a 1 s smoothing window. While a correlated signal is recorded when implementing the internal electrode, this may be due to the activity of other muscular structures. A deformation of the spectrum can also be observed.

4.4.1 Measurements and post-processing

Figure 4.19 shows the recordings using Probe A while implementing the internal and external reference electrodes. While the recorded trace using the internal reference electrode shows a correlation with the muscular activity, in terms of its occurrence and not intensity, the recorded signal using the external reference electrode does not show such a consistent correlation. A considerable cross-talk is observed which is deduced from the starting level of the RMS in the case of the recording assembly implementing the internal reference electrode. A deformation of the frequency spectrum is observed which may be associated with the cross-talk as well. Finally, samples seem to be sufficiently de-correlated. Figure 4.20 shows the recordings using Probe B while implementing different electrode configurations. A partial correlation is observed between the recorded traces and the muscular activity. Configuration 1-4 shows an excessive 50 Hz contamination, demonstrated in the spectrum as well as the autocorrelation plot. This may be due to the incomplete contact between the electrodes and tissue. A very interesting observation is the cancellations observed in the recorded traces. This may be

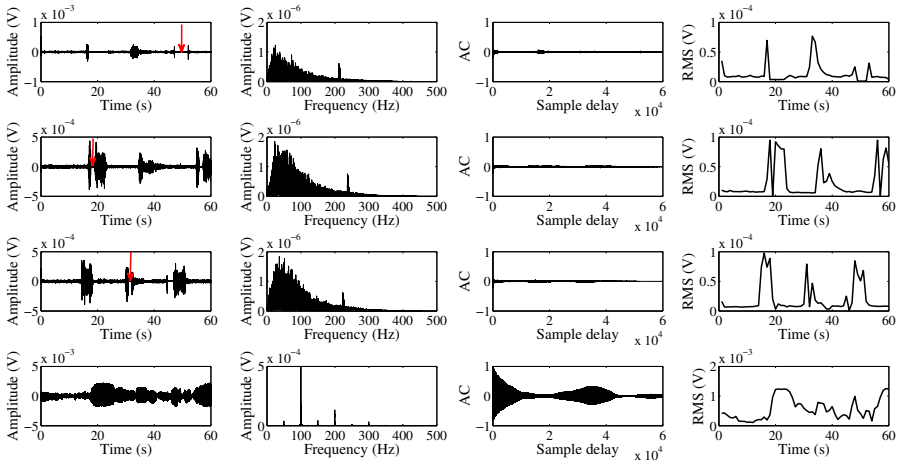

Figure 4.20: Probe B processed data. The first row from the top is showing the processed signal from 1-2, the second row from 1-3, the third row from 1-4 and the fourth row from 2-4. The first column from left is the filtered signal (30-500 Hz), the second column is the frequency spectrum of the signal, the third column is the autocorrelation of the signal and the fourth column is the RMS with a 1 s smoothing window. A very interesting feature of this recording is the phase cancellation observed. Instances of such an effect are indicated using red arrows. The signal due to 2-4 may be the result of an incomplete contact or a faulty electrode.

associated with the placement of the electrodes with respect to the corresponding IZs and EZs as described before. Figure 4.21 shows the recordings using Probe C while implementing different electrode configurations. A visible correlation between the muscular activity and the recorded trace is observed both in terms of occurrences and intensities which is also manifested in the RMS amplitude estimate. The traces of cross-talk are stronger for the larger inter-electrode spacings. The samples seem to be sufficiently de-correlated and the spectrum is consistent with those presented in the literature. Figure 4.22 shows the recordings using Probe D while implementing different electrode configurations. The major limiting factor based on the traces is the incomplete contact between the electrodes and tissue as demonstrated in the auto-correlation plot and the frequency spectrum. Configurations 1-2 and 2-4 show traces of the EMG activity but the signals are too weak, demonstrating that the stainless steel electrodes are too small for a reliable SEMG recording under the abovementioned conditions.

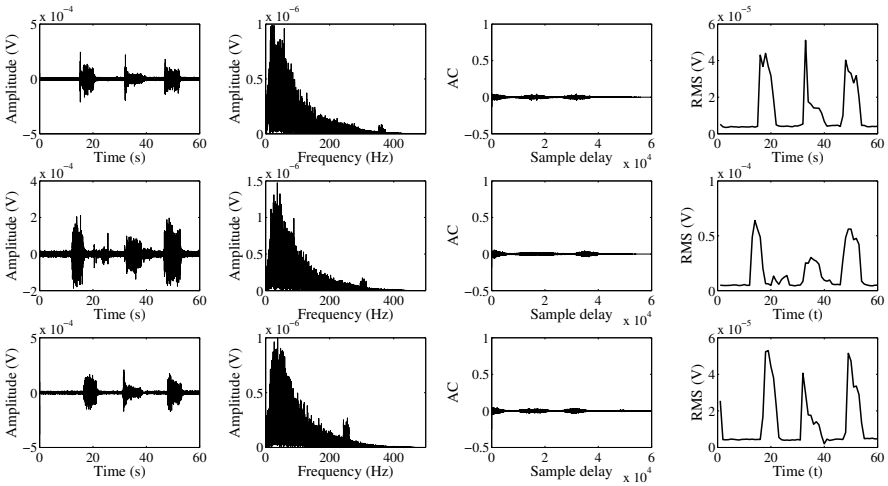

Figure 4.21: Probe C processed data. The first row from the top is showing the processed signal from 1-2, the second row from 1-3, the third row from 2-3. The first column from left is the filtered signal (30-500 Hz), the second column is the frequency spectrum of the signal, the third column is the autocorrelation of the signal and the fourth column is the RMS with a 1 s smoothing window. A distinctly correlated signal is recorded while samples of each recording seem relatively de-correlated. Increasing the IES increases the contribution from other components.

4.4.2 Smoothing, corner frequencies and filter order

Figure 4.23 shows the recorded trace from Probe C 1-2 configuration filtered at different high-pass corner frequencies and their respective RMS amplitudes implementing different smoothing widow lengths. It is noted that the spike at the beginning of the SEMG traces associated with the muscular activity diminishes at higher corner frequencies, indicating the presence of low frequency components in the said spikes. It is demonstrated that while increasing the window duration up to 400 ms improves the SNR, it does not improve much further for a window of 500 ms. Similarly, increasing the high pass corner frequency above 20 Hz does not significantly improve the SNR. The amplitude of the signal is also affected when the corner frequency is increased from 20 Hz to 30 Hz. For all smoothing windows and corner frequencies the difference between the two distinct levels are pronounced. The low-pass corner frequencies were also shifted from 400 Hz to 500 Hz and the resulting SNRs were investigated. However, no significant variation in

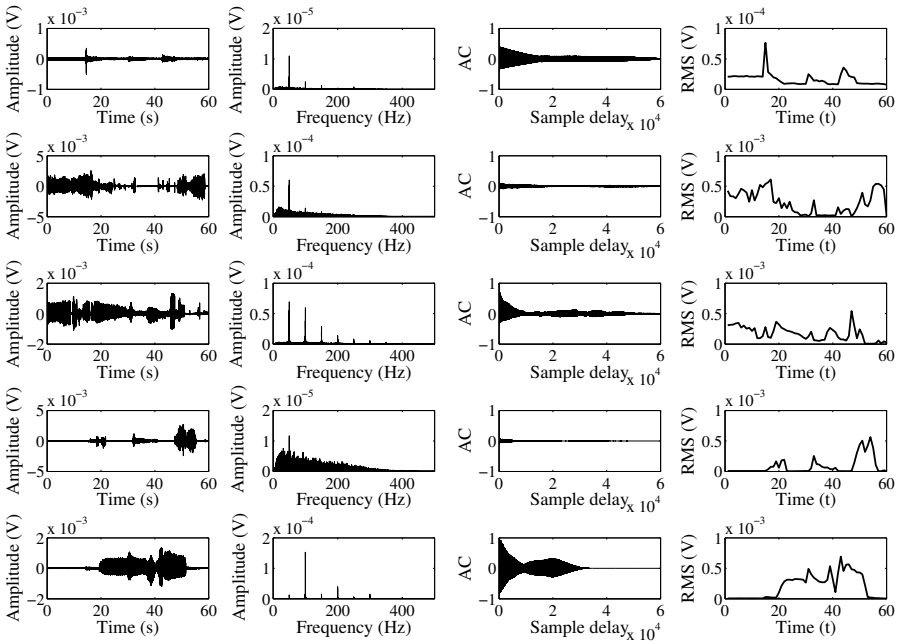

Figure 4.22: Probe D processed data. The first row from the top is showing the processed signal from 1-2, the second row from 1-3, the third from 2-3, fourth from 2-4 and fifth from 3-4. The first column from left is the filtered signal (30-500 Hz), the second column is the frequency spectrum of the signal, the third column is the autocorrelation of the signal and the fourth column is the RMS with a 1 s smoothing window. Very little SEMG signal is recorded. This may be attributed to the incomplete contact as large 50 Hz components are present and samples of signals have large autocorrelations.

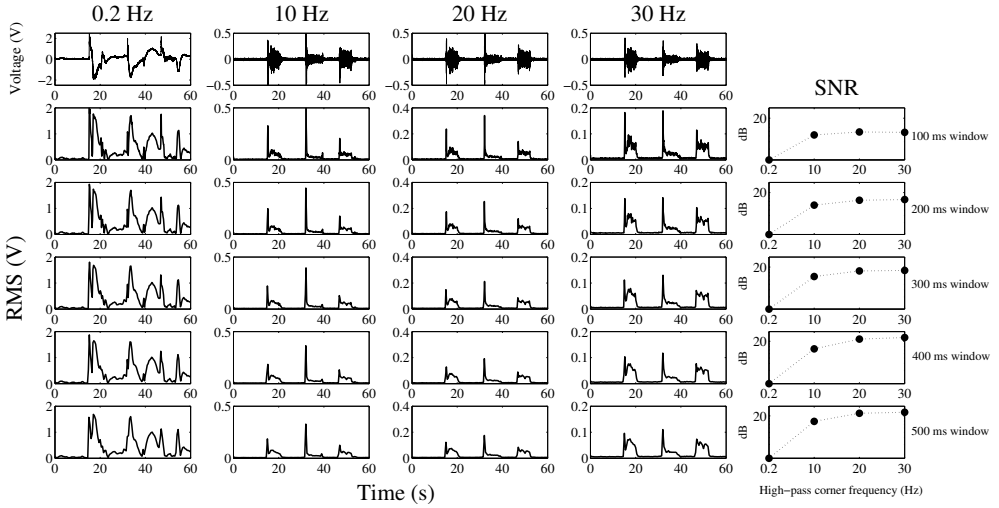

Figure 4.23: The effect of processing parameters on the recorded SEMG using Probe C 1-2 configuration. The first row from the top shows the the filtered signal at the indicated high-pass corner frequencies. The subsequent rows show the RMS using different smoothing windows while the column on the right compares the SNR at the said corners for the given smoothing window.

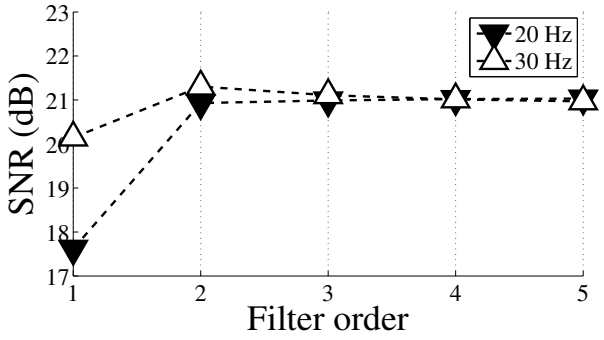

Figure 4.24: The effect of filter order on the SNR of the RMS amplitude estimate for 20 Hz and 30 Hz high-pass corner frequencies.

the SNR value was observed. Figure 4.24 shows the SNR for Butterworth filters of different orders for the RMS amplitude estimates with 500 ms smoothing windows for two high-pass corner frequencies. For both corner frequencies no improvement above a second order filter is observed. In addition, the filter with a 30 Hz corner frequency demonstrates a slight improvement.

4.4.3 Electrode tissue impedance

Figure 4.25 shows the impedance magnitude and phase of the electrodes *in situ* and those of the models across the measurement frequencies. Table 4.3 shows

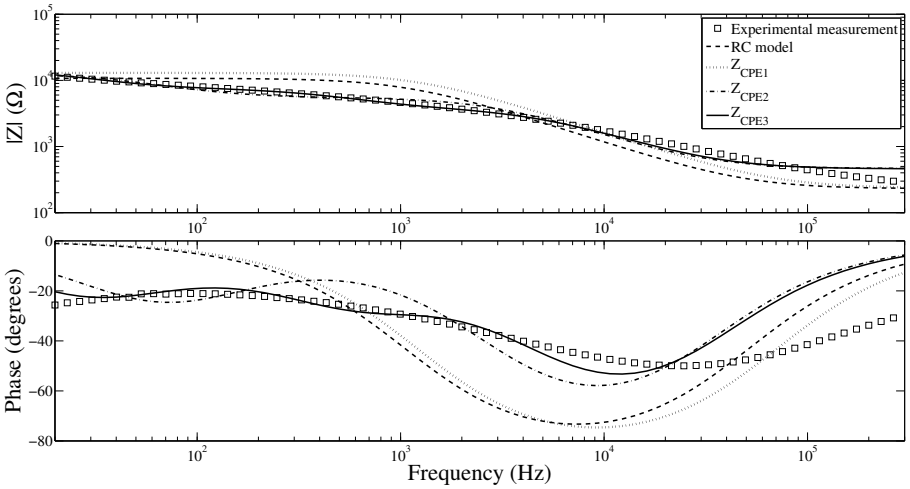

Figure 4.25: Experimental electrode tissue impedance and that of the corresponding models. Various model fits are shown. It is clear that a 3-stage ladder representing the Z_{CPE} yields the best fit within the frequencies of interest (20 Hz - 400 Hz).

Table 4.3: Coefficients for different models.

Coefficient	*RC*	Z_{CPE1}	Z_{CPE2}	Z_{CPE3}
R_t	230.8 Ω	235 Ω	234.7 Ω	238.4 Ω
R_{ct}	10513.2 Ω	12750 Ω	12284 Ω	14994.8 Ω
C_{dl}	14.03 nF	-	-	-
r_o	-	1 Ω	26.17 Ω	22.4 Ω
c_o	-	1 pF	1.3 pF	1.038 pF
r_1	-	-	9595.58 Ω	5085.86 Ω
c_1	-	-	15.249 pF	5.205 pF
r_2	-	-	-	11112.64 Ω
c_2	-	-	-	21.849 pF

all the values of the components based on Figure 4.25. It is clear that Z_{CPE3} fits the magnitude and phase data well within the operation frequencies of the SEMG apparatus. It is noted that the application of appropriate boundaries has resulted in the coefficients being of sensible values based on the nature of the electric components they represent.

4.5 Discussions

Experimental results

The signal recorded using large electrodes placed laterally (Probe A) with the internal reference electrode shows occurrence correlation with the muscular activity but the intensity of the muscular activity is not manifested in the recorded signal. Such a correlation is not visible when an external reference electrode is used. Thus, this raises doubts in the nature of the recorded signal using the internal reference electrode and its neutrality in terms of the recorded electrical activity. In both cases of the internal and external references, however, the signal is white.

An interesting feature observed when implementing 1 cm wide electrodes placed circumferentially all the way round the probe (Probe B) is the pronounced signal cancellation. This is most likely associated with the placement of the electrodes. As it was shown, such a cancellation is perceivable in case electrodes are placed not between an IZ and EZ pair. When electrodes make a sufficient contact with the tissue, the signals are white and no significant spectrum deformation is visible.

In Probe D, the electrodes either do not make a sufficient contact or the contact area is so small that a very weak signal is recorded. This shows that although under controlled conditions and using more polarisable electrodes the signal may be readily recorded with electrodes such as those in Probe D, however, this may not be possible with stainless steel electrodes and with no skin preparation and no conductive gel applied to the contact tissue.

The trade-off between practical considerations and theoretical calculations is clearly met when implementing Probe C. A double electrode spacing results in extraneous activities, possibly from other muscular structures, being recorded but the signal from adjacent electrodes are correlated with the muscular activity

completely and the signal is sufficiently white.

One of the major components which may vary across different subjects and affect the outcome of this pre-clinical study is the variation in the positions of the IZs and EZs. Variations in the other elements such as the depth of the EAS and the population of the fibres and MUs do not affect the design parameters considerably. The significance of the electrode position compared to other features can be observed from the data recorded from Probe B. Therefore, the same array of four electrodes as in Probe C can be used to account for the variation in the positions of the IZs and EZs in different subjects.

Signal processing

Apart from the mains noise which only manifests itself if the electrodes do not make a sufficient contact if the electronics are designed appropriately, the movement artefact is a serious source of noise. This may be rectified by having a relatively high high-pass corner frequency. However, the attenuation in the level of the recorded signal and the SNR of the RMS amplitude estimate should be considered. It was shown that using a 20 Hz corner frequency in a second order filter, a relatively high signal level is maintained with a relatively high SNR of the amplitude estimate.

It is important that the smoothing window is short enough to ensure that the variations of the muscular activity are followed and is large enough to ensure a reasonable SNR. Given that the frequency level of the target muscular activity is in the order of 1 Hz, a 500 ms window length results in an appropriate monitoring of muscular activities while maintaining a relatively high SNR.

Electrode tissue impedance

The set of experiments and analyses provided the specifications of a real time recording and processing apparatus. Furthermore, using the developed functional model of the electrode and tissue, it is possible to very accurately estimate the loading effect of the electrode-tissue interface in the frequencies of operation. For

the electrodes in the experiment, the impedance of the electrode and tissue range between 6 KΩ to 10 KΩ across the SEMG frequency range.

To model the electrodes separately, it is trivial to show that all the appropriate resistor values in the model (related to the electrode-tissue interface) should be halved and the capacitor values should be doubled to have a representation of the electrode tissue interface for two completely balanced electrodes. Any imbalance can then be manually exerted if such effects are to be tested in simulations. It is worth re-iterating that the developed model is merely a functional model in that values of the components may be different if they were to adopt the values consistent with the physiochemical effects they represent. In that case more stages of the Z_{CPE} ladder might have been required to fit the data.

4.6 Summary

After a brief introduction to the physiology of muscles in general, the underlying fundamentals of the EMG signal with particular attention to the SEMG were discussed. The functional models of the SEMG based on which many aspects of the SEMG have been investigated in the literature were mentioned to build an analytical understanding of the SEMG generation and recording.

Important issues regarding the recording apparatus were discussed. Namely, the effect of the electrode size and shape, the linear operation performed on the spatial samples of the signal and recording arrays in general were analysed. The main features of the amplitude estimation were described and their relation to the stochastic nature of the SEMG amplitude was analytically demonstrated.

On an issue immediately related to the target application described in this thesis, the existing studies on the EAS based on SEMG studies were reviewed.

Given the importance of loading effects of the electrode-tissue interface, ways to model such interfaces were analytically demonstrated. The methods to arrive at such models were described in detail based on the experimental measurements.

It was demonstrated that a model based on Z_{CPE} which is in turn modelled using three stages of an RC ladder can model the electrode tissue impedance within the frequencies of interest.

A set of probes with arrays of electrodes of different size and spacing were designed based on the theoretical analyses. They were tested methodically to identify an appropriate trade-off between the theoretical design and practical considerations. A specific electrode design was identified to adequately record the intended signal. Different features of the processing unit including the bandwidth, filter order and smoothing window size were also methodically identified. Therefore, the outcome of this chapter derived the necessary design parameters to have an optimally designed SEMG sensor to monitor the EAS activity as a proxy for the EUS.

Chapter 5

Conclusions & future directions

5.1 Introduction

The subsequent sections of this chapter conclude and summarise the narrative of the thesis while the possibilities for improvement and future directions are discussed.

5.2 An optimised design

The target solution, the conditional trans-rectal neuromodulation of the pudendal nerve using a wearable device, as presented in this thesis can greatly improve the QoL for SCI patients if proven clinically that it is safe, reliable and efficacious for a chronic use. Based on an extensive literature review the potentials of the solution were demonstrated. The particular merits of the solution are its non-invasive nature and the fact that it may be implemented to recover a full bladder function after SCI, for which no single solution exists.

Optimised conditional neuromodulation

One of the major impediments in the chronic implementation of the trans-rectal pudendal nerve neuromodulation is the high levels of current involved. The computational modelling study presented in this thesis aimed to address this issue. The findings of the hybrid-modelling studies suggest that by re-positioning the

stimulation electrodes on the surface of the probe, the required stimulus current may be reduced considerably. This can enhance the safety of the device while making it more efficacious. As per the recording electrodes, the thorough theoretical and experimental studies presented, may ensure a reliable chronic EAS SEMG amplitude estimation is performed to carry out the conditional neuromodulation of the pudendal nerve.

The device body shape

It was mentioned in Chapter 2 that ano-rectal stimulators are generally used acutely and for therapeutic purposes. Thus, their body shape are usually not designed to be held in place for an extended period of time. Rather, the shape of such probes are designed in a way to ensure electrodes, which are generally relatively large, are held in specific locations. The study by Hopkinson and Lightwood [74], as referred to in Chapter 2, demonstrated the need for various probe sizes by moulding the anal canal of a group of subjects. Their probes were intended for the stimulation of muscular structures but they envisaged a prolonged use. This led to the design of a series of probes which had a bulb-shaped head and a cylindrical body. They also reported the ability of the subjects in holding the probes *in situ*. They proposed to devise a narrowed section at the position of the ano-rectal junction to control the degree of the widening towards the rectum (30°) and the degree of broadening back towards the anal canal (10°). The study by Brindley *et al.* [72], also referred to in Chapter 2, perhaps was the first to consider the concept of the trans-rectal pudendal nerve neuromodulation using a relatively elongated probe. This idea is particularly interesting as it may eliminate the need for various probe shapes and sizes by pushing the wider section of the probe to the verge of the rectal opening. The device used by Craggs *et al.* [8, 73] followed a similar shape. Thus, general anatomical considerations for average feature sizes should be considered to design an optimised prototype at

this stage.

The design considerations form the tail to the tip of the device may be summarised as follows although more extensive studies on anatomical variations should be performed. The details of the probe design in the study by Craggs *et al.* [8] may be found in [73]. Glen proposed [245] the placement of an anchor shape barrier at the tail of anorectal probes to avoid an inadvertent complete insertion of the probe. It has also been proposed that an isthmus should be placed between the anchor and the widening of such probes to allow the closure of the anal orifice. This isthmus should be no more than 5 mm in diameter [8, 73]. It was concluded in Chapter 4 that the recording electrodes should be placed 1 cm deep into the anal canal. The diameter of the recording compartment may be about 1.8 cm based on the data presented in Chapter 4 and it can have a uniform thickness as no visible curvature was observed in the MRI study shown in Chapter 3.

The length of the surgical anal canal defined as the distance between the anorectal ring to anal verge is on average 4.2 cm, ranging from 3 cm to 5.3 cm (n=211) [246]. This is roughly where the body of the probe should be widening towards its tip. This way the anodes can be placed on the widest segment of the device, about 6 cm deep into the canal to be pushed towards the pudendal nerve and also hold the device in place. The stimulation compartment of the device may be designed like an ellipsoid for an improved insertability. The device at its widest, where the anodes are, should be no more that 3 cm as suggested by Hopkinson and Lightwood [74]. Thus, the widening on the anode side may be about 3 cm while in the direction of the cathode it may be 2 cm, similar to the models in Chapter 3. This description of the design is similar to that implemented by Craggs *et al.* [8] apart from the design of the SEMG compartment. The wider SEMG compartment has two benefits: one is to make the overall body of the device more robust and the other is that more space is available inside the probe in case the future integrations of electronics and batteries are intended. The possible issue with this design is that the body of the device may push and rub against the

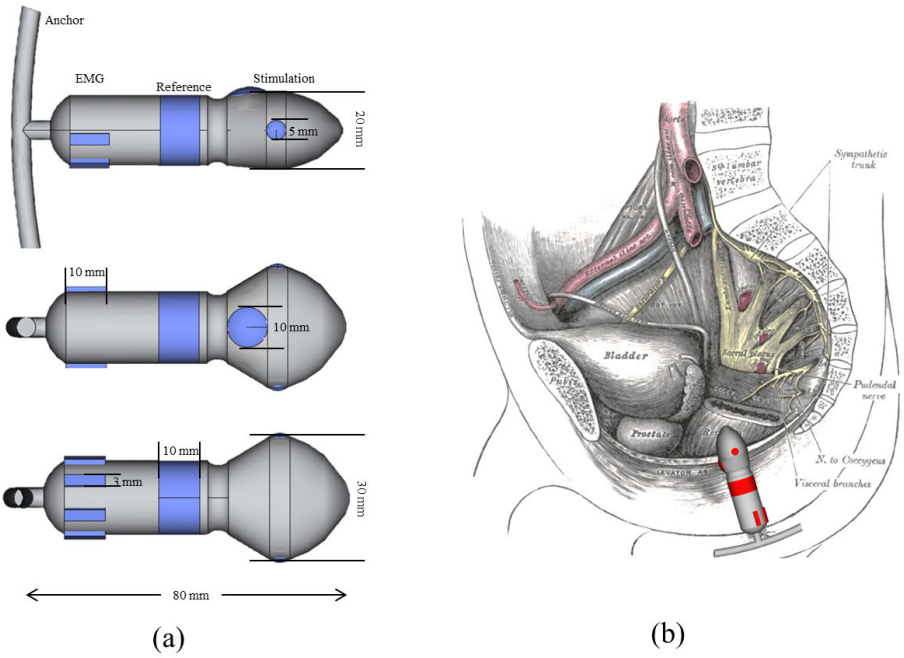

Figure 5.1: Drawings of the proposed optimised design. (a) shows different dimensions of the design while (b) is an schematic view of the probe *in situ*. In (b) drawings from [12] were used.

surface of the anal canal which should be tested in the subsequent stages of the development. Based on the work presented in this thesis and the abovementioned considerations, the optimised design presented in Figure 5.1 is proposed. Based on the information in Chapter 4, using an array of SEMG recording electrodes, variations in the positions of IZs and EZs can be accounted for in different individuals. The stimulation electrodes are optimally positioned to reduce the required stimulus current as presented in Chapter 3.

Given the presented reviews, studies and discussions, the remainder of this chapter summarises the achievements of the thesis and possible future directions as related to every chapter.

5.3 Fundamentals of the design

Mid-frequency stimulation

It should be noted that the effects of the mid-frequency trans-rectal neuromodulation of the pudendal nerve have not been tested. Therefore, a great research potential lies in the clinical evaluation of the mid-frequency trans-rectal neuromodulation of the pudendal nerve using the optimised device. Such a study should consider the voiding efficiencies and the effects of shifting from the low-frequencies to mid-frequencies to switch from the storage mode to the voiding mode.

Absence of DSD

In the absence of the DSD, the solution may not be able to use the activities of the EAS to detect the onset of hyperreflexive contractions. Thus, a conditional neuromodulation may not be possible. In that case other materials and methods should be used for a conditional neuromodulation [247].

Combined with other treatments

It was mentioned that other relatively conservative treatment and management techniques include drugs and catheterisation. The solution should be evaluated and compared based on features such as the bladder capacity and voiding efficiency with the said solutions. It should also be considered that the solution may be used in tandem with other solutions.

Therapeutic use

Various studies as also mentioned in Chapter 2 have investigated the acute and therapeutic use of the pudendal nerve stimulation. This changes the mode of usage from a device for a chronic control of the LUT to a solution used for a limited period of time during the day for an improved function of different elements of the LUT. Still, the value of the optimised design is that it requires a current level below the pain threshold of sensate individuals.

Other patient groups

Similar conditions exist in different patient groups with neurologic damage or disease such as multiple sclerosis. This solution may be applied in all similar conditions and further research may be performed on the applicability of this solution in those cases.

5.4 Stimulation compartment design

It was pointed out that the major limiting factor of the trans-rectal neuromodulation of the pudendal nerve is the high levels of the required stimulus current. Levels as high as 100 mA of the applied stimulus current have been reported. Using state of the art computational models, a novel configuration of electrodes for the trans-rectal neuromodulation of the pudendal nerve was proposed. The modelling shows that even when different variations of the pudendal nerve in different individuals and in a same individual in different body postures are considered a specific configuration requires a considerably lower stimulus current level to activate the pudendal nerve. This is a major achievement and if proven clinically can transform the trans-rectal neuromodulation of the pudendal nerve into a viable solution.

The steps in forming the model presented in Chapter 3 involved an *in vivo* conductivity test using a test trans-rectal stimulator, a set of MRI scans to form a 3D understanding of the pelvic region with the device *in situ*, forming an FEM model, generating random fibre distributions and implementing a mammalian fibre model. The validity of the model was tested by considering the approximations made and their effects on the conclusions drawn. The model can be retrospectively verified as the thresholds shown for the pudendal nerve neuromodulation are consistent with those reported in the literature. The MRG model shows slightly higher thresholds and if the results are adjusted to account for that the thresholds are in the region reported in the literature.

5.4.1 MRI study and 3D model

Deriving a 3D model directly from MRI studies can generate a more realistic 3D model. Different image processing methods and tools may be applied to distinguish different layers in the MRI. By selecting points in different sagittal planes and subsequently interpolating those points, the 3D model is formed that can be discretised for the subsequent FEM studies. Also, a more anisotropic definition of conductivities may be used. The shortcoming of such a method is that it may generate an extremely complex 3D model that cannot be solved using the available computational power.

5.4.2 Frequency dependent components

Although the validity of the quasi-static approximation in the model and the subsequent presented study was demonstrated, a more realistic model, taking into account the frequency dependent response of the electrode-tissue contact and different tissue layers may be beneficial in predicting the actual thresholds for a given configuration. A complete electrode model is especially important if the response to a voltage-controlled stimulation is to be modelled.

5.4.3 Numerical methods

The FEM was used to discretise and solve the underlying differential equations. A comparison of the solutions in the FVM and FEM are of great interest in a field that predominantly the workers use FEM.

5.4.4 Fibre model

A well-established fibre model was used in this study but various other models also exist. A comparison of the results from these models in the case of the trans-rectal pudendal nerve neuromodulation may be of interest.

It was mentioned that the MRG model shows an elevated threshold of excitation. It may be also of interest to determine the features of the model which result

in this elevated threshold. In a similar fashion the parameters may be adjusted to clearly distinguish between afferent and efferent fibres in the nerve although within the pulse widths of interest the difference is minute.

5.4.5 Electrode material

The role of the electrode material has been extensively investigated in various electrical stimulation applications. Stainless steel was chosen as the material of choice at this stage of the development due to its availability and mechanical properties. Other choices may be investigated if need be at the later stages of the development.

5.5 SEMG compartment design

By means of a thorough theoretical analysis, a comprehensive literature review and experimental measurements a feasible design for the SEMG recording from the EAS was proposed. This design is the compromise between the theoretical design and practical feasibility. The limiting factor of the chronic EAS SEMG recording is that the device should produce an acceptable EMG signal, correlated with the muscular activity without any skin preparation or the application of any conductive gel. From the four prototypes tested, only one showed a high quality SEMG signal consistent with the prompted muscular activity.

A novel method was also developed to model the electrode-tissue conductivity using Z_{CPE}. This model was applied to the experimental measurements of a set of electrodes *in situ*. Any subsequent study on the effect of the electrode-tissue impedance may use such models while introducing imbalance.

5.5.1 Electrode models and material

Using the developed electrode-tissue model, it is possible to study various choices of the material by modelling them in the frequency band of interest. At this stage of the development stainless steel electrodes were used. However, it should be

investigated via experiments how the choice of different electrodes or electrode surface rendering techniques may affect the recorded signal.

5.6 An optimised prototype

5.6.1 Making the probe

The making of the optimised prototype requires a thorough evaluation of the limits of the required trade-offs in terms of the need for implementing a specific design and the manufacturability of the said design. Figure 5.2 shows an attempt[1] in realising the design shown in Figure 5.1. A great amount of research may be carried out on the materials and methods of making the prototype such as the body and electrode material. For the specific attempt shown in Figure 5.2 a medical grade silicone was used and the electrodes were made out of stainless steel. The moulds and electrode holders were 3D printed out of Verowhite material. Similar to the study in [74] a great research interest lies in analysing the size variations required for such a device.

5.6.2 The electronics

A block diagram of the typical modules in a required portable device for performing the clinical tests is shown in Figure 5.3. The modules involve an AC coupling stage followed by a preamplifier. After bandpassing the signal, a secondary gain stage with a programmable gain is devised. The RMS detection, communication with a command unit and the control of the stimulus amplitude and parameters can be done digitally.

Upon deriving the specifications and validating the results of the thesis, it is possible to integrate the required electronics to make a fully active probe, in which case the method of making the prototype should be revised to make space for the electronics and the battery inside.

[1]The device was made in collaboration with Dr Sandy Mosse and Dr Daniil Nikitichev at UCL Medical Physics and Biomedical Engineering Department.

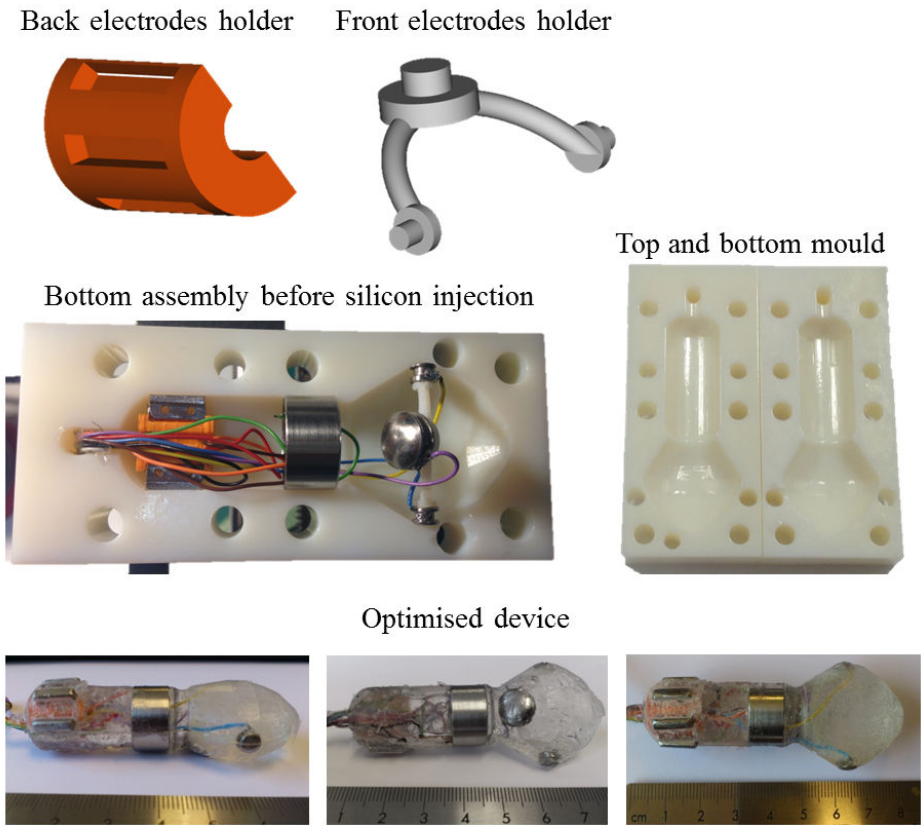

Figure 5.2: The making of the optimised probe. From top to bottom, the structure designed to hold the electrodes in place, the 3D printed moulds, the mould populated with the wired electrodes and the optimised prototype are shown.

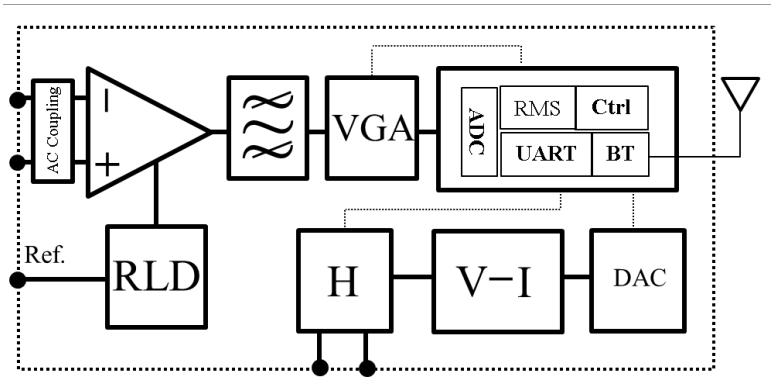

Figure 5.3: The block diagram of the electronics required to perform the clinical tests.

Bibliography

[1] National-Spinal-Cord-Injury-Statistical-Center, "Spinal cord injury facts and figures at a glance," *The Journal of Spinal Cord Medicine*, vol. 37, no. 4, pp. 479–480, 2014.

[2] B. Lee, R. Cripps, M. Fitzharris, and P. Wing, "The global map for traumatic spinal cord injury epidemiology: update 2011, global incidence rate," *Spinal cord*, vol. 52, no. 2, pp. 110–116, 2014.

[3] R. A. Gaunt and A. Prochazka, "Control of urinary bladder function with devices: successes and failures," *Progress in brain research*, vol. 152, pp. 163–194, 2006.

[4] K. D. Anderson, "Targeting recovery: priorities of the spinal cord-injured population," *Journal of neurotrauma*, vol. 21, no. 10, pp. 1371–1383, 2004.

[5] J. Corcos and E. Schick, *Textbook of the neurogenic bladder*. Informa Healthcare, 2008.

[6] P. Sanders, M. Ijzerman, M. Roach, and K. Gustafson, "Patient preferences for next generation neural prostheses to restore bladder function," *Spinal Cord*, vol. 49, no. 1, pp. 113–119, 2011.

[7] D. B. Vodusek, J. K. Light, and J. M. Libby, "Detrusor inhibition induced by stimulation of pudendal nerve afferents," *Neurourology and urodynamics*, vol. 5, no. 4, pp. 381–389, 1986.

[8] M. Craggs, N. Edirisinghe, B. Leaker, J. Susser, M. Al-Mukhtar, and N. Donaldson, "Conditional neuromodulation using trans-rectal stimulation in spinal cord injury," 2009.

[9] D. Purves, G. J. Augustine, D. Fitzpatrick, W. C. Hall, A.-S. LaMantia, J. O. McNamara, and L. E. White, "Neuroscience. 4th," *Sunderland, MA: Sinauer Associates*, 2007.

[10] E. R. Kandel, J. H. Schwartz, T. M. Jessell *et al.*, *Principles of neural science*. McGraw-Hill New York, 2000, vol. 4.

[11] G. Paxinos and J. K. Mai, *The human nervous system*. Academic Press, 2004.

[12] H. Gray, *Anatomy of the human body*. Lea & Febiger, 1918.

[13] F. H. Netter, *Atlas of human anatomy*. Elsevier Health Sciences, 2014.

[14] R. Carpenter and B. Reddi, *Neurophysiology: A Conceptual Approach*. CRC Press, 2012.

[15] W. F. Pickard, "Generalizations of the goldman-hodgkin-katz equation," *Mathematical Biosciences*, vol. 30, no. 1, pp. 99–111, 1976.

[16] A. L. Hodgkin and A. F. Huxley, "A quantitative description of membrane current and its application to conduction and excitation in nerve," *The Journal of physiology*, vol. 117, no. 4, pp. 500–544, 1952.

[17] C. C. McIntyre, A. G. Richardson, and W. M. Grill, "Modeling the excitability of mammalian nerve fibers: influence of afterpotentials on the recovery cycle," *Journal of neurophysiology*, vol. 87, no. 2, pp. 995–1006, 2002.

[18] J. Malmivuo and R. Plonsey, *Bioelectromagnetism: principles and applications of bioelectric and biomagnetic fields*. Oxford University Press, USA, 1995.

[19] P. Abrams, J. G. Blaivas, S. L. Stanton, and J. T. Andersen, "Standardisation of terminology of lower urinary tract function," *Neurourology and Urodynamics*, vol. 7, no. 5, pp. 403–427, 1988.

[20] C. J. Fowler, D. Griffiths, and W. C. de Groat, "The neural control of micturition," *Nature Reviews Neuroscience*, vol. 9, no. 6, pp. 453–466, 2008.

[21] W. C. de Groat, D. Griffiths, and N. Yoshimura, "Neural control of the lower urinary tract," *Comprehensive Physiology*, 2015.

[22] A. Kanai and K.-E. Andersson, "Bladder afferent signaling: recent findings," *The Journal of urology*, vol. 183, no. 4, pp. 1288–1295, 2010.

[23] W. De Groat, "Nervous control of the urinary bladder of the cat," *Brain research*, vol. 87, no. 2-3, pp. 201–211, 1975.

[24] ——, "Inhibitory mechanisms in the sacral reflex pathways to the urinary bladder," *Iontophoresis and transmitter mechanisms in the mammalian central nervous system*, pp. 366–368, 1978.

[25] W. De Groat, A. Booth, R. Milne, and J. Roppolo, "Parasympathetic preganglionic neurons in the sacral spinal cord," *Journal of the autonomic nervous system*, vol. 5, no. 1, pp. 23–43, 1982.

[26] W. C. de Groat, M. O. Fraser, M. Yoshiyama, S. Smerin, C. Tai, M. B. Chancellor, N. Yoshimura, and J. R. Roppolo, "Neural control of the urethra," *Scandinavian Journal of Urology and Nephrology*, vol. 35, no. 207, pp. 35–43, 2001.

[27] J. P. Woock, P. B. Yoo, and W. M. Grill, "Finite element modeling and in vivo analysis of electrode configurations for selective stimulation of pudendal afferent fibers," *BMC urology*, vol. 10, no. 1, p. 11, 2010.

[28] F. M. Maynard, M. B. Bracken, G. Creasey, J. Ditunno, W. H. Donovan, T. B. Ducker, S. L. Garber, R. J. Marino, S. L. Stover, C. H. Tator *et al.*, "International standards for neurological and functional classification of spinal cord injury," *Spinal cord*, vol. 35, no. 5, pp. 266–274, 1997.

[29] M. J. McGee, C. L. Amundsen, and W. M. Grill, "Electrical stimulation for the treatment of lower urinary tract dysfunction after spinal cord injury," *The journal of spinal cord medicine*, vol. 38, no. 2, pp. 135–146, 2015.

[30] K. J. Weld and R. R. Dmochowski, "Association of level of injury and bladder behavior in patients with post-traumatic spinal cord injury," *Urology*, vol. 55, no. 4, pp. 490–494, 2000.

[31] A. Reitz, M. Stöhrer, G. Kramer, G. Del Popolo, E. Chartier-Kastler, J. Pannek, H. Burgdörfer, K. Göcking, H. Madersbacher, S. Schumacher *et al.*, "European experience of 200 cases treated with botulinum-a toxin injections into the detrusor muscle for urinary incontinence due to neurogenic detrusor overactivity," *European urology*, vol. 45, no. 4, pp. 510–515, 2004.

[32] G. Brindley, "The first 500 patients with sacral anterior root stimulator implants: general description," *Spinal Cord*, vol. 32, no. 12, pp. 795–805, 1994.

[33] M. Spinelli and K.-D. Sievert, "Latest technologic and surgical developments in using interstim therapy for sacral neuromodulation: impact on treatment success and safety," *European urology*, vol. 54, no. 6, pp. 1287–1296, 2008.

[34] K. J. Gustafson, P. F. Zelkovic, A. H. Feng, C. E. Draper, D. R. Bodner, and W. M. Grill, "Fascicular anatomy and surgical access of the human pudendal nerve," *World journal of urology*, vol. 23, no. 6, pp. 411–418, 2005.

[35] P. Mahakkanukrauh, P. Surin, and P. Vaidhayakarn, "Anatomical study of the pudendal nerve adjacent to the sacrospinous ligament," *Clinical Anatomy*, vol. 18, no. 3, pp. 200–205, 2005.

[36] A. Shafik, M. El-Sherif, A. Youssef, and E.-S. Olfat, "Surgical anatomy of the pudendal nerve and its clinical implications," *Clinical anatomy*, vol. 8, no. 2, pp. 110–115, 1995.

[37] P. Kovacs, H. Gruber, J. Piegger, and G. Bodner, "New, simple, ultrasound-guided infiltration of the pudendal nerve," *Diseases of the colon & rectum*, vol. 44, no. 9, pp. 1381–1385, 2001.

[38] M. Schenck, C. Schenck, H. Rübben, M. Stuschke, T. Schneider, A. Eisenhardt, and R. Rossi, "Pudendal nerve block in hdr-brachytherapy patients: do we really need general or regional anesthesia?" *World journal of urology*, vol. 31, no. 2, pp. 417–421, 2013.

[39] D. B. Vodušek, S. Plevnik, P. Vrtačnik, and J. Janež, "Detrusor inhibition on selective pudendal nerve stimulation in the perineum," *Neurourology and Urodynamics*, vol. 6, no. 5, pp. 389–393, 1987.

[40] J. Previnaire, J. Soler, M. Perrigot, G. Boileau, H. Delahaye, P. Schumacker, J. Vanvelcenaher, and J. Vanhee, "Short-term effect of pudendal nerve electrical stimulation on detrusor hyperreflexia in spinal cord injury patients: importance of current strength," *Spinal Cord*, vol. 34, no. 2, pp. 95–99, 1996.

[41] S. J. Shefchyk and R. Buss, "Urethral pudendal afferent-evoked bladder and sphincter reflexes in decerebrate and acute spinal cats," *Neuroscience letters*, vol. 244, no. 3, pp. 137–140, 1998.

[42] J. Previnaire, J. Soler, and M. Perrigot, "Is there a place for pudendal nerve maximal electrical stimulation for the treatment of detrusor hyperreflexia in spinal cord injury patients?" *Spinal Cord*, vol. 36, no. 2, pp. 100–103, 1998.

[43] A. Kirkham, N. Shah, S. Knight, P. Shah, and M. Craggs, "The acute effects of continuous and conditional neuromodulation on the bladder in spinal cord injury." *Spinal Cord*, vol. 39, no. 8, pp. 420–428, 2001.

[44] Y.-H. Lee and G. H. Creasey, "Self-controlled dorsal penile nerve stimulation to inhibit bladder hyperreflexia in incomplete spinal cord injury: a case report," *Archives of physical medicine and rehabilitation*, vol. 83, no. 2, pp. 273–277, 2002.

[45] J. W. Boggs, B. J. Wenzel, K. J. Gustafson, and W. M. Grill, "Spinal micturition reflex mediated by afferents in the deep perineal nerve," *Journal of neurophysiology*, vol. 93, no. 5, pp. 2688–2697, 2005.

[46] K. M. Peters, K. M. Feber, and R. C. Bennett, "Sacral versus pudendal nerve stimulation for voiding dysfunction: A prospective, single-blinded, randomized, crossover trial," *Neurourology and urodynamics*, vol. 24, no. 7, pp. 643–647, 2005.

[47] M. Spinelli, S. Malaguti, G. Giardiello, M. Lazzeri, J. Tarantola, and U. V. D. Hombergh, "A new minimally invasive procedure for pudendal nerve stimulation to treat neurogenic bladder: description of the method and preliminary data," *Neurourology and urodynamics*, vol. 24, no. 4, pp. 305–309, 2005.

[48] J. W. Boggs, B. J. Wenzel, K. J. Gustafson, and W. M. Grill, "Frequency-dependent selection of reflexes by pudendal afferents in the cat," *The Journal of physiology*, vol. 577, no. 1, pp. 115–126, 2006.

[49] ——, "Bladder emptying by intermittent electrical stimulation of the pudendal nerve," *Journal of neural engineering*, vol. 3, no. 1, p. 43, 2006.

[50] C. Tai, S. E. Smerin, W. C. de Groat, and J. R. Roppolo, "Pudendal-to-bladder reflex in chronic spinal-cord-injured cats," *Experimental neurology*, vol. 197, no. 1, pp. 225–234, 2006.

[51] C. Tai, J. Wang, X. Wang, J. R. Roppolo, and W. C. de Groat, "Voiding reflex in chronic spinal cord injured cats induced by stimulating and blocking pudendal nerves," *Neurourology and urodynamics*, vol. 26, no. 6, pp. 879–886, 2007.

[52] P. B. Yoo, S. M. Klein, N. H. Grafstein, E. E. Horvath, C. L. Amundsen, G. D. Webster, and W. M. Grill, "Pudendal nerve stimulation evokes reflex bladder contractions in persons with chronic spinal cord injury," *Neurourology and urodynamics*, vol. 26, no. 7, pp. 1020–1023, 2007.

[53] P. B. Yoo and W. M. Grill, "Minimally-invasive electrical stimulation of the pudendal nerve: A pre-clinical study for neural control of the lower urinary tract," *Neurourology and urodynamics*, vol. 26, no. 4, pp. 562–569, 2007.

[54] T. M. Bruns, N. Bhadra, and K. J. Gustafson, "Variable patterned pudendal nerve stimuli improves reflex bladder activation," *Neural Systems and Rehabilitation Engineering, IEEE Transactions on*, vol. 16, no. 2, pp. 140–148, 2008.

[55] P. B. Yoo, J. P. Woock, and W. M. Grill, "Bladder activation by selective stimulation of pudendal nerve afferents in the cat," *Experimental neurology*, vol. 212, no. 1, pp. 218–225, 2008.

[56] C.-W. Peng, J.-J. J. Chen, C.-L. Cheng, and W. M. Grill, "Improved bladder emptying in urinary retention by electrical stimulation of pudendal afferents," *Journal of neural engineering*, vol. 5, no. 2, p. 144, 2008.

[57] J. P. Woock, P. B. Yoo, and W. M. Grill, "Activation and inhibition of the micturition reflex by penile afferents in the cat," *American Journal of Physiology-Regulatory, Integrative and Comparative Physiology*, vol. 294, no. 6, pp. R1880–R1889, 2008.

[58] ——, "Intraurethral stimulation evokes bladder responses via 2 distinct reflex pathways," *The Journal of urology*, vol. 182, no. 1, pp. 366–373, 2009.

[59] E. E. Horvath, P. B. Yoo, C. L. Amundsen, G. D. Webster, and W. M. Grill, "Conditional and continuous electrical stimulation increase cystometric capacity in persons with spinal cord injury," *Neurourology and urodynamics*, vol. 29, no. 3, pp. 401–407, 2010.

[60] M. J. Kennelly, K. C. Arena, N. Shaffer, M. E. Bennett, W. M. Grill, J. H. Grill, and J. W. Boggs, "Electrical stimulation of the urethra evokes bladder contractions in a woman with spinal cord injury," *The journal of spinal cord medicine*, vol. 33, no. 3, p. 261, 2010.

[61] C. Tai, B. Shen, J. Wang, H. Liu, J. Subbaroyan, J. R. Roppolo, and W. C. de Groat, "Inhibition of bladder overactivity by stimulation of feline pudendal nerve using transdermal amplitude-modulated signal (tams)," *BJU international*, vol. 109, no. 5, pp. 782–787, 2012.

[62] P. B. Yoo, E. E. Horvath, C. L. Amundsen, G. D. Webster, and W. M. Grill, "Multiple pudendal sensory pathways reflexly modulate bladder and urethral activity in patients with spinal cord injury," *The Journal of urology*, vol. 185, no. 2, pp. 737–743, 2011.

[63] S.-C. Chen, W. M. Grill, W.-J. Fan, Y. R. Kou, Y. S. Lin, C.-H. Lai, and C.-W. Peng, "Bilateral pudendal afferent stimulation improves bladder emptying in rats with urinary retention," *BJU international*, vol. 109, no. 7, pp. 1051–1058, 2012.

[64] M. J. Kennelly, M. E. Bennett, W. M. Grill, J. H. Grill, and J. W. Boggs, "Electrical stimulation of the urethra evokes bladder contractions and emptying in spinal cord injury men: Case studies," *The journal of spinal cord medicine*, vol. 34, no. 3, pp. 315–321, 2011.

[65] A. Snellings and W. M. Grill, "Effects of stimulation site and stimulation parameters on bladder inhibition by electrical nerve stimulation," *BJU international*, vol. 110, no. 1, pp. 136–143, 2012.

[66] G. Yang, J. Wang, B. Shen, J. R. Roppolo, W. C. Groat, and C. Tai, "Pudendal nerve stimulation and block by a wireless-controlled implantable stimulator in cats," *Neuromodulation: Technology at the Neural Interface*, vol. 17, no. 5, pp. 490–496, 2014.

[67] M. J. McGee and W. M. Grill, "Selective co-stimulation of pudendal afferents enhances bladder activation and improves voiding efficiency," *Neurourology and urodynamics*, vol. 33, no. 8, pp. 1272–1278, 2014.

[68] ——, "Temporal pattern of stimulation modulates reflex bladder activation by pudendal nerve stimulation," *Neurourology and urodynamics*, 2015.

[69] M. Craggs, "Neuromodulation device for pelvic dysfunction," Feb. 4 2014, uS Patent 8,644,938.

[70] A. Shiraz, M. Craggs, B. Leaker, and A. Demosthenous, "Minimizing stimulus current in a wearable pudendal nerve stimulator using computational models," *Neural Systems and Rehabilitation Engineering, IEEE Transactions on, in press*.

[71] R. P. Fravel and C. J. Godec, "Urinary incontinence stimulator system," May 8 1979, uS Patent 4,153,059.

[72] G. Brindley, D. Rushton, and M. Craggs, "The pressure exerted by the external sphincter of the urethra when its motor nerve fibres are stimulated electrically," *British journal of urology*, vol. 46, no. 4, pp. 453–462, 1974.

[73] N. A. Edirisinghe, "A novel wearable electronic device for treating neurogenic detrusor overactivity by conditional neuromodulation," Ph.D. dissertation, UCL (University College London), 2011.

[74] B. Hopkinson and R. Lightwood, "Electrical treatment of incontinence," *British Journal of Surgery*, vol. 54, no. 9, pp. 802–805, 1967.

[75] B. J. Wenzel, J. W. Boggs, K. J. Gustafson, and W. M. Grill, "Detecting the onset of hyper-reflexive bladder contractions from the electrical activity of the pudendal nerve," *Neural Systems and Rehabilitation Engineering, IEEE Transactions on*, vol. 13, no. 3, pp. 428–435, 2005.

[76] B. J. Wenzel, J. W. Boggs, K. J. Gustafson, G. H. Creasey, and W. M. Grill, "Detection of neurogenic detrusor contractions from the activity of the external anal sphincter in cat and human," *Neurourology and urodynamics*, vol. 25, no. 2, pp. 140–147, 2006.

[77] J. W. Moore and K. S. Cole, "Voltage clamp techniques," *Physical techniques in biological research*, vol. 6, no. Part B, 1963.

[78] C. Koch, "Cable theory in neurons with active, linearized membranes," *Biological cybernetics*, vol. 50, no. 1, pp. 15–33, 1984.

[79] A. Richardson, C. McIntyre, and W. Grill, "Modelling the effects of electric fields on nerve fibres: influence of the myelin sheath," *Medical and Biological Engineering and Computing*, vol. 38, no. 4, pp. 438–446, 2000.

[80] D. R. McNeal, "Analysis of a model for excitation of myelinated nerve," *Biomedical Engineering, IEEE Transactions on*, no. 4, pp. 329–337, 1976.

[81] J. Sweeney, J. Mortimer, and D. Durand, "Modeling of mammalian myelinated nerve for functional neuromuscular stimulation," in *IEEE 9th Annual Conference of the Engineering in Medicine and Biology Society*, vol. 3, 1987, pp. 1577–1578.

[82] J. H. Frijns, J. Mooij, and J. H. Ten Kate, "A quantitative approach to modeling mammalian myelinated nerve fibers for electrical prosthesis design," *Biomedical Engineering, IEEE Transactions on*, vol. 41, no. 6, pp. 556–566, 1994.

[83] J. Frijns and J. Ten Kate, "A model of myelinated nerve fibres for electrical prosthesis design," *Medical and Biological Engineering and Computing*, vol. 32, no. 4, pp. 391–398, 1994.

[84] S. Raspopovic, M. Capogrosso, and S. Micera, "A computational model for the stimulation of rat sciatic nerve using a transverse intrafascicular multichannel electrode," *Neural Systems and Rehabilitation Engineering, IEEE Transactions on*, vol. 19, no. 4, pp. 333–344, 2011.

[85] A. R. Kent and W. M. Grill, "Model-based analysis and design of nerve cuff electrodes for restoring bladder function by selective stimulation of the pudendal nerve," *Journal of neural engineering*, vol. 10, no. 3, p. 036010, 2013.

[86] A. Huxley and R. Stämpeli, "Evidence for saltatory conduction in peripheral myelinated nerve fibres," *The Journal of physiology*, vol. 108, no. 3, pp. 315–339, 1949.

[87] I. Tasaki, "New measurements of the capacity and the resistance of the myelin sheath and the nodal membrane of the isolated frog nerve fiber," *Am J Physiol*, vol. 181, no. 3, pp. 639–650, 1955.

[88] R. Fitzhugh, "Computation of impulse initiation and saltatory conduction in a myelinated nerve fiber," *Biophysical journal*, vol. 2, no. 1, p. 11, 1962.

[89] L. Goldman and J. S. Albus, "Computation of impulse conduction in myelinated fibers; theoretical basis of the velocity-diameter relation," *Biophysical journal*, vol. 8, no. 5, p. 596, 1968.

[90] J. W. Moore, R. W. Joyner, M. H. Brill, S. D. Waxman, and M. Najar-Joa, "Simulations of conduction in uniform myelinated fibers. relative sensitivity to changes in nodal and internodal parameters," *Biophysical journal*, vol. 21, no. 2, pp. 147–160, 1978.

[91] J. Rubinstein, "Analytical theory for extracellular electrical stimulation of nerve with focal electrodes. ii. passive myelinated axon." *Biophysical journal*, vol. 60, no. 3, p. 538, 1991.

[92] M. Capogrosso, N. Wenger, S. Raspopovic, P. Musienko, J. Beauparlant, L. B. Luciani, G. Courtine, and S. Micera, "A computational model for epidural electrical stimulation of spinal sensorimotor circuits," *The Journal of Neuroscience*, vol. 33, no. 49, pp. 19 326–19 340, 2013.

[93] E. F. Barrett and J. N. Barrett, "Intracellular recording from vertebrate myelinated axons: mechanism of the depolarizing afterpotential," *The Journal of Physiology*, vol. 323, no. 1, pp. 117–144, 1982.

[94] A. Blight and S. Someya, "Depolarizing afterpotentials in myelinated axons of mammalian spinal cord," *Neuroscience*, vol. 15, no. 1, pp. 1–12, 1985.

[95] A. Blight, "Computer simulation of action potentials and afterpotentials in mammalian myelinated axons: the case for a lower resistance myelin sheath," *Neuroscience*, vol. 15, no. 1, pp. 13–31, 1985.

[96] J. A. Halter and J. Clark, "A distributed-parameter model of the myelinated nerve fiber," *Journal of theoretical biology*, vol. 148, no. 3, pp. 345–382, 1991.

[97] H. Bostock, M. Baker, and G. Reid, "Changes in excitability of human motor axons underlying post-ischaemic fasciculations: evidence for two stable states." *The Journal of Physiology*, vol. 441, no. 1, pp. 537–557, 1991.

[98] F. Awiszus, "Effects of paranodal potassium permeability on repetitive activity of mammalian myelinated nerve fiber models," *Biological cybernetics*, vol. 64, no. 1, pp. 69–76, 1990.

[99] D. Stephanova and H. Bostock, "A distributed-parameter model of the myelinated human motor nerve fibre: temporal and spatial distributions of action potentials and ionic currents," *Biological cybernetics*, vol. 73, no. 3, pp. 275–280, 1995.

[100] B. Frankenhaeuser and A. Huxley, "The action potential in the myelinated nerve fibre of xenopus laevis as computed on the basis of voltage clamp data," *The Journal of Physiology*, vol. 171, no. 2, pp. 302–315, 1964.

[101] S. Chiu, J. Ritchie, R. Rogart, and D. Stagg, "A quantitative description of membrane currents in rabbit myelinated nerve." *The Journal of Physiology*, vol. 292, no. 1, pp. 149–166, 1979.

[102] T. Brismar, "Potential clamp analysis of membrane currents in rat myelinated nerve fibres." *The Journal of physiology*, vol. 298, no. 1, pp. 171–184, 1980.

[103] A. Scholz, G. Reid, W. Vogel, and H. Bostock, "Ion channels in human axons," *Journal of neurophysiology*, vol. 70, no. 3, pp. 1274–1279, 1993.

[104] J. R. Schwarz, G. Reid, and H. Bostock, "Action potentials and membrane currents in the human node of ranvier," *Pflügers Archiv*, vol. 430, no. 2, pp. 283–292, 1995.

[105] G. Reid, A. Scholz, H. Bostock, and W. Vogel, "Human axons contain at least five types of voltage-dependent potassium channel," *The Journal of Physiology*, vol. 518, no. 3, pp. 681–696, 1999.

[106] P. K. Stys and S. G. Waxman, "Activity-dependent modulation of excitability: Implications for axonal physiology and pathophysiology," *Muscle & nerve*, vol. 17, no. 9, pp. 969–974, 1994.

[107] A. Kuhn, T. Keller, M. Lawrence, and M. Morari, "A model for transcutaneous current stimulation: simulations and experiments," *Medical & biological engineering & computing*, vol. 47, no. 3, pp. 279–289, 2009.

[108] D. Bourbeau, J. Hokanson, J. Rubin, and D. Weber, "A computational model for estimating recruitment of primary afferent fibers by intraneural stimulation in the dorsal root ganglia," *Journal of neural engineering*, vol. 8, no. 5, p. 056009, 2011.

[109] J. Erlanger and E. A. Blair, "Comparative observations on motor and sensory fibers with special reference to repetitiousness," *American Journal of Physiology–Legacy Content*, vol. 121, no. 2, pp. 431–453, 1938.

[110] N. T. Carnevale and M. L. Hines, *The NEURON book*. Cambridge University Press, 2006.

[111] C. A. Bossetti, M. J. Birdno, and W. M. Grill, "Analysis of the quasi-static approximation for calculating potentials generated by neural stimulation," *Journal of neural engineering*, vol. 5, no. 1, p. 44, 2008.

[112] S. Gabriel, R. Lau, and C. Gabriel, "The dielectric properties of biological tissues: Iii. parametric models for the dielectric spectrum of tissues," *Physics in medicine and biology*, vol. 41, no. 11, p. 2271, 1996.

[113] R. Plonsey and R. C. Barr, *Bioelectricity: a quantitative approach*. Springer Science & Business Media, 2007.

[114] S. Joucla, A. Glière, and B. Yvert, "Current approaches to model extracellular electrical neural microstimulation," *Frontiers in computational neuroscience*, vol. 8, 2014.

[115] W. Rushton, "The effect upon the threshold for nervous excitation of the length of nerve exposed, and the angle between current and nerve," *The Journal of physiology*, vol. 63, no. 4, pp. 357–377, 1927.

[116] ——, "A physical analysis of the relation between threshold and interpolar length in the electric excitation of medullated nerve," *The Journal of physiology*, vol. 82, no. 3, pp. 332–352, 1934.

[117] ——, "Initiation of the propagated disturbance," *Proceedings of the Royal Society of London. Series B, Biological Sciences*, vol. 124, no. 835, pp. 210–243, 1937.

[118] F. Rattay, "Analysis of models for external stimulation of axons," *Biomedical Engineering, IEEE Transactions on*, no. 10, pp. 974–977, 1986.

[119] ——, "Modeling the excitation of fibers under surface electrodes," *Biomedical Engineering, IEEE Transactions on*, vol. 35, no. 3, pp. 199–202, 1988.

[120] ——, "Analysis of models for extracellular fiber stimulation," *Biomedical Engineering, IEEE Transactions on*, vol. 36, no. 7, pp. 676–682, 1989.

[121] C. R. Butson and C. C. McIntyre, "Role of electrode design on the volume of tissue activated during deep brain stimulation," *Journal of Neural Engineering*, vol. 3, no. 1, p. 1, 2006.

[122] C. M. Zierhofer, "Analysis of a linear model for electrical stimulation of axons-critical remarks on the" activating function concept"," *Biomedical Engineering, IEEE Transactions on*, vol. 48, no. 2, pp. 173–184, 2001.

[123] W. Wesselink, J. Holsheimer, and H. Boom, "A model of the electrical behaviour of myelinated sensory nerve fibres based on human data," *Medical & biological engineering & computing*, vol. 37, no. 2, pp. 228–235, 1999.

[124] C. C. McIntyre and W. M. Grill, "Extracellular stimulation of central neurons: influence of stimulus waveform and frequency on neuronal output," *Journal of Neurophysiology*, vol. 88, no. 4, pp. 1592–1604, 2002.

[125] C. C. McIntyre, W. M. Grill, D. L. Sherman, and N. V. Thakor, "Cellular effects of deep brain stimulation: model-based analysis of activation and inhibition," *Journal of neurophysiology*, vol. 91, no. 4, pp. 1457–1469, 2004.

[126] C. R. Butson and C. C. McIntyre, "Tissue and electrode capacitance reduce neural activation volumes during deep brain stimulation," *Clinical neurophysiology*, vol. 116, no. 10, pp. 2490–2500, 2005.

[127] M. Schiefer, R. J. Triolo, D. J. Tyler *et al.*, "A model of selective activation of the femoral nerve with a flat interface nerve electrode for a lower extremity neuroprosthesis," *Neural Systems and Rehabilitation Engineering, IEEE Transactions on*, vol. 16, no. 2, pp. 195–204, 2008.

[128] A. Kuhn, T. Keller, M. Lawrence, and M. Morari, "The influence of electrode size on selectivity and comfort in transcutaneous electrical stimulation of the forearm," *Neural Systems and Rehabilitation Engineering, IEEE Transactions on*, vol. 18, no. 3, pp. 255–262, 2010.

[129] J. Ladenbauer, K. Minassian, U. S. Hofstoetter, M. R. Dimitrijevic, and F. Rattay, "Stimulation of the human lumbar spinal cord with implanted and surface electrodes: a computer simulation study," *Neural Systems and Rehabilitation Engineering, IEEE Transactions on*, vol. 18, no. 6, pp. 637–645, 2010.

[130] S. M. Danner, U. S. Hofstoetter, J. Ladenbauer, F. Rattay, and K. Minassian, "Can the human lumbar posterior columns be stimulated by transcutaneous spinal cord stimulation? a modeling study," *Artificial organs*, vol. 35, no. 3, pp. 257–262, 2011.

[131] M. A. Schiefer, D. J. Tyler, and R. J. Triolo, "Probabilistic modeling of selective stimulation of the human sciatic nerve with a flat interface nerve electrode," *Journal of computational neuroscience*, vol. 33, no. 1, pp. 179–190, 2012.

[132] E. Peterson, O. Izad, and D. Tyler, "Predicting myelinated axon activation using spatial characteristics of the extracellular field," *Journal of neural engineering*, vol. 8, no. 4, p. 046030, 2011.

[133] M. Keane, S. Deyo, A. Abosch, J. A. Bajwa, and M. D. Johnson, "Improved spatial targeting with directionally segmented deep brain stimulation leads for treating essential tremor," *Journal of neural engineering*, vol. 9, no. 4, p. 046005, 2012.

[134] K. S. Frahm, C. D. Mørch, W. M. Grill, N. B. Lubock, K. Hennings, and O. K. Andersen, "Activation of peripheral nerve fibers by electrical stimulation in the sole of the foot," *BMC neuroscience*, vol. 14, no. 1, p. 116, 2013.

[135] B. A. Teplitzky, A. T. Connolly, J. A. Bajwa, and M. D. Johnson, "Computational modeling of an endovascular approach to deep brain stimulation," *Journal of neural engineering*, vol. 11, no. 2, p. 026011, 2014.

[136] Q. Huang, H. Oya, O. E. Flouty, C. G. Reddy, M. A. Howard III, G. T. Gillies, and M. Utz, "Comparison of spinal cord stimulation profiles from intra-and extradural electrode arrangements by finite element modelling," *Medical & biological engineering & computing*, vol. 52, no. 6, pp. 531–538, 2014.

[137] P. Marianelli, M. Capogrosso, L. Bassi Luciani, A. Panarese, and S. Micera, "A computational framework for electrical stimulation of vestibular nerve," 2015.

[138] C. Gabriel, S. Gabriel, and E. Corthout, "The dielectric properties of biological tissues: I. literature survey," *Physics in medicine and biology*, vol. 41, no. 11, p. 2231, 1996.

[139] S. Gabriel, R. Lau, and C. Gabriel, "The dielectric properties of biological tissues: Ii. measurements in the frequency range 10 hz to 20 ghz," *Physics in medicine and biology*, vol. 41, no. 11, p. 2251, 1996.

[140] P. Šuhel, P. Vrtačnik, and M. Trlep, "Bioimpedance measurement in the lower urinary tract: numerical calculation of the potential and current distribution," in *Engineering in Medicine and Biology Society, 1995., IEEE 17th Annual Conference*, vol. 2. IEEE, 1995, pp. 1523–1524.

[141] C. M. Davies, C. M. Ferguson, C. Kaucner, M. Krogh, N. Altavilla, D. A. Deere, and N. J. Ashbolt, "Dispersion and transport of cryptosporidium oocysts from fecal pats under simulated rainfall events," *Applied and environmental microbiology*, vol. 70, no. 2, pp. 1151–1159, 2004.

[142] G. Schalow, G. Zäch, and R. Warzok, "Classification of human peripheral nerve fibre groups by conduction velocity and nerve fibre diameter is preserved following spinal cord lesion," *Journal of the autonomic nervous system*, vol. 52, no. 2, pp. 125–150, 1995.

[143] M. L. Hines and N. T. Carnevale, "The neuron simulation environment," *Neural computation*, vol. 9, no. 6, pp. 1179–1209, 1997.

[144] M. L. Hines, T. Morse, M. Migliore, N. T. Carnevale, and G. M. Shepherd, "Modeldb: a database to support computational neuroscience," *Journal of computational neuroscience*, vol. 17, no. 1, pp. 7–11, 2004.

[145] A. N. Shiraz, B. Leaker, and A. Demosthenous, "Optimization of a wearable pudendal nerve stimulator using computational models," in *Engineering in Medicine and Biology Society (EMBC), 2015 37th Annual International Conference of the IEEE*. IEEE, 2015, pp. 3395–3398.

[146] D. B. McCreery, W. F. Agnew, T. G. Yuen, and L. Bullara, "Charge density and charge per phase as cofactors in neural injury induced by electrical stimulation," *Biomedical Engineering, IEEE Transactions on*, vol. 37, no. 10, pp. 996–1001, 1990.

[147] D. R. Merrill, M. Bikson, and J. G. Jefferys, "Electrical stimulation of excitable tissue: design of efficacious and safe protocols," *Journal of neuroscience methods*, vol. 141, no. 2, pp. 171–198, 2005.

[148] J. E. Arle and J. L. Shils, *Essential neuromodulation*. Academic Press, 2011.

[149] S. F. Cogan, "Neural stimulation and recording electrodes," *Annu. Rev. Biomed. Eng.*, vol. 10, pp. 275–309, 2008.

[150] J. V. Basmajian and C. De Luca, "Muscles alive," *Proceedings of The Royal Society of Medicine*, vol. 278, p. 126, 1985.

[151] R. Merletti and P. A. Parker, *Electromyography: physiology, engineering, and non-invasive applications*. John Wiley & Sons, 2004, vol. 11.

[152] A. Guillot, F. Lebon, D. Rouffet, S. Champely, J. Doyon, and C. Collet, "Muscular responses during motor imagery as a function of muscle contraction types," *International Journal of Psychophysiology*, vol. 66, no. 1, pp. 18–27, 2007.

[153] A. Holobar, P. Enck, H. Hinninghofer, and R. Merletti, "Decomposition of surface emg from external anal sphincter," in *XVII Congress of the International Society of Electrophysiology and Kinesiology, Niagara Falls, Ontario*, 2008.

[154] C. Cescon, E. E. Raimondi, V. Začesta, K. Drusany-Starič, K. Martsidis, and R. Merletti, "Characterization of the motor units of the external anal sphincter in pregnant women with multichannel surface emg," *International urogynecology journal*, vol. 25, no. 8, pp. 1097–1103, 2014.

[155] C. J. De Luca, "Physiology and mathematics of myoelectric signals," *Biomedical Engineering, IEEE Transactions on*, no. 6, pp. 313–325, 1979.

[156] G. C. Agarwal and G. L. Gottlieb, "An analysis of the electromyogram by fourier, simulation and experimental techniques," *Biomedical Engineering, IEEE Transactions on*, no. 3, pp. 225–229, 1975.

[157] J. Duchêne and J.-Y. Hogrel, "A model of emg generation," *Biomedical Engineering, IEEE Transactions on*, vol. 47, no. 2, pp. 192–201, 2000.

[158] D. Farina and R. Merletti, "Comparison of algorithms for estimation of emg variables during voluntary isometric contractions," *Journal of Electromyography and Kinesiology*, vol. 10, no. 5, pp. 337–349, 2000.

[159] D. Farina, R. Merletti, and R. M. Enoka, "The extraction of neural strategies from the surface emg," *Journal of Applied Physiology*, vol. 96, no. 4, pp. 1486–1495, 2004.

[160] D. Farina, E. Fortunato, and R. Merletti, "Noninvasive estimation of motor unit conduction velocity distribution using linear electrode arrays," *Biomedical Engineering, IEEE Transactions on*, vol. 47, no. 3, pp. 380–388, 2000.

[161] D. Farina and R. Merletti, "A novel approach for precise simulation of the emg signal detected by surface electrodes," *Biomedical Engineering, IEEE Transactions on*, vol. 48, no. 6, pp. 637–646, 2001.

[162] D. Farina, W. Muhammad, E. Fortunato, O. Meste, R. Merletti, and H. Rix, "Estimation of single motor unit conduction velocity from surface electromyogram signals detected with linear electrode arrays," *Medical and Biological Engineering and Computing*, vol. 39, no. 2, pp. 225–236, 2001.

[163] D. Farina, A. Crosetti, and R. Merletti, "A model for the generation of synthetic intramuscular emg signals to test decomposition algorithms," *Biomedical Engineering, IEEE Transactions on*, vol. 48, no. 1, pp. 66–77, 2001.

[164] D. Farina, C. Cescon, and R. Merletti, "Influence of anatomical, physical, and detection-system parameters on surface emg," *Biological cybernetics*, vol. 86, no. 6, pp. 445–456, 2002.

[165] D. Farina, L. Mesin, S. Martina, and R. Merletti, "A surface emg generation model with multilayer cylindrical description of the volume conductor," *Biomedical Engineering, IEEE Transactions on*, vol. 51, no. 3, pp. 415–426, 2004.

[166] D. Farina and A. Rainoldi, "Compensation of the effect of sub-cutaneous tissue layers on surface emg: a simulation study," *Medical engineering & physics*, vol. 21, no. 6, pp. 487–497, 1999.

[167] A. J. Fuglevand, D. A. Winter, A. E. Patla, and D. Stashuk, "Detection of motor unit action potentials with surface electrodes: influence of electrode size and spacing," *Biological cybernetics*, vol. 67, no. 2, pp. 143–153, 1992.

[168] T. Kiryu, Y. Saitoh, and K. Ishioka, "Investigation on parametric analysis of dynamic emg signals by a muscle-structured simulation model," *Biomedical Engineering, IEEE Transactions on*, vol. 39, no. 3, pp. 280–288, 1992.

[169] P. Lago and N. Jones, "Effect of motor-unit firing time statistics on emg spectra," *Medical and Biological Engineering and computing*, vol. 15, no. 6, pp. 648–655, 1977.

[170] M. M. Lowery, N. S. Stoykov, A. Taflove, T. Kuiken *et al.*, "A multiple-layer finite-element model of the surface emg signal," *Biomedical Engineering, IEEE Transactions on*, vol. 49, no. 5, pp. 446–454, 2002.

[171] M. M. Lowery, N. S. Stoykov, and T. A. Kuiken, "A simulation study to examine the use of cross-correlation as an estimate of surface emg cross talk," *Journal of Applied Physiology*, vol. 94, no. 4, pp. 1324–1334, 2003.

[172] M. M. Lowery and M. J. O'Malley, "Analysis and simulation of changes in emg amplitude during high-level fatiguing contractions," *Biomedical Engineering, IEEE Transactions on*, vol. 50, no. 9, pp. 1052–1062, 2003.

[173] R. Merletti and L. R. L. Conte, "Surface emg signal processing during isometric contractions," *Journal of Electromyography and Kinesiology*, vol. 7, no. 4, pp. 241–250, 1997.

[174] R. Merletti, S. H. Roy, E. Kupa, S. Roatta, and A. Granata, "Modeling of surface myoelectric signals. ii. model-based signal interpretation," *Biomedical Engineering, IEEE Transactions on*, vol. 46, no. 7, pp. 821–829, 1999.

[175] L. Mesin and D. Farina, "Simulation of surface emg signals generated by muscle tissues with inhomogeneity due to fiber pinnation," *Biomedical Engineering, IEEE Transactions on*, vol. 51, no. 9, pp. 1521–1529, 2004.

[176] L. Mesin, M. Joubert, T. Hanekom, R. Merletti, and D. Farina, "A finite element model for describing the effect of muscle shortening on surface emg," *Biomedical Engineering, IEEE Transactions on*, vol. 53, no. 4, pp. 593–600, 2006.

[177] L. Mesin, R. Merletti, and A. Rainoldi, "Surface emg: the issue of electrode location," *Journal of Electromyography and Kinesiology*, vol. 19, no. 5, pp. 719–726, 2009.

[178] S. Nandedkar and E. Stålberg, "Simulation of macro emg motor unit potentials," *Electroencephalography and clinical neurophysiology*, vol. 56, no. 1, pp. 52–62, 1983.

[179] S. Nandedkar *et al.*, "Simulation of single muscle fibre action potentials," *Medical and Biological Engineering and Computing*, vol. 21, no. 2, pp. 158–165, 1983.

[180] D. F. Stegeman and W. H. Linssen, "Muscle fiber action potential changes and surface emg: a simulation study," *Journal of Electromyography and Kinesiology*, vol. 2, no. 3, pp. 130–140, 1992.

[181] A. Hamilton-Wright and D. W. Stashuk, "Physiologically based simulation of clinical emg signals," *Biomedical Engineering, IEEE Transactions on*, vol. 52, no. 2, pp. 171–183, 2005.

[182] D. F. Stegeman, J. H. Blok, H. J. Hermens, and K. Roeleveld, "Surface emg models: properties and applications," *Journal of Electromyography and Kinesiology*, vol. 10, no. 5, pp. 313–326, 2000.

[183] P. Rosenfalck, "Intra-and extracellular potential fields of active nerve and muscle fibres. a physico-mathematical analysis of different models." *Thrombosis et diathesis haemorrhagica. Supplementum*, vol. 321, p. 1, 1969.

[184] M. S. Spach, R. C. Barr, G. A. Serwer, J. M. Kootsey, and E. A. JOHNSON, "Extracellular potentials related to intracellular action potentials in the dog purkinje system," *Circulation research*, vol. 30, no. 5, pp. 505–519, 1972.

[185] K. McGill, "Surface electromyogram signal modelling," *Medical and Biological Engineering and Computing*, vol. 42, no. 4, pp. 446–454, 2004.

[186] A. Gydikov, D. Kosarov, and N. Tankov, "Studying the alpha motoneurone activity by investigating motor units of various sizes." *Electromyography and clinical neurophysiology*, vol. 12, no. 2, pp. 99–117, 1971.

[187] D. Staudenmann, K. Roeleveld, D. F. Stegeman, and J. H. Van Dieën, "Methodological aspects of semg recordings for force estimation–a tutorial and review," *Journal of Electromyography and Kinesiology*, vol. 20, no. 3, pp. 375–387, 2010.

[188] D. Farina, P. Madeleine, T. Graven-Nielsen, R. Merletti, and L. Arendt-Nielsen, "Standardising surface electromyogram recordings for assessment of activity and fatigue in the human upper trapezius muscle," *European journal of applied physiology*, vol. 86, no. 6, pp. 469–478, 2002.

[189] R. Merletti, D. Farina, M. Gazzoni, and M. P. Schieroni, "Effect of age on muscle functions investigated with surface electromyography," *Muscle & nerve*, vol. 25, no. 1, pp. 65–76, 2002.

[190] H. Hermens, B. Freriks, R. Merletti, D. Stegerman, J. Block, and A. Gre, "Seniam: European recommendations for surface electromyography roessingh research and development, enschede," 2013.

[191] C. J. De Luca, "Surface electromyography: Detection and recording," *DelSys Incorporated*, vol. 10, p. 2011, 2002.

[192] V. T. Inman, H. Ralston, J. d. C. Saunders, M. B. Feinstein, and E. W. Wright, "Relation of human electromyogram to muscular tension," *Electroencephalography and clinical neurophysiology*, vol. 4, no. 2, pp. 187–194, 1952.

[193] E. Shwedyk, R. Balasubramanian, and R. Scott, "A nonstationary model for the electromyogram," *Biomedical Engineering, IEEE Transactions on*, no. 5, pp. 417–424, 1977.

[194] N. Hogan and R. W. Mann, "Myoelectric signal processing: Optimal estimation applied to electromyography-part i: Derivation of the optimal myoprocessor," *Biomedical Engineering, IEEE Transactions on*, no. 7, pp. 382–395, 1980.

[195] E. Clancy, N. Hogan *et al.*, "Single site electromyograph amplitude estimation," *Biomedical Engineering, IEEE Transactions on*, vol. 41, no. 2, pp. 159–167, 1994.

[196] D. Godin, P. Parker, and R. Scott, "Noise characteristics of stainless-steel surface electrodes," *Medical and Biological Engineering and Computing*, vol. 29, no. 6, pp. 585–590, 1991.

[197] E. Clancy, E. L. Morin, and R. Merletti, "Sampling, noise-reduction and amplitude estimation issues in surface electromyography," *Journal of Electromyography and Kinesiology*, vol. 12, no. 1, pp. 1–16, 2002.

[198] S. Conforto, T. D'Alessio, and S. Pignatelli, "Optimal rejection of movement artefacts from myoelectric signals by means of a wavelet filtering procedure," *Journal of Electromyography and Kinesiology*, vol. 9, no. 1, pp. 47–57, 1999.

[199] K. T. Sweeney, T. E. Ward, and S. F. McLoone, "Artifact removal in physiological signalspractices and possibilities," *Information Technology in Biomedicine, IEEE Transactions on*, vol. 16, no. 3, pp. 488–500, 2012.

[200] P. S. Hamilton and M. G. Curley, "Adaptive removal of motion artifact," in *Engineering in Medicine and Biology Society, 1997. Proceedings of the 19th Annual International Conference of the IEEE*, vol. 1. IEEE, 1997, pp. 297–299.

[201] C. J. De Luca, L. D. Gilmore, M. Kuznetsov, and S. H. Roy, "Filtering the surface emg signal: Movement artifact and baseline noise contamination," *Journal of biomechanics*, vol. 43, no. 8, pp. 1573–1579, 2010.

[202] J. Klijn and M. Kloprogge, "Cable artefact suppressor for electrophysiological recording." *Electromyography and clinical neurophysiology*, vol. 13, no. 1, p. 87, 1973.

[203] J. G. Webster, "Reducing motion artifacts and interference in biopotential recording," *Biomedical Engineering, IEEE Transactions on*, no. 12, pp. 823–826, 1984.

[204] S. Nishimura, Y. Tomita, and T. Horiuchi, "Clinical application of an active electrode using an operational amplifier," *Biomedical Engineering, IEEE Transactions on*, vol. 39, no. 10, pp. 1096–1099, 1992.

[205] Y. Zhang, P. Parker, and R. Scott, "Study of the effects of motor unit recruitment and firing statistics on the signal-to-noise ratio of a myoelectric control channel," *Medical and Biological Engineering and Computing*, vol. 28, no. 3, pp. 225–231, 1990.

[206] R. B. Blackman and J. W. Tukey, "The measurement of power spectra," 1958.

[207] L. Cohen, "Generalization of the wiener-khinchin theorem," *Signal Processing Letters, IEEE*, vol. 5, no. 11, pp. 292–294, 1998.

[208] T. DAlessio, N. Accornero, and A. Berardelli, "Toward a real time adaptive processor for surface emg signals," in *Ann. Int. Conf. IEEE Eng. Med. Biol. Soc*, vol. 9, 1987, pp. 323–324.

[209] E. Kaiser and I. Petersen, "Adaptive filter for emg control signals," *The Control of Upper-Extremity Prostheses and Orthoses*, pp. 54–57, 1974.

[210] E. Clancy, K. Farry *et al.*, "Adaptive whitening of the electromyogram to improve amplitude estimation," *Biomedical Engineering, IEEE Transactions on*, vol. 47, no. 6, pp. 709–719, 2000.

[211] P. Prakash, C. A. Salini, J. A. Tranquilli, D. R. Brown, E. A. Clancy *et al.*, "Adaptive whitening in electromyogram amplitude estimation for epoch-based applications," *IEEE transactions on biomedical engineering*, vol. 52, no. 2, pp. 331–334, 2005.

[212] E. A. Clancy, O. Bida, and D. Rancourt, "Influence of advanced electromyogram (emg) amplitude processors on emg-to-torque estimation during constant-posture, force-varying contractions," *Journal of biomechanics*, vol. 39, no. 14, pp. 2690–2698, 2006.

[213] N. Hogan and R. W. Mann, "Myoelectric signal processing: Optimal estimation applied to electromyography-part ii: experimental demonstration of optimal myoprocessor performance," *Biomedical Engineering, IEEE Transactions on*, no. 7, pp. 396–410, 1980.

[214] M. Hakonen, H. Piitulainen, and A. Visala, "Current state of digital signal processing in myoelectric interfaces and related applications," *Biomedical Signal Processing and Control*, vol. 18, pp. 334–359, 2015.

[215] E. Clancy, N. Hogan *et al.*, "Multiple site electromyograph amplitude estimation," *Biomedical Engineering, IEEE Transactions on*, vol. 42, no. 2, pp. 203–211, 1995.

[216] D. Staudenmann, I. Kingma, A. Daffertshofer, D. Stegeman, and J. Van Dieën, "Heterogeneity of muscle activation in relation to force direction: A multi-channel surface electromyography study on the triceps surae muscle," *Journal of Electromyography and Kinesiology*, vol. 19, no. 5, pp. 882–895, 2009.

[217] H. Roesler, "Statistical analysis and evaluation of myoelectric signals for proportional control," *The Control of upper-extremity prostheses and orthoses*, pp. 44–53, 1974.

[218] P. Parker, J. Stuller, R. Scott *et al.*, "Signal processing for the multistate myoelectric channel," *Proceedings of the IEEE*, vol. 65, no. 5, pp. 662–674, 1977.

[219] E. Clancy, N. Hogan *et al.*, "Probability density of the surface electromyogram and its relation to amplitude detectors," *Biomedical Engineering, IEEE Transactions on*, vol. 46, no. 6, pp. 730–739, 1999.

[220] Y. St-Amant, D. Rancourt, E. Clancy *et al.*, "Influence of smoothing window length on electromyogram amplitude estimates," *Biomedical Engineering, IEEE Transactions on*, vol. 45, no. 6, pp. 795–799, 1998.

[221] E. Clancy *et al.*, "Electromyogram amplitude estimation with adaptive smoothing window length," *Biomedical Engineering, IEEE Transactions on*, vol. 46, no. 6, pp. 717–729, 1999.

[222] R. Merletti, A. Bottin, C. Cescon, D. Farina, M. Gazzoni, S. Martina, L. Mesin, M. Pozzo, A. Rainoldi, and P. Enck, "Multichannel surface emg for the non-invasive assessment of the anal sphincter muscle," *Digestion*, vol. 69, no. 2, pp. 112–122, 2004.

[223] N. Binnie, B. Kawimbe, M. Papachrysostomou, N. Clare, and A. Smith, "The importance of the orientation of the electrode plates in recording the external anal sphincter emg by non-invasive anal plug electrodes," *International journal of colorectal disease*, vol. 6, no. 1, pp. 5–8, 1991.

[224] P. O'Donnell, C. Beck, R. Doyle, and C. Eubanks, "Surface electrodes in perineal electromyography," *Urology*, vol. 32, no. 4, pp. 375–379, 1988.

[225] P. Enck, H. Franz, F. Azpiroz, X. Fernandez-Fraga, H. Hinninghofen, K. Kaske-Bretag, A. Bottin, S. Martina, and R. Merletti, "Innervation zones of the external anal sphincter in healthy male and female subjects," *Digestion*, vol. 69, no. 2, pp. 123–130, 2004.

[226] P. Enck, H. Hinninghofen, R. Merletti, and F. Azpiroz, "The external anal sphincter and the role of surface electromyography," *Neurogastroenterology & Motility*, vol. 17, no. s1, pp. 60–67, 2005.

[227] P. Enck and D. B. Vodušek, "Electromyography of pelvic floor muscles," *Journal of Electromyography and Kinesiology*, vol. 16, no. 6, pp. 568–577, 2006.

[228] R. Merletti, A. Holobar, and D. Farina, "Analysis of motor units with high-density surface electromyography," *Journal of electromyography and kinesiology*, vol. 18, no. 6, pp. 879–890, 2008.

[229] L. Mesin, "Estimation of monopolar signals from sphincter muscles and removal of common mode interference," *Biomedical Signal Processing and Control*, vol. 4, no. 1, pp. 37–48, 2009.

[230] C. Cescon, L. Mesin, M. Nowakowski, and R. Merletti, "Geometry assessment of anal sphincter muscle based on monopolar multichannel surface emg signals," *Journal of Electromyography and Kinesiology*, vol. 21, no. 2, pp. 394–401, 2011.

[231] K. Ullah, C. Cescon, B. Afsharipour, and R. Merletti, "Automatic detection of motor unit innervation zones of the external anal sphincter by multichannel surface emg," *Journal of Electromyography and Kinesiology*, vol. 24, no. 6, pp. 860–867, 2014.

[232] J. R. Macdonald and E. Barsoukov, "Impedance spectroscopy: theory, experiment, and applications," *History*, vol. 1, p. 8, 2005.

[233] E. McAdams, A. Lackermeier, J. McLaughlin, D. Macken, and J. Jossinet, "The linear and non-linear electrical properties of the electrode-electrolyte interface," *Biosensors and Bioelectronics*, vol. 10, no. 1, pp. 67–74, 1995.

[234] S. Mayer, L. Geddes, J. Bourland, and L. Ogborn, "Faradic resistance of the electrode/electrolyte interface," *Medical and Biological Engineering and Computing*, vol. 30, no. 5, pp. 538–542, 1992.

[235] W. Franks, I. Schenker, P. Schmutz, and A. Hierlemann, "Impedance characterization and modeling of electrodes for biomedical applications," *Biomedical Engineering, IEEE Transactions on*, vol. 52, no. 7, pp. 1295–1302, 2005.

[236] P. Zoltowski, "On the electrical capacitance of interfaces exhibiting constant phase element behaviour," *Journal of Electroanalytical Chemistry*, vol. 443, no. 1, pp. 149–154, 1998.

[237] A. N. Shiraz, A. Demosthenous, and A. Vanhoestenberghe, "Towards an optimized wearable neuromodulation device for urinary incontinence," in *Electronics, Circuits and Systems (ICECS), 2012 19th IEEE International Conference on*. IEEE, 2012, pp. 25–28.

[238] T. Pajkossy, "Impedance of rough capacitive electrodes," *Journal of Electroanalytical Chemistry*, vol. 364, no. 1, pp. 111–125, 1994.

[239] R. De Levie, "The influence of surface roughness of solid electrodes on electrochemical measurements," *Electrochimica Acta*, vol. 10, no. 2, pp. 113–130, 1965.

[240] L. Nyikos and T. Pajkossy, "Fractal dimension and fractional power frequency-dependent impedance of blocking electrodes," *Electrochimica Acta*, vol. 30, no. 11, pp. 1533–1540, 1985.

[241] S. D. Roy, "On the realization of a constant-argument immittance or fractional operator," *Circuit Theory, IEEE Transactions on*, vol. 14, no. 3, pp. 264–274, 1967.

[242] E. M. Spinelli, R. Pallàs-Areny, and M. A. Mayosky, "Ac-coupled front-end for biopotential measurements," *Biomedical Engineering, IEEE Transactions on*, vol. 50, no. 3, pp. 391–395, 2003.

[243] G. E. Box, G. M. Jenkins, and G. C. Reinsel, *Time series analysis: forecasting and control*. John Wiley & Sons, 2011, vol. 734.

[244] T. F. Coleman and Y. Li, "An interior trust region approach for nonlinear minimization subject to bounds," *SIAM Journal on optimization*, vol. 6, no. 2, pp. 418–445, 1996.

[245] E. S. Glen, "Effective and safe control of incontinence by the intra-anal plug electrode," *British Journal of Surgery*, vol. 58, no. 4, pp. 249–252, 1971.

[246] S. Nivatvongs, H. S. Stern, and D. S. Fryd, "The length of the anal canal," *Diseases of the Colon & Rectum*, vol. 24, no. 8, pp. 600–601, 1981.

[247] J. Melgaard, N. J. Rijkhoff *et al.*, "Detecting urinary bladder contractions: methods and devices," *Journal of Sensor Technology*, vol. 4, no. 04, p. 165, 2014.

[248] O. C. Zienkiewicz, R. L. Taylor, O. C. Zienkiewicz, and R. L. Taylor, *The finite element method*. McGraw-hill London, 1977, vol. 3.

Appendix A

Finite Element method [248]

This numerical method is based on dividing a domain into what is called elements. These elements should cover all the domain without overlapping. An approximation of the weak formulation of the relevant partial differential equations is found using different methods in each single element. As the elements are ideally sufficiently small, when basis functions are defined locally, they yield a good approximation of the actual solution to the partial differential equations. The overall function in the domain is then simply approximated as the summation of all the local basis functions.

The defining feature of FEM is that it is *exact-in-the-limit*, meaning that the degree of approximation can only improve if the number of elements are increased. As the number of elements increases, the solution gradually converges to the exact solution to the partial differential equations. Thus, depending on the need for a certain level of accuracy, it is possible to increase the number of elements, which are also referred to as the mesh. As the number of elements increases, however, the required time and computational power increase.

Depending on the shape of the volume in which the equations are solved, different mesh shapes may be used.

Appendix B

HH-type channel parameters [17]

Current	Equations
Fast sodium	$I_{Naf} = g_{Naf} m^3 h (V_m - E_{Na})$
	$\alpha_m = \frac{6.57(V_m+20.4)}{1-e^{\frac{-V_m-20.4)}{10.3}}}$
	$\alpha_h = \frac{0.34(-V_m-114)}{1-e^{\frac{V_m+114}{11}}}$
	$\beta_m = \frac{0.304(-V_m-25.7)}{1-e^{\frac{V_m+25.7}{9.16}}}$
	$\beta_h = \frac{12.6}{1+e^{\frac{-V_m-31.8}{13.4}}}$
Persistent sodium	$I_{Nap} = g_{Nap} p^3 (V_m - E_{Na})$
	$\alpha_p = \frac{0.0353(V_m+27)}{1-e^{\frac{-V_m-27)}{10.2}}}$
	$\beta_p = \frac{0.000883(-V_m-34)}{1-e^{\frac{V_m+34}{10}}}$
Slow potassium	$I_{Ks} = g_{Ks} s (V_m - E_K)$
	$\alpha_s = \frac{0.3}{1+e^{\frac{V_m+53)}{-5}}}$
	$\beta_p = \frac{0.03}{1+e^{\frac{V_m+90}{-1}}}$